Università degli Studi Di Genova
Facoltà di Scienze Matematiche Fisiche e Naturali

Tesi di Dottorato di Ricerca in Fisica

Osservazione di radiazione cosmica di altissima energia dallo spazio

Candidato:
A. Thea

Relatore:
Prof. A. Petrolini

Relatore Esterno:
Dott. S. Bottai

XVIII Ciclo di Dottorato

Contents

Introduction

The cosmic radiation, discovered by Hess and Kohlhörster in 1912, has been since the very beginning a very active field of research, both because of its intrinsic scientific interest, and because it has been for long time a unique tool for elementary particle physics.

The nature of the cosmic radiation was a mistery for a long time, and many fundamental questions are still unanswered nowadays.

In 1925 Millikan named the cosmic radiation "Cosmic Rays", believing it was composed of electromagnetic radiation only. In fact, the Cosmic Rays (CR) are mainly constituted of protons, anti-protons, and standard nuclei, from light elements up to iron. At the highest energies the composition is still uncertain, and a significant neutrino component cannot be ruled out.

The known energy spectrum of CR is extremely regular, although its intensity spans more than thirty orders of magnitude over more than ten energy decades, from a few hundreds MeV up to almost a ZeV (10^{21} eV). Nowadays the upper limit of the CR energy spectrum is still unknown. In the past 40 years twenty events with energy $E \gtrsim 10^{20}$ eV have been detected by 5 different experiments: Volcano Ranch [1], Haverah Park [2], Yakutsk [3] and more recently Fly's Eye [4, 5] and Agasa [6, 7, 8]. Although the existence of the so called UHECRs is well established, their origin, the maximum energy and their nature still remain a mystery.

The origin of particles of such enormous energies is unknown. Two classes of possible explanations have been developed in the recent years. The first class ("bottom-up approach"), assumes that some astrophysical object is capable of accelerating charged particles to such energies; the second class ("top-down" approach) assumes that the highest energy cosmic rays are decay product of super-heavy particles that are slowly decaying since the big-bang. None of the two approaches has produced a convincing model so far.

According to our present knowledge, no astrophysical accelerator has the power to accelerate a particle to such energies. Even worse, for the best hypothetical candidate accelerator, the highest energies would be likely

obtained in its central region, where the density of matter and energy are very high. It is then very difficult to extract a particle out of the core of the accelerator without losing a lot of energy. On the other hand, even if some classes of object would be able to boost the particles to the highest energies, the interaction with the Cosmic Microwave Background Radiation (CMB) during the propagation toward the Earth would rapidly degrade the initial energy strongly suppressing the flux above $\approx 5 \cdot 10^{19}$ eV. This effect, known as Greisen-Zatsepin-Kuzmin (GZK) effect, is of the utmost importance for the study of the extreme energy cosmic rays. Particularly, the GZK suppression limits the maximum distance of possible source candidates to a few tens of Mpc.

The cosmic rays arrival direction is isotropic, unless possibly the very high energy ones. This is not surprising, because according to the present knowledge of the galactic and intergalactic magnetic fields, all charged particles are strongly deflected. Only the UHECR are not significantly deflected and could point to their source.

According to the results obtained by all the experiments the UHECR incoming directions are distributed isotropically, within the limits of the collected statistics. This result is in conflict with the anisotropy of the distribution of luminous matter in the range of 100 Mpc from the Earth, but the currently available statistics is very limited and the issue is still open. The AGASA experiment has actually seen some "doublets" and two "triplets" that could suggest the existence of point like sources.

The greatest difficulty in the detection of UHECRs comes from the limited statistics: as a matter of fact, the flux at the highest energy is extremely low. According to the collected data, the estimated flux above 10^{20} eV is ≈ 1 event$\cdot$km$^{-2}\cdot$sr$^{-1}\cdot$century^{-1} which impose the construction of detectors with a sensitive area of the order of hundreds of km^2 or more.

The UHECR cannot be observed directly because of the shielding effect of the atmosphere. The detection techniques are based on the observation of the Extensive Air Shower (EAS) generated by the impact of the CR with the atmosphere.

The most effective techniques for the observation of UHECRs are the direct observation of the secondary particles with a giant array of detectors when they reach the ground and the measurement of the fluorescence light produced by the secondaries traveling through the air.

In the first case the energy and the incoming direction are reconstructed measuring the footprint of the EAS. The direction is reconstructed with an average error of a couple of degrees measuring the time structure of the shower, while the energy is inferred by the density of particles as a function of the distance from the shower axis.

Alternately in clear moonless nights the air fluorescence light emitted by the nitrogen molecules can be detected. Every element of the photodetector watches a region of the sky. The development of an EAS appears on the focal surface as set of bright points aligned on a track, whose intensity is proportional to the number of charged particles.

In both cases the ground detectors can monitor only a limited portion of atmosphere due to the practical constraints of the monitored area or to the limited Field Of View (FOV). Furthermore the coverage provided by ground based fluorescence detector is reduced by the fact that EASs mainly develop at low altitude. The alternatives are to extend enormously the area of the detector or to approach the problem from a different perspective.

John Linsley [9], in 1982 first suggested that the Earth's atmosphere at night, viewed from Space, constitutes a huge calorimeter for remotely observing UHECR (SOCRAS [10]) . The observation of fluorescence light from space, exploiting the atmosphere huge calorimeter, is a proper solution for the extremely low fluxes. An orbiting detector at few hundreds km can monitor an area of the order of hundreds thousands km^2.

Since 1982 a number of proposals and studies were carried on, including the *Orbiting Wide-angle Light-collectors Experiment* (OWL) [11] project, the TUS/KLYPVE [12] project and the *Extreme Universe Space Observatory* (*EUSO*) experiment [13], a pathfinder mission of the European Space Agency.

The basic concept of the space approach is to observe the fluorescence light with a large aperture and a large FOV optics. The image of the EAS is recorded on the focal surface with a granularity and a sampling rate high enough to reconstruct the EAS direction and energy with a precision of the order of currently running experiments. The complexity of the detector is increased by the constraints which any space instrument must fulfill.

The design and optimization of the mission is a difficult task. A space mission must fulfill an additional number of requirements which are unknown to ground detectors. The resources available for the instrument are limited: power, mass, volume and telemetry. The instrument must be qualified for the launch and to operate in space which entails a limited choice of technologies and materials. Eventually the instrument must operate unmanned for several years in the hostile space environment. On the contrary, the observation of the faint EAS signal from space requires a large optics to collect as many photons as possible as well as an efficient and reliable photosensor, a number of channels of the order of few hundred thousands which have to be efficiently digitizes with a sampling rate of the order of few hundreds *kHz* . The design of the mission must be tuned

to optimize the delicate balance between space constraints and observational requirements. The mission's parameters must also be optimized according the physics objective: the observation of 10^{19} eV "low" energy showers would prefer a low orbit to increase the photon's statistics while the observation of the high energy tail of the spectrum would prefer high altitude orbit to maximise the monitored atmosphere volume.

The work of this PhD thesis has been carried out in this framework. In the first part I have contributed to the *EUSO* mission. *EUSO*, the European Space Agency (ESA) path-finder for the observation of UHECR from space, has been designed to be installed on the International Space Station (ISS). After a successful ESA Phase A study, from both technical and scientific point of view, *EUSO* has been put oh hold because of financial and programmatic issues related to the Columbia Space Shuttle accident in 2003.

The second part of the research has been focused on the planning of a new mission in the framework of the ESA Cosmic Vision program 2015-2025 [14].

The research activity has comprised three main topics:

- A preliminaty study on the relation between the scientific requirements and the mission requirements with an analytical and semi-analytical approach. This investigation is the base for the mission planning and provides an useful overview on the the delicate balance between constraints and requirements foe a space-based UHECR observatory.

- The development of the Monte-Carlo simulation and reconstruction software for *EUSO*. The complexity of both the instrument and the physics of signal production and transport in the Earth's atmosphere require a detailed Monte-Carlo simulation to reach a good understanding of the performances and the systematics of the technique and the detector. In particlular we have studied and implemented in the software framewor a possible trigger scheme for *EUSO*. We have also used the *EUSO* design as a model to simulate a larger detector in realistic conditions. In the view of the planning of Cosmic Vision mission we have also used the *EUSO* design as a model to simulate a larger detector in realistic conditions. Applying the trigger scheme we developed to the extended detectors we studied the relation between the trigger threshold and the instrument's effective collection area.

- The investigation of the characteristic of a new promising type of single-photon solid-state detector, the Silicon Photomultiplier, as a possible candidate photonsensor for *EUSO* or a future space mission. The Silicon Photomultiplier (SiPM) aims to combine the intrinsic high quantum efficiency with the multiplication factor of a geiger avalanche in a single silicon device. The successful development of this concept would provide the scientific community with an high QE, high gain, low consumption and compact detector for single photon counting. In a photon hungry UHECR space experiment where the photodetector is one of the main entries in the mass and power budgets. An high QE photodetector can increase the sensitivity significantly, an improvement that otherwise could could be achieved only with a larger instrument. Even if the SiPM technology has not reached the maturity yet, the chances that in the next year prototypes with competitives characteristics are good in the prospect of a future Cosmic Vision mission. This activity has been carried out at the Max-Plank Institute für Physik of Munich

The present work is organized in the following way. The first part is a brief overview to the origin, propagation and observation of UHECR. The second part illustrates the three aspects of the observation from space which has been addressed in this thesis. In Chapter 3 the observation from space is discussed using an analytical approach to highlight the functional relations between the parameters of the mission. In Chapter 4, after an introduction about the *EUSO* experiment, the Monte-Carlo simulation and reconstruction framework ESAF is described in detail. The results obtained with EUSO Simulation and Analysis Framework (ESAF) are discussed in Chapter 5. The last Chapter is dedicated to the study and characterization of the SiPMs for the possible application to the next generation of UHECR space-based telescopes.

Part I

The Ultra High Energy Cosmic Rays

Chapter 1

The Observation of UHECR

1.1 Status of the field

Cosmic rays are a very wide topic, deeply related to many fields of physics, ranging from particle and nuclear physics to astrophysics and cosmology. The present knowledge on elementary particles was triggered by cosmic rays, with the discovery of the positron in 1932, the muon in 1937, the pion in 1947, and later of the strange particles kaon and Λ-hyperon. Nowadays that the physics at accelerators is starting to fight against both technological and financial limitations, these natural laboratories enjoy renewed interest. Fundamental questions remain however unanswered in cosmic ray physics. From the astrophysical point of view, almost one century after their discovery, we have no definite clue to the origin, acceleration and propagation of cosmic rays, though we recognize that they carry information about our Galaxy, and probably also about the extragalactic space, at, least at the highest observed energies. In a nutshell, we know that cosmic rays at the sea level are mostly $e^{\pm}$, $\mu^{\pm}$, γ, a few hadrons and many ν (the so-called atmospheric neutrinos) with an integrated flux of charged particles of about 200 $m^{-2}s^{-1}$ These are secondary particles generated in Earth's atmosphere by the so-called primary component, whose content at the top of the atmosphere is roughly 90% protons, 8% He nuclei, 1% of heavier nuclei up to iron, 1% $e^{\pm}$ and a small component of of the order of 0.01%. Cosmic rays present an almost featureless energy-spectrum which extends over more than eleven decades up to at least 10^{20} eV, where the flux is lower than one particle per km^2 per century (see Fig. 1.1). The main physical observables are the arrival directions, the chemical composition and energy spectra of the primaries; while at the highest energies also the arrival times

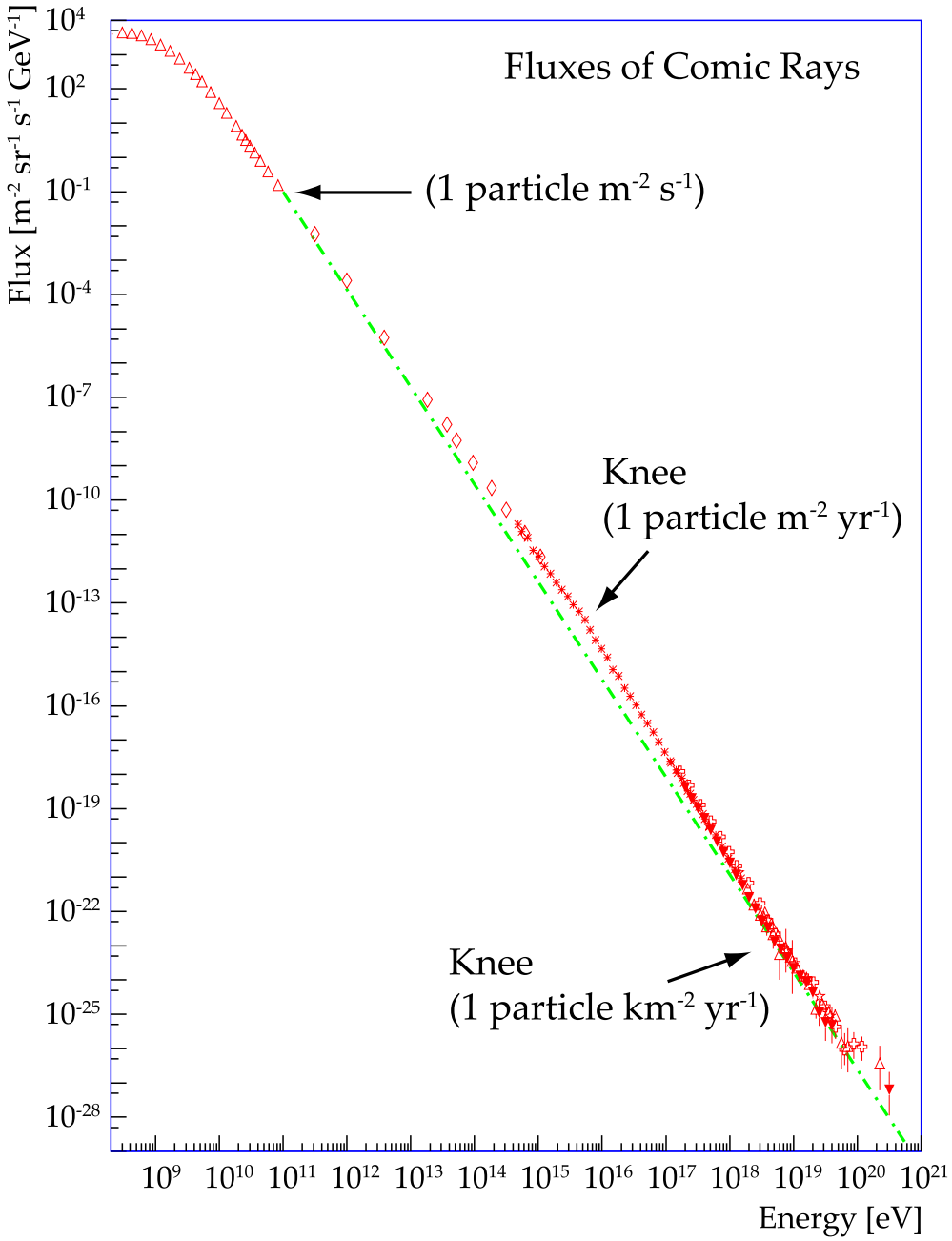

Figure 1.1: Compilation of measurements of the differential energy spectrum of cosmic ray. The dotted line shows an E^3 power-law for comparison. Approximate integral fluxes (per sr) are also shown [15].

provide interesting information. The GeV and sub-GeV energy range is strongly influenced by the Solar magnetic modulation and also includes some contribution of Solar-injected particles. These particles constitute both numerically and energetically the hulk of the cosmic ray primaries, and their deflections in the Earth's magnetic field were historically crucial to understand the charged particle nature of Hess' "Kosmische Strahlung". Nowadays, this range still plays an interesting role for particle physics, in particular for indirect searches of dark matter via its annihilation products: anti-nuclei, positrons, γ-rays, and neutrinos [16, 17, 18]. At higher energies the spectrum behaves like a power-law, ($\mathrm{d}N/\mathrm{d}E \propto E^{-\gamma}$ with $\gamma \simeq 2.7$. The only distinct features are:

i) A change in the index from 2.7 to 3.1 around 3 PeV (knee);

ii) a possible second knee around $4 - 8{\cdot}10^{17}$ eV;

iii) flattening again to $\gamma \simeq 2.7$ at about $5{\cdot}10^{18}$ eV (ankle) (see Fig. 1.1.)

At the 29th International Cosmic Ray Conference in 2005, the HiRes collaboration has also claimed strong evidence (almost 5σ) in favor of a suppression of the flux at E = $5{\cdot}10^{19}$ eV (see also [19]). This awaits further confirmation, but the end of cosmic ray spectrum at energies around 10^{20} eV is theoretically expected.

1.1.1 The Extensive Air Showers

When a cosmic ray strikes the Earth atmosphere a shower of particles is produced, an EAS. At the beginning the number of particles grows until the maximum N_{max} (Fig. 1.2), where the average energy per particle is not enough to sustain the multiplication process. After the maximum the number of particles decreases until the EAS is not completely attenuated. An EAS appears as a disc of particles (the shower front) traveling through the atmosphere at the speed of light. A 10^{19} eV shower produces about $7{\times}10^{9}$ charged particles at its maximum development. Most of the shower particles are very close to an axis defined as the direction of the primary particle. Roughly 80% of the particles are within one *Molière radius* from the shower axis.

$$R_{\mathrm{Molière}} \simeq X_{\pm}\frac{\alpha_{m.s.}}{E_c}. \tag{1.1}$$

where $X_{\pm} \simeq 37$ g/cm^2 is the radiation length in air, $\alpha_{m.s.} \simeq 21$ MeV is the multiple scattering constant and $E_c \simeq 80$ MeV the critical energy in air.

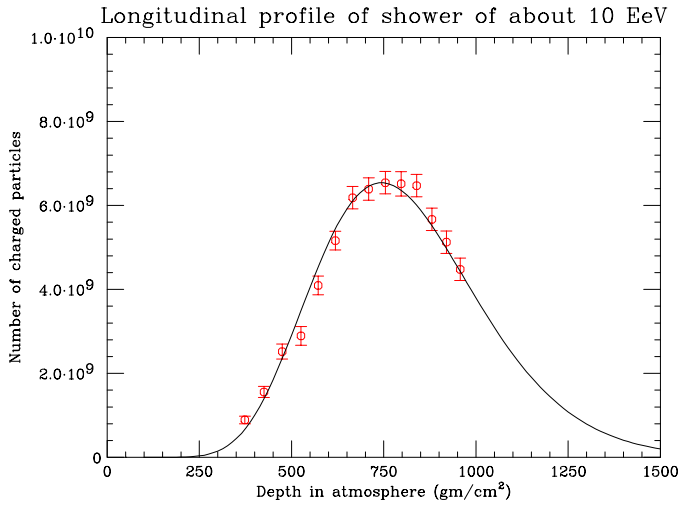

Figure 1.2: Longitudinal development of a 9 EeV shower in the atmosphere. The solid line is an empirical fit to the shower development. The red points are the measurements of the shower development by detection of its nitrogen fluorescence.

Typically this distance is about 100 meters. The EAS has an electromagnetic, and hadronic and a muonic component as sketched in Fig. 1.3. The predominance of one of the components depends on the primary cosmic ray species. Most of the produced particles in each hadronic interactions are π and K mesons. K and $\pi^{\pm}$ decay into μ and ν, thus producing the most penetrating component of the atmospheric showers. The decays of π^0 into photons are the main responsible of the electromagnetic showers of γ and $e^{\pm}$, that constitute the majority of the particles of the shower. The longitudinal evolution of the shower, i.e. the number of charged particles $N_{\pm}$, is a function of the nature and the energy of the primary, naturally described in terms of the shower depth X (*slant depth*).

$$X \equiv \int \mathrm{d}\ell\, \rho(\ell). \tag{1.2}$$

For a ground hitting shower X assumes the form

$$X = \int_{h_{imp}}^{\infty} \mathrm{d}h \frac{\mathrm{d}\ell}{\mathrm{d}h} \rho(h), \tag{1.3}$$

being $\rho(h)$ the atmospheric density profile, h_{imp} the altitude of the impact

point and $l(h)$ is the particle trajectory as a function of the altitude. The general formula for $\mathrm{d}\ell\,/\,\mathrm{d}h$ is

$$\frac{\mathrm{d}\ell}{\mathrm{d}h} = \left(\cos\theta + \frac{\ell}{R_\oplus}\sin^2\theta\right)^{-1} \tag{1.4}$$

but for not too inclined showers, $\theta \leq 70°$, also stands $\frac{\mathrm{d}\ell}{\mathrm{d}h} = \frac{1}{\cos\theta}$.

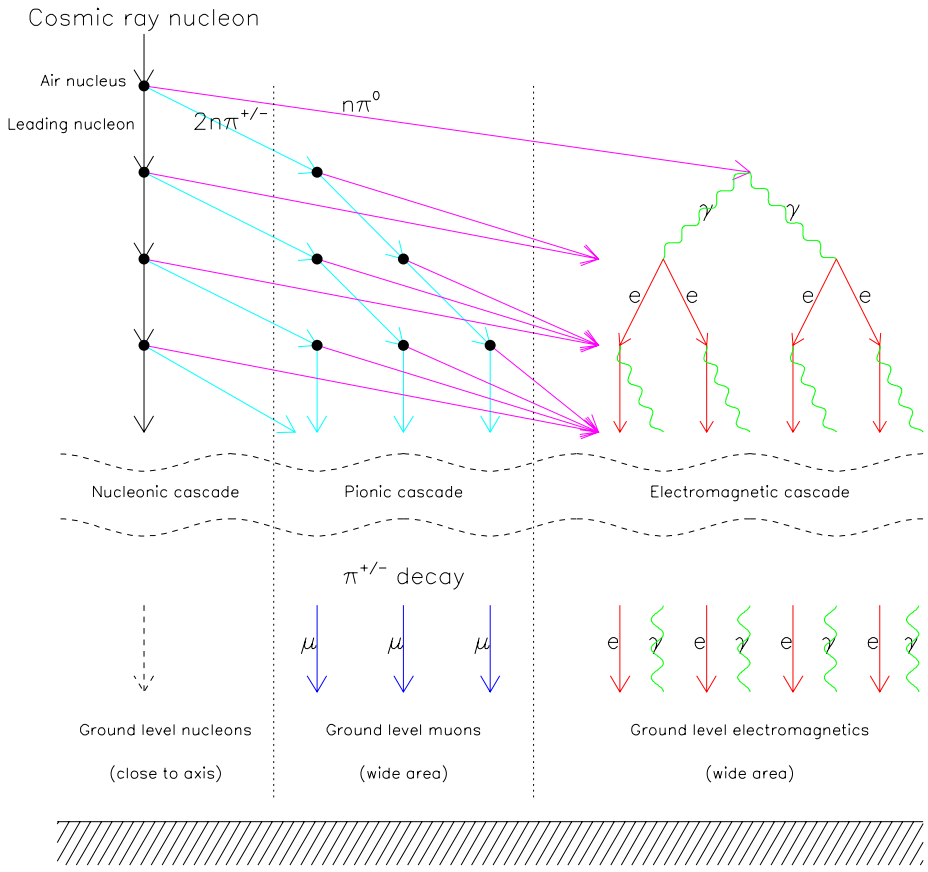

Figure 1.3: Schematic diagram showing the principal extensive air shower cascade processes. An incident cosmic ray nucleon is assumed and the resulting shower divided into three categories: the nucleonic cascade consisting of the surviving primary itself in the guise of a leading nucleon, the pionic cascades and the electromagnetic cascade which is fed by neutral pion decay. From [20].

The energy of the shower can be obtained by integration of the ionization loss in the atmosphere, given by approximately

$$E = \left.\frac{\mathrm{d}E}{\mathrm{d}X}\right|_{E=E_c} \int \mathrm{d}X N_{\pm}(X) \tag{1.5}$$

where $\left.\frac{\mathrm{d}E}{\mathrm{d}X}\right|_{E=E_c} \simeq 2.2\ \mathrm{MeV}/(\mathrm{g/cm^2})$ is the energy loss rate for electrons at the critical energy, $N_{\pm}(X)$ is the number of shower particles at the atmospheric depth. Implicit in this formula is the presumed knowledge of the shape of the longitudinal development outside the range of measurement. Also some energy is not observed in the form of neutrinos and penetrating muons.

Electromagnetic showers

In the electromagnetic UHECRs two base processes concur to the development of the cascade, the pair production and the Bremsstrahlung. At energies higher than 1 GeV the cross sections of both processes are almost constant against the energy. Below the critical energy E_c, the ionization losses for electrons and positrons and the Compton and photoelectric effects for photons, prevail on the other interactions. Actually the critical energy is defined as the energy at which the ionization losses equal the radiation losses. The evolution of an electromagnetic shower is fixed by the radiation length for Bremsstrahlung $X_{\pm}$

$$\left.\frac{\mathrm{d}E}{\mathrm{d}X}\right|_{\mathrm{rad}} = \frac{E}{X_{\pm}} \tag{1.6}$$

$X_{\pm}$ can be parameterized as

$$X_{\pm} \approx 180 \frac{A}{Z^2}\ \mathrm{g/cm^2} \tag{1.7}$$

being A the mass number and Z the charge number. The empirical relation for the critical energy E_c is

$$E_c \approx \frac{800\ \mathrm{MeV}}{Z + 1.2} \approx 80\ \mathrm{MeV\ in\ air} \tag{1.8}$$

The average free path for the Bremsstrahlung is $X_{\pm}$, while for the pair production is $9/7 X_{\pm}$ [21]. The electromagnetic longitudinal profile is well described by the Greisen formula [22],

$$N_{\pm}(X) = \frac{0.31}{\sqrt{T_{\mathrm{max}}}} e^{T} s^{-3T/2}, \tag{1.9}$$

where $T \equiv \frac{X}{X_\pm}$ is the atmospheric slant depth measured in radiation lengths, $T_{\max} \equiv \frac{X_{\max}}{X_\pm}$ and the shower age $s \equiv 3T/(T + 2T_{\max})$. The Heitler model of an electromagnetic cascade [23] gives an intuitive understanding of the basic properties of the EAS, whose development is figured as a sequence of generations. At each generation a photon converts into an $e^\pm$ pair and each $e^\pm$ is assumed to emit a γ, doubling the size of the shower. The shower maximum is

$$N_{\max} = \frac{E}{E_c} \tag{1.10}$$

and occurs after n generations when $N_{\max} = 2^n$ or $n = \log(E/E_c)/\log 2$. The maximum occurs at $X_{\max} = nX_\pm \log 2$.

Hadronic showers

Hadronic interactions are more complex than electromagnetic ones; an UHE hadron can generate a multitude of secondary particles interacting with the nuclei of the atmosphere. The nucleus can be considered as a solid disc of radius R. The cross section of the interaction is $\sigma_{\text{int}} = \pi R^2$ or $A^{2/3}$, as the fenomenology shows that $R \propto A^{1/3}$. The nuclear interaction length in air is

$$\Lambda = \frac{\langle A \rangle}{N_A \sigma_{\text{int}}} \sim \langle A \rangle^{1/3} \tag{1.11}$$

where N_A is the Avogadro's number and $\langle A \rangle$ is the average mass number of the air. Due to the multitude of possible processes during the shower creation, the hadron energy is transferred into several groups, each of them with their own systematic energy dependencies, and the distribution into the groups is subject to fluctuations. Part of the energy goes into charged particles. Isospin symmetry suggests that at each generation $1/3$ of the energy is transformed into an electromagnetic cascade (mainly via π^0 decay), and after n generations, only $(1/3)^n$ of the energy remains in the hadronic channels, that eventually will go in ν and μ, accounting for $\simeq 7-10\%$ of the initial energy. The longitudinal extension of the shower is determined by Λ, which typically depends on the energy, the cross section and on the inelasticity[1]. The lateral distribution depends on the angular distribution of secondary particles, which have transverse momenta of the order of 0.35 GeV. A widely used longitudinal parameterization for

[1] defined as $K = \frac{E_0 - E'}{E_0 + M}$, with E_0 the incoming particle energy, E' the energy of the nucleon after the collision and M the mass of the atmosphere particles.

hadronic EAS is the *Gaisser-Hillas* function:

$$N^{\pm}(X) = N^{\pm}_{\max}\left(\frac{X - X_0}{X_{\max} - X_0}\right)^{\frac{X_{\max}-X_0}{\lambda}} e^{\frac{X_{\max}-X_0}{\lambda}} \tag{1.12}$$

being $\lambda \simeq 65$ g/cm^2 [24], X_0 the radiation length of the primary in air and $X_{\max}$ the depth of the maximum. $X_{\max}$ depends strongly on the multiplicity of the first interaction. In general light nuclei produce EAS with an $X_{\max}$ deeper than heavy nuclei.

1.1.2 Chemical composition

While indirect detection of EAS is a relatively easy task, extracting precise information has proved exceedingly difficult because of the highly indirect method of measurement. Probably the most difficult parameter to extract is the primary particle species. The CR primary particles must be stable and, if charged, heavy enough not to lose energy too easily in the Galactic and intergalactic media. These conditions only allow nuclei (including protons), photons and neutrinos as standard model candidates. One way to distinguish photon and hadron primaries in a statistical way is to compare the vertical to inclined EAS rate, a technique which exploits the attenuation of the electromagnetic component for large slant depths. This technique was employed in [25] using the Haverah Park data to conclude that above 10^{19} eV less than 48% of the primary UHECRs can be photons and above $4{\cdot}10^{19}$ eV less than 50% can be photons (both bounds at the 95% confidence level, C.L.). At present the most stringent upper limit on the photon fraction comes however from the study of $X_{\max}$: Auger preliminary data imply that no more than 26% of events at $E \geq 10^{19}$ eV can be induced by photons [26]. The absence of clear photon or neutrino candidate events at present is not unexpected in astrophysical models, since ν and γ are only produced as secondary particles. On the other hand, this is already challenging for exotic models of UHECR production, such as the top-down scenarios, predicting a large photon fraction in the primaries, or the Z-burst scenarios, where a large photon fraction is accompanied by a huge neutrino flux.

Up to now, all the indirect evidence suggests that UHECRs are mostly hadronic particles. Unfortunately distinguishing between a proton and a heavier nucleus is extremely difficult at the highest energies. A powerful way, at least in principle, to determine the primary species is achieved by measuring the correlation between different components, e.g. number of $e^{\pm}$ vs. number of $\mu^{\pm}$. Since muons are mainly produced via nuclear processes, it is clear that, for a fixed energy E, the relative number of muons

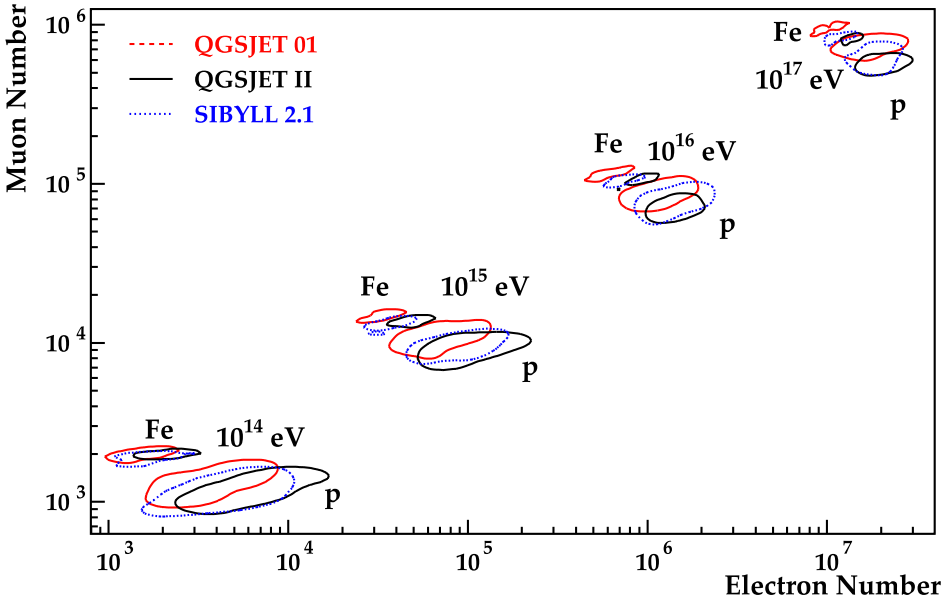

Figure 1.4: Number of muons vs. number of electrons at different lab energies as resulting from proton and iron EAS based on different hadronic interaction models [27].

for an hadronic primary is significantly larger than for a photon primary. But more muons are also expected when a heavier nucleus triggers the shower. The superposition model implies that heavy nuclei EAS develop and attenuate earlier in the atmosphere, since the energy per nucleon is less. Nucleons of lower energies produce lower energy mesons, which decay more often than the high energy ones, thus producing more muons. Quantitatively, the number of muons grows with the primary proton energy E roughly as $N_\mu^p = \alpha E^\beta$, with α and β depending only weakly on the energy. The superposition model tells us that

$$N_\mu^A \simeq A \times \left(\frac{E}{A}\right)^\beta = A^{1-\beta} N_\mu^p. \tag{1.13}$$

Simulations show that, at ultra-high energies, $\beta \simeq 0.93$ and thus that an iron nucleus produces a shower with around 30% more muons than a proton shower of the same energy. Unfortunately, the uncertainty of hadronic models makes this method very model-dependent, especially at high energies (see Fig. 1.4). A more robust method for the estimate of the

primary properties is based on the determination of the depth of maximum longitudinal development of the shower, $X_{\max}$.

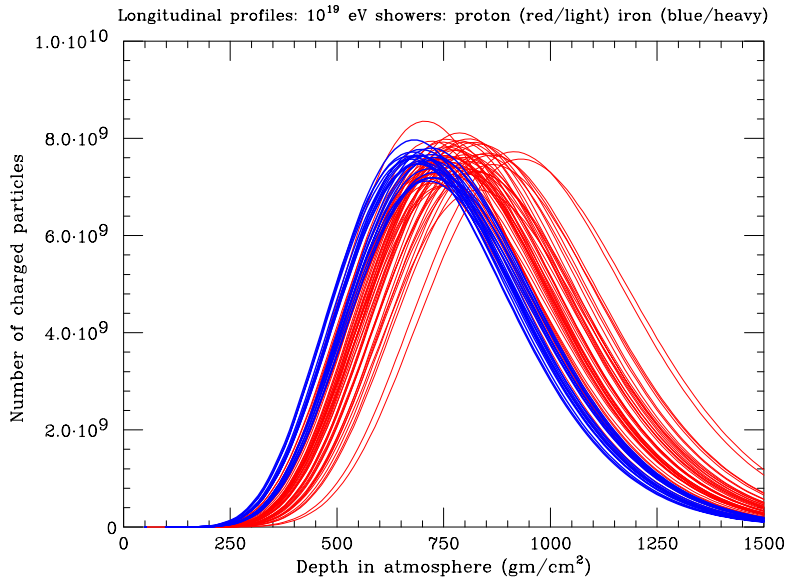

Figure 1.5: Simulated shower profiles for proton (light profiles) and iron (heavy profiles).

The quantity $X_{\max}$ increases with primary energy as more cascade generations are required to degrade the secondary particle energies; for showers of a given total energy, heavier nuclei have smaller $X_{\max}$, because the shower is already subdivided into A nucleons when it enters the atmosphere. Specifically, the way the average depth of maximum $\langle X_{\max} \rangle$ changes with energy depends on the primary composition and particle interactions according to

$$\langle X_{\max} \rangle = D_e \ln\left(\frac{E}{E_0}\right), \tag{1.14}$$

where D_e is the so-called elongation rate and E_0 is a characteristic energy that depends on the primary species [28]. For a nucleus of mass number A, once again the superposition principle suggests the relation $E_0 \propto A$, that indeed is approximately confirmed by simulations. In fluorescence detectors, $\langle X_{\max} \rangle$ and D_e can be determined directly from the longitudinal shower profiles; E_0 and thus the composition can be extracted after estimating E from the total fluorescence yield, i.e. the integral over X of the Eq.(1.12). Moreover, the fluctuation expected around the average

depth $\langle X_{\max} \rangle$ are larger for protons than for heavy nuclei, whose showers are approximately an average of A single nucleon showers (see Fig. 1.5). The status of present analysis (assuming for simplicity a bi-modal composition proton-iron) is summarized in the "estimated iron fraction" shown in Fig. 1.7 (see also [29]). We can recognize some trend suggesting a transition to lower $\langle A \rangle$ moving from energies 10^{17} eV to 10^{19} eV, but it is clear that in view of the low statistics at the end of the spectrum and the wide variety of uncertainties in these experiments, one may conservatively say that this is not a closed issue. A natural question suggested by the previous

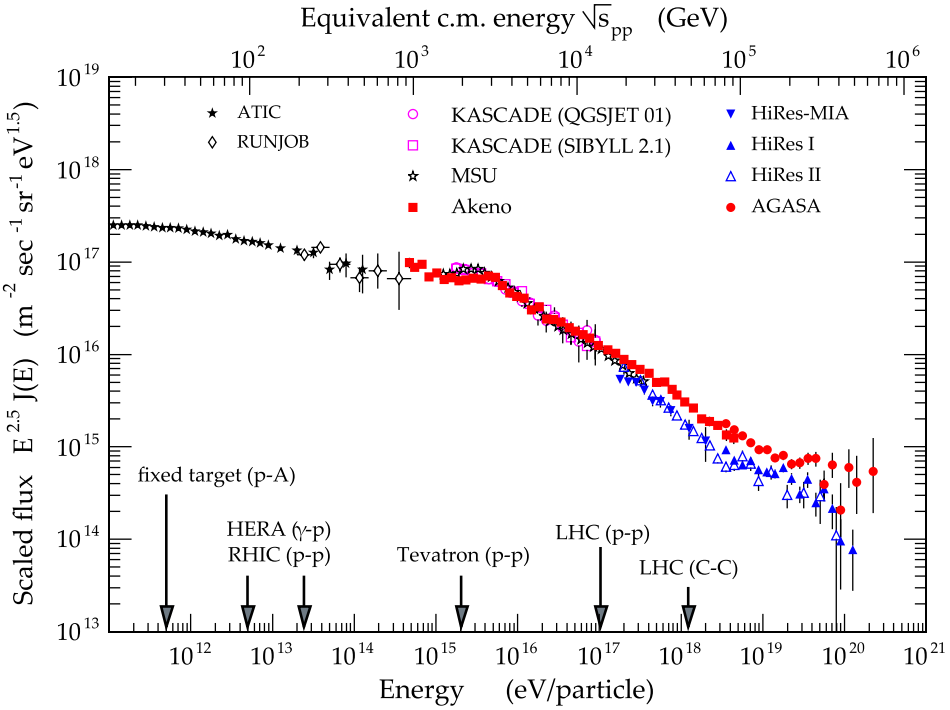

Figure 1.6: Primary cosmic ray flux scaled with $E^{2.5}$ from [27]. A selection of old and recent measurements is shown, included for reference. The energy scale of recent and future accelerators is also shown for comparison.

discussion is why the extraction of precise information on EAS primaries, and the chemical composition in particular, is so challenging. The ultimate reasons are that:

1. the first generations of particles in the cascade are subject to inherent fluctuations and consequently this limits the event-by-event resolution of the experiments;

2. the center-of-mass energy of the first few cascade steps is well beyond any reached in collider experiments, as also shown in Fig. 1.6. Therefore, one needs to rely on hadronic interaction models that attempt to extrapolate our understanding of particle physics.

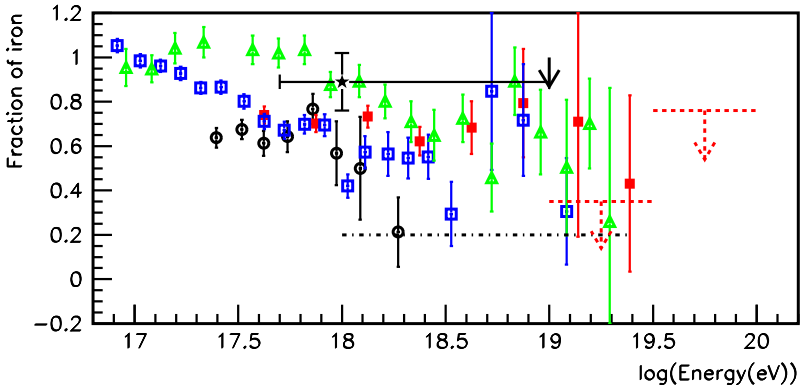

Figure 1.7: Iron fraction in various experiments [30]: Fly's Eye (triangles), AGASA A100 (full squares), AGASA A1 (empty squares) using SIBYLL 1.6 and Haverah Park, using QGSJET (circles)

Reliable models are difficult to achieve, since the inelastic part of hadronic interactions of interest is dominated by hadronic emission at limited trans-verse momentum, $\langle p_T \rangle \sim 0.3$ GeV. Differently from the hard scattering at high p_T which can be predicted relatively well by perturbative QCD, no exact way is known to calculate the bulk of soft, non-perturbative interactions, and one has to rely on more or less phenomenological models. These models are calibrated with the sparse accelerator data available in the forward region, and then extrapolated by one or two decades in the center of mass energy to interpret the EAS data. At present, the different approaches used to model the underlying physics of pp collisions show clear differences in multiplicity predictions which increase with rising energy [30]. Experimental programs specifically devoted to the study of cross sections in the forward region are ongoing. For example, exploiting LHC, the most energetic accelerator nowadays in construction at CERN, experiments like LHCf [31] or TOTEM [32] should be able to validate the EAS models at least up to equivalent lab energies of 10^{17} eV (CM energy 14 TeV) for protons. A few years later, much larger energies should be attained in lead-lead ion collisions, and a dedicated heavy ion detector, ALICE, will also operate at this collider.

1.1.3 Large scale anisotropies

Since cosmic rays can not propagate very far at trans-GZK energies, and their deflections are expected to be relatively small in most of the sky, anisotropy patterns are expected to show up in UHECRs, provided enough statistics is collected. Cosmic ray air shower detectors which experience stable operation over a period of a year or more have a uniform exposure in right ascension (R.A.). A traditional technique to search for large scale anisotropies is then to fit the R.A. distribution of events to a sine wave with period $2\pi/m$ (m^{th} harmonic) to determine the components (x, y) of the Rayleigh vector [33]

$$x = \frac{2}{N}\sum_{i=1}^{N}\cos(m\alpha_i), \quad y = \frac{2}{N}\sum_{i=1}^{N}\sin(m\alpha_i) \tag{1.15}$$

where α_i is the R.A. of the i-th event. The m^{th} harmonic amplitude of N data is given by the Rayleigh vector length $\mathcal{R} = (x^2 + y^2)^{1/2}$. The expected length of such a vector for values randomly sampled from a uniform phase distribution is $\mathcal{R}_0 = \frac{2}{\sqrt{N}}$. The chance probability of obtaining an amplitude with length larger than that measured is $p(> \mathcal{R}) = e^{k_0}$, where $k_0 = \mathcal{R}^2/\mathcal{R}_0^2$. Until now, all experiments to date have reported results consistent with an isotropic sky on large scales. A study [34] of the angular power spectrum of the distribution of trans-GZK cosmic rays ($E > 10^{19.6}$ eV) as seen by the AGASA and the *Sidney University Giant Air-shower Recorder* (SUGAR) experiments show no departures from either homogeneity or isotropy on an angular scale greater than 10°. Analogously, HiRes data are also statistically consistent with an isotropic distribution [35].

1.1.4 Small scale clustering

Although there seems to be a remarkable agreement among experiments on the large scale isotropy of the data, this is certainly not the case considering the two-point auto-correlation function on a small angular scale, i.e. at a scale comparable with the angular resolution of the experiment. The analysis carried out by the AGASA collaboration indicate that the clustering of events on the celestial sky occurs at considerably higher than chance coincidence at separation angles less than the angular resolution $\theta_{\rm min} = 2.5°$ [37, 8]. AGASA finds indeed four doublets and one triplet among the 57 events re-ported with mean energy above $10^{19.6}$ eV, with probability of observing these clusters by chance coincidence for an isotropic distribution estimated to be smaller than 1% (see Fig. 1.9).

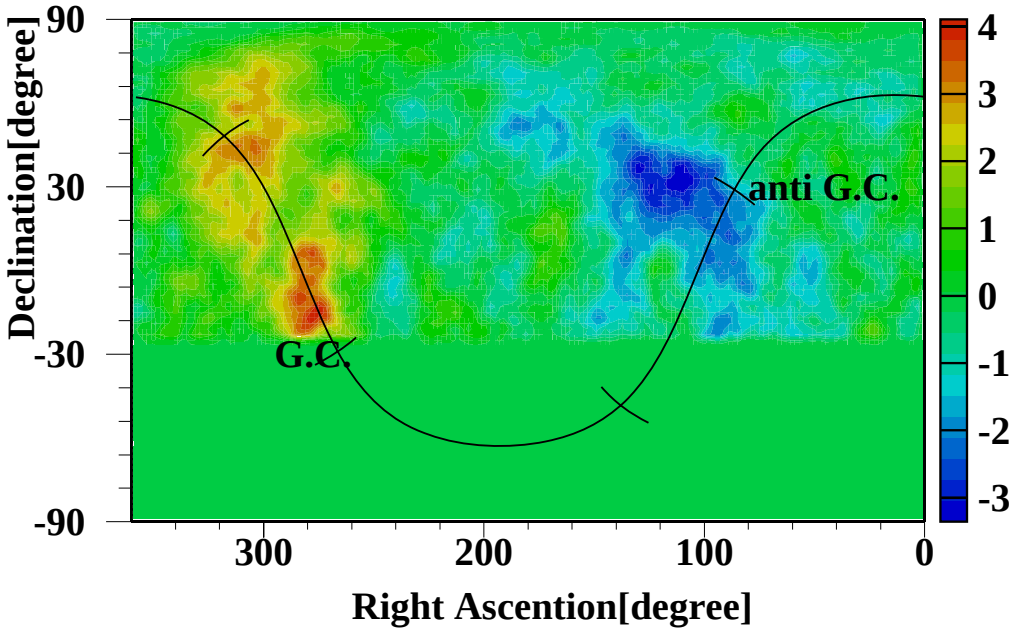

Figure 1.8: Map of ratio of the number of observed events to expected ones in equatorial coordinate in the energy range $10^{17} - 10^{18}$ eV. Solid line shows Galactic Plane. G.C. marks the galactic center. The bottom region (solid green) is not observable by AGASA. From Ref. [36].

A data set including events from other experiments has also been studied [38]: six doublets and two triplets out of 92 events with energies above $10^{19.6}$ eV were found. The angular two-point correlation function of a combined data sample of AGASA ($E > 4.8{\cdot}10^{19}$ eV) and Yakutsk ($E > 2.4{\cdot}10^{19}$ eV) was analyzed [39]. For a uniform distribution of sources, the probability of chance clustering is reported to be as small as 4×10^{-6}. Far from confirming what seemed a fascinating discovery, the analysis reported by the *High Resolution Fly's Eye* (HiRes) Collaboration showed that the data are consistent with no small scale anisotropy among the highest energy events [40, 41]. The preliminary data of the Auger Observatory, though being searched only for single sources; gave negative result as well [42]. The discovery of such clusters would be a tremendous breakthrough for the field, but the case for them is not yet proved. In order to obtain a meaningful statistical significance for such an analysis, it is important to define the search procedure a priori in order to prevent it from being biased by the particular data set considered. Very recently, with the

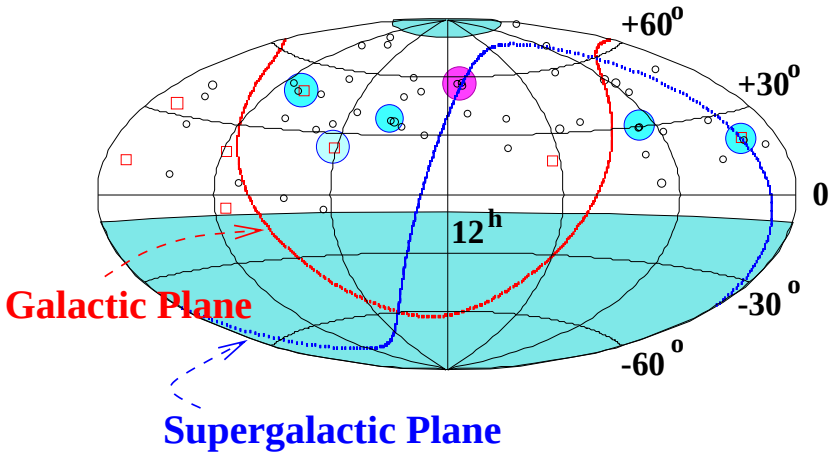

Figure 1.9: Arrival directions of cosmic rays with energies above $4{\cdot}10^{19}$ eV in equatorial coordinates. Red squares and green circles represent cosmic rays with energies of $> 10^{20}$ eV , and $(4-10)\times 10^{19}$ eV, respectively. Circles enclose the multiplets.

aim to avoid accidental bias on the number of trials performed in selecting the angular bin, the original claim of the AGASA Collaboration [37] was re-examined considering only the events observed after the claim [43]. This study showed that the evidence for clustering in the AGASA data set is weaker than was previously claimed, and consistent with the null hypothesis of isotropically distributed arrival directions. Summing up, the clustering on small angular scale at the upper end of the spectrum remains an open question, and the increase in statistics and improved resolution attainable with the *Pierre Auger Observatory* (PAO) is awaited to solve the issue.

1.2 Experimental techniques

1.2.1 Ground Arrays

Direct detection of shower particles is the most commonly used method, and involves constructing an array of sensors spread, often in a regular grid, over an appropriate area to sample particle densities as the shower arrives on the ground. The area required relates to the rate of events being studied and for UHECRs must be many square kilometers. The separation of the detectors is chosen to match the scale of the footprint of the shower

at the observation level. For UHECRs, this distance is typically many hundreds meters. All of the arrays built to detect cosmic rays above 10^{19} eV have been located between 800 g/cm^2 and sea level. This is appropriate, as the average maximum depth of showers of these primaries is about 750 g/cm^2 and it is effective to study showers close to or beyond shower maximum. With an array of particle detectors, the direction of the shower axis, and hence of the primary cosmic ray, is deduced from the relative arrival times of signals at a minimum of three non-collinear detectors. The shower disc is assumed to sweep across the array at the velocity of light and the relative arrival times are measured. As a first approximation, the extreme front of the disc is treated as if it were planar. The shower disc has a thickness that increases from a few nanoseconds close to the shower core up to several microseconds at distances beyond 1 km. Thus a large-area detector is more likely to intercept a particle or photon arriving early in the shower front and so enhance the accuracy of directional reconstruction. With giant arrays the arrival direction has been measured to an accuracy between 1° and 5°. Measurement of the direction of the shower axis is the first step toward finding the impact point of the axis of the shower on the ground, the core. The raw data associated with each event, in addition to the relative arrival times, consist of a set of densities from the detectors of the array. Fitting to these densities the lateral distribution function, a function that describes the falloff of particles density with the distance from the shower core and that depends on the detectors used, one can find the shower core. After the core position has been found, the assumption of a planar description of the shower front can be modified to allow for the fact that shower particles are not created at a point infinitely far away from the detectors. It has been found that for the showers that are of interest here a spherical front with a radius of curvature of several kilometers fits the data. After the core has been determined the shower size can, in principle, be obtained from the fit to the lateral distribution function. However the shower size produced by primaries of a particular energy will fluctuate from shower to shower because of differences in the stochastic development of the cascades, so this is not a good estimator for the energy of the primary particle. Hillas [44, 45] showed that fluctuations of the density of shower particles far from the core are quite small and hence the density depends only on primary energy. Then, a better quantity to use in order to estimate the primary energy is the density of the registered shower component at a relatively large distance from the shower axis. Several Monte-Carlo simulations of cascade development have confirmed this, and it is now widely accepted that the density far from the shower axis depends rather little on the hadronic interaction model or the primary

composition and may be used reliably as an energy estimator. The ground array technique is the most used one and there are many experiments around the world exploiting it to detect UHECRs:

Volcano Ranch was the first experiment that made measurements of UHECRs in the late 1950's. It was located at Volcano Ranch in New Mexico and the detector consisted in an array of 19 scintillation counters spaced on a 884 m hexagonal grid that covered about 8 km^2. Data from the Volcano Ranch array yielded the first measurements of the energy spectrum of cosmic rays above 10^{18} eV, giving the earliest hint of a scattering of the spectrum in that region, a hint that took over 20 years to confirm convincingly. The most energetic event was assigned an energy of 10^{20} eV, an energy that was subsequently revised to $1.4{\cdot}10^{20}$ eV. This event remains one of the largest ever recorded and, interestingly, was reported before the discovery of the cosmic microwave background radiation and the subsequent prediction of a spectrum cutoff.

Haverah Park ceased operation in 1987 after 19 years of operation. The experiment was operated at Haverah Park in England and the detector array consisted in deep water Cherenkov detectors distributed over an area of approximately 12 km^2. Restriction on land access made it impossible to position the detectors on a uniform grid. In the ongoing analyses of data, primary energies are derived from the particle density at 600 m form the shower axis, $\rho(600)$. Random errors in the determination of $\rho(600)$ are less than 30%. The energy threshold was approximately $6{\cdot}10^{16}$ eV. The angular resolution of the array is of about 3°.

Yakutsk This array, located in Siberia and in operation from 1972, is composed of plastic scintillators arranged on a triangular grid. It began taking data in 1970 and was developed to cover an area of 18 km^2 in 1974. There are three nested arrays. The inner-most, of area 0.026 km^2, uses 19 scintillation detectors and is surrounded by 43 similar detectors on a 500 m grid covering 10 km^2. A further 17 scintillation detectors surround the second array on a spacing of 1 km. Within 1 km of the center of the array are 8 muon detectors with an energy threshold of 0.5 GeV. In 1995 the Yakutsk group contracted their array to 10 km^2 so that detailed studies of shower structure could be made near 10^{19} eV, where they have reported a change of shower characteristics.

SUGAR is the only giant array that operated in the Southern Hemisphere. It was built by the University of Sydney at Narribri in Australia, close to sea level. The array consisted in 54 stations deployed over 60 km^2. Each station was autonomous, with its own local power source and local intelligence. Data were logged on audio tape recorders from which tapes were collected at weekly intervals and sent to Sydney for analysis. Unfortunately the spacing between the detectors, typically one mile (1.61 km), proved to be too great and, even in the largest events, the number of stations that registered measurable densities was small. For the ten largest events the mean number of stations struck was only 4.7, with a mean core error greatly in excess of 100 m. Furthermore there were also some problems in the design of the electronics and thus the precision achieved contrasts poorly with that of work from the other arrays, and one should be cautious about taking the energies ascribed to the Sydney events above $5{\cdot}10^{19}$ eV as providing definitive evidence against a cutoff in the cosmic ray energy spectrum. The data are mainly useful because they form a unique set for arrival direction studies in the Southern Hemisphere, even if the angular resolution is not very good, $\sim 6°$. Moreover, the novel method of data recording provides the template for a new approach to a giant array (the Pierre Auger Observatory), which takes advantage of 30 years of technological development.

AGASA is the largest array constructed so far, covering an area of 100km2 at Akeno in Japan. The array consists of 111 scintillation detectors deployed with an inter-detector spacing of about 1 km. Muon detectors of varying sizes are installed at 27 of the 111 detector sites. Data acquisition was started in 1990. In the southeast corner of AGASA, there is a densely packed array of detectors covering 1km2. This has been operated since 1979. There are arrays with detector separations of 3, 15, 30, 60, and 120 m. The proton-air inelastic collision cross section, the energy spectrum, and the muon energy spectrum derived from the shower size spectrum of horizontal air showers have been determined with these arrays from $3{\cdot}10^{14}$ eV to $3{\cdot}10^{18}$. The energy spectrum is connected to the higher-energy region using AGASA. The typical angular resolution is 3° and 1.5° for 10^{19} and 10^{20} eV showers, respectively. To investigate the relative proportion of electrons, photons, and muons far from the core of giant air showers, for the design of the next generation of experiments, three detectors having two scintillators sandwiching a lead plate of 1 cm thickness are installed. Two prototype water Cherenkov detectors for the Auger

Project are also being operated.

1.2.2 Fluorescence Telescopes

The detection of secondary photons from extensive air showers represents a complementary technique with respect to the ground array. As an EAS develops in the atmosphere it dissipates much of its energy by exciting and ionizing air molecules along its path. Excited nitrogen molecules fluoresce producing ultraviolet radiation.

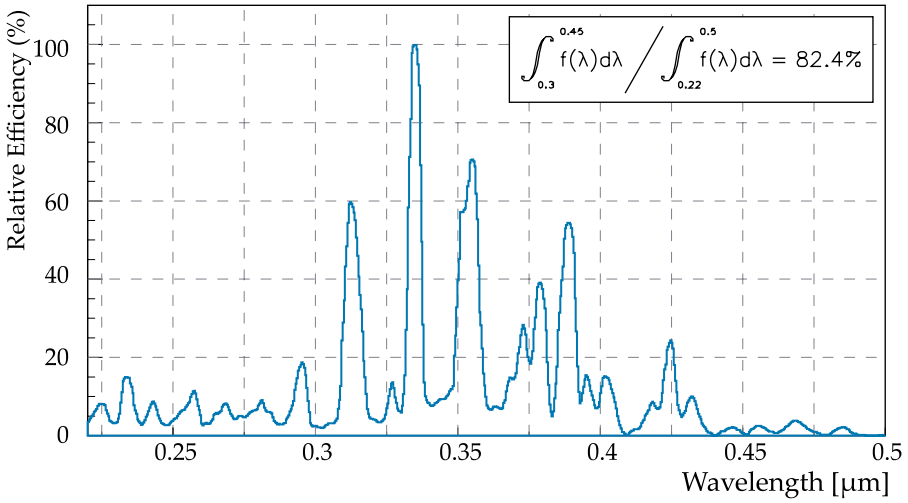

Figure 1.10: Nitrogen fluorescence spectrum in the $300 \div 450$ nm band.

The shower development appears as a rapidly moving spot of light describing a great circle path across the night sky background of starlight, atmospheric airglow, and man-made light pollution. The angular motion of the spot depends on both the distance and the orientation of the shower axis. The apparent brightness of the spot depends on the instantaneous number of charged particles present in the shower, but it is also affected by Cherenkov contamination and atmospheric scattering. The fluorescence trail is emitted isotropically with an intensity that is proportional to the number of charged particles in the shower. The ratio of the energy emitted as fluorescence light to the total energy deposited is less than 1%, hence low energy ($< 10^{17}$ eV) showers can hardly be observed. Furthermore, observations can only be done on clear moon-less nights, resulting in an

average 10% duty cycle. The emitted light is typically in the $300 \div 400$ nm ultraviolet range to which the atmosphere is quite transparent.

A fluorescence eye consists of several large light collectors or telescopes which image regions of the sky onto clusters of light sensing and amplification devices. The basic elements of the telescope are the diaphragm, which defines the telescope aperture, the spherical mirror that must be dimensioned to collect all the light entering the diaphragm in the acceptance angular range, and the camera which consists of an array of photomultiplier tubes (PMTs) positioned approximately on the mirror focal surface. The showers development is detected as a long, rather narrow sequence of hit PMTs. The first stage in the shower reconstruction is the determination of the shower-detector plane, using a fit to the eye's hit tube directions. In the second stage of track reconstruction, the orientation and position of the shower axis within the shower detector plane are determined. Once the trajectory has been found, the next step is to use the PMT signal information to determine the shower size, profile and total energy. One of the advantages of the fluorescence method is its ability to measure the maximum depth of the shower, $X_{\max}$, directly on a shower-by-shower basis. $X_{\max}$ distributions have given important results concerning primary composition (see Sec. 1.1.2). The fluorescence technique has been first implemented only in the Dugway desert by the Fly's Eye group from the University of Utah. Following a successful trial at Volcano Ranch, the Utah group built a device containing two separated Fly's Eyes made up of 880 and 460 PMTs, 3.3 km apart. The two eye configuration monitored the sky from 1986 to 1993. The first detector, Fly's Eye I, had full operation since 1981. It was made of 67 telescopes with diameter 1.5 m and spherical curvature, each with 12 o 14 PMTs at the focus. The mirror were arranged so that the entire night sky was imaged, with each PMT viewing a hexagonal region of the sky of about 5°. Fly's Eye II was made of 36 mirrors of the same design. The detector viewed only half of the sky in the direction of Fly's Eye I. As an up-scaled version of the Fly's Eye, the HiRes detector has being running since the end of 1999. It uses 14 spherical telescopes of 2 m diameter to collect the light from a 0.95 sr portion of the sky. The image plane of each telescope is populated with an array of 256 hexagonal PMTs, giving for each pixel a sky coverage of about 1°.

1.2.3 Running and future experiments

PAO [20, 46] is designed to work in a hybrid mode, employing fluorescence detectors overlooking a ground array of deep water Cherenkov radiators. During clear, dark nights, events will be simultaneously

observed by fluorescence light and particle detectors at ground level. The PAO is expected to measure the energy, arrival direction and primary species with unprecedented statistical precision. It will eventually consist of two sites, one in the Northern hemisphere and one in the Southern, each covering an area of 3000 km^2 and consisting of 1600 particle detectors overlooked by 4 fluorescence eyes. The overall acceptance (two sites) is 14000 $km^2 \cdot sr$. The surface array stations are cylindrical water Cherenkov detectors with area 10 m^2, spaced 1.5 km from each other in a hexagonal grid. Cherenkov radiation emitted by charged particles penetrating the detector is read out by 3 PMTs. The output signal is digitized by flash ADCs, with the aim of separating the electromagnetic signal (low energy electrons and photons) from the muons crossing the tank. Event timing is made possible via global positioning system (GPS) satellites with a precision of a few tens of ns. Communication between the stations is achieved using radio signals by methods similar to mobile telephone techniques. The stations are powered by solar panels and batteries which allow autonomous operation. The configuration of the fluorescence detectors is arranged to optimize the hybrid detector performance. The number of eyes and their location on the site are chosen so that all showers of energy $> 10^{19}$ eV that hit the surface array are seen by at least one eye. A further constraint comes from the need to limit the systematic error in the measurements deriving from uncertainty in the attenuation length of the atmosphere traversed by the light in its path from shower to detector. The optimal configuration was determined by Monte-Carlo simulation, guided by the orographic constraints on the site. The base-line design of the detector includes 4 fluorescence eyes, each comprised of six telescopes with diameter 1.7 m in which each pixel images about 1.5° of the sky. The angular and energy resolution of the ground array (without coincident fluorescence data) are typically less than 1.5° and less than 20%, respectively. Golden events, events detected by both methods simultaneously, will have a directional reconstruction resolution of about 0.3° for energies near 10^{20} eV. If an event trigger is assumed to require 5 detectors above threshold, the array is fully efficient at 10^{19} eV. In three years of running, the surface arrays in both hemispheres, operating 24 hours per day, will collect more than 1000 showers above $4 \cdot 10^{19}$ eV with approximately uniform sky exposure. This will enable a straightforward search for correlations with discrete sources and also a sensitive large scale anisotropy analysis. In addition, PAO offers a window for neutrino astronomy above 10^{17} eV. For standard neutrino interac-

tions in the atmosphere, each site of PAO reaches ~ 15 km^3·sr·w.e. of target mass around 10^{19} eV, which is comparable to other neutrino detectors being planned.

Telescope Array The Telescope Array will comprise a collection of fluorescence detectors dispersed over a large area near Salt Lake City, Utah [47]. Ten observational stations separated from each other by $30-40$ km are planned, each station containing 40 telescopes of 3 m diameter. An imaging camera with 256 PMTs (each one covering about 1° of sky) will be installed on the focal plane of each telescope. The effective aperture of the array will be approximately 5000 km^2 sr for 10^{20} eV particles assuming a 10% observation duty factor. This aperture is around 30 times larger than the existing AGASA ground array. The energy, arrival direction, and shower maximum will be determined with an accuracy of 6%, 0.6°, and 20 g/cm^2, respectively. In addition, the Telescope Array will observe high energy gamma rays from point sources in the sub-TeV energy region. Gamma rays will be distinguished from the large hadronic background using the imaging patterns observed with many telescopes.

Chapter 2

Origin of the UHECRs

2.1 Propagation

Thirty seven years ago, Penzias and Wilson [48] reported the discovery of the cosmic 2.7 K thermal blackbody radiation which was produced very early on in the history of the universe and which led to the undisputed acceptance of the "big bang" theory of the origin of the universe. Much more recently, the Cosmic Background Explorer (COBE) and Wilkinson Microwave Anisotropy Probe (WMAP) satellite confirmed this discovery, showing that the CMB has the spectrum of the most perfect thermal blackbody known to man. The same data also showed that this radiation (on angular scales $> 7°$) was isotropic to a part in 10^5 . The perfect thermal character and smoothness of the CMB proved conclusively that this radiation is indeed cosmological and that, at the present time, it fills the entire universe with a 2.725 K thermal spectrum of radio to far-infrared photons with a density of $400\ \mathrm{cm}^{-3}$. Shortly after the discovery of the CMB, Greisen [49] and Zatsepin and Kuzmin [50] predicted that pion-producing interactions of UHECR protons with CMB photons of target density $400\ \mathrm{cm}^{-3}$ should produce a cutoff in their spectrum at energies greater than 50 EeV. This predicted effect has since become known as the GZK effect.

2.1.1 Protons and Nuclei

Three mechanisms contribute to the energy losses of ultra high energy protons, the photopion production, responsible for the GZK effect, the Pair Production by Proton (PPP) and the expanding universe redshift . All the other processes are negligible except for the galactic centers.

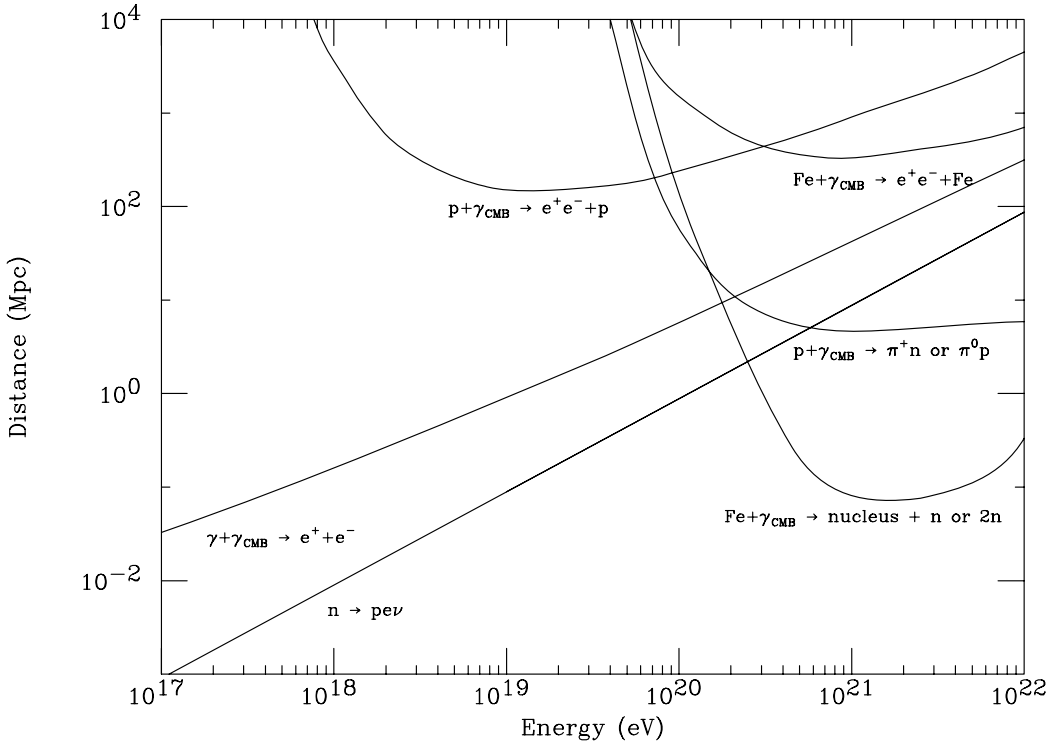

Figure 2.1: Panorama of the interactions of possible cosmic primaries with the CMB. Curves marked by "$p + \gamma_{\mathrm{CMB}} \rightarrow e^+e^- + p$" and "$\mathrm{Fe} + \gamma_{\mathrm{CMB}} \rightarrow e^+e^- + p$" are energy loss lengths: the distance for which the proton or Fe nucleus loses 1/e of its energy due to pair production. The curve marked by "$p + \gamma_{\mathrm{CMB}} \rightarrow \pi^+ + n$ or $\pi^0 p$" is the mean free path for photo-pion production of a proton on the CMB. The curve marked "$\mathrm{Fe} + \gamma_{\mathrm{CMB}} \rightarrow nucleus + n$ or $2n$" is the mean free path for a photonuclear reaction where one or two nucleons are chipped off the nucleus. The curve marked "$\gamma + \gamma_{\mathrm{CMB}} \rightarrow e^+e^-$" is the mean free path for the interaction of a high energy photon with the CMB. Added for reference is the mean decay length for a neutron indicated by "$n \rightarrow pe\nu$"

The photo-pion production affects protons with energies above 50 EeV, since in the laboratory reference frame the photon's energy is higher than the threshold $E_\gamma = m_\pi + \frac{m_\pi^2}{2m_p} \simeq 180$ MeV. The pions are producted via the inelastic processes:

$$\begin{aligned} p + \gamma_{\rm CMB} &\rightarrow \Delta^+ \rightarrow n\pi^+ \\ p + \gamma_{\rm CMB} &\rightarrow \Delta^+ \rightarrow p\pi^0 \end{aligned} \tag{2.1}$$

The cross section has a strong resonance above the threshold associated with the single π production while at high energies grows as the $\log s$, where $s = m_p^2 + 2m_p E_\gamma^{\rm CRF}$. The cross section for the multiple photo-pion production has been computed carefully in [51, 52, 53] in order to estimate the fluxes of secondary γ and ν produced in the pion decays. The long tail above the resonance is dominated by the multiple pion production, $N\gamma_{\rm CMB} \rightarrow N(n\pi)$, $n > 1$. A photon with energy ϵ in the Cosmic Rest Frame: the reference frame where the cosmic radiation is isotropic (CRF) corresponds to a threshold for the proton

$$E_{\rm th} = \frac{\left[m_\pi(m_p + {}^{m_\pi}/_2)\right]}{2\epsilon} \simeq 6.8{\cdot}10^{16}\left(\frac{\epsilon}{\rm eV}\right)^{-1}\ {\rm eV}. \tag{2.2}$$

The typical energy for the CMB is $\approx 10^{-3}$ eV from which follows the energy threshold mentioned above. The proton interaction length falls rapidly to $\lesssim 10^2$ Mpc as shown in Fig. 2.2a and 2.2b.

Below the photo-pion threshold energy the dominat mechanism is the e^+e^- pair production, PPP, induced by the interaction with the CMB: $p + \gamma_{\rm CMB} \rightarrow e^+e^-$, down to the threshold

$$E = \frac{\left[m_e(m_p + m_e)\right]}{\epsilon} \simeq 4.8{\cdot}10^{14}\left(\frac{\epsilon}{\rm eV}\right)^{-1}\ {\rm eV} \tag{2.3}$$

which for the CMB energies turns out to be ~ 0.5 EeV. Stecker [54] has utilized data on the energy dependence of the photomeson production cross sections and inelasticities to calculate the mean energy loss time for protons propagating through the CMB in intergalactic space as a function of energy. Based on his results, Stecker then suggested that the particles of energy above the GZK cutoff energy must be coming from within the Local Supercluster of which we are a part and which is centred on the Virgo Cluster of galaxies. Thus, the GZK cutoff is not a true cutoff, but a *feature* [55] as the shape of the energy spectrum around 10^{20} eV depends on many unknowns. The actual position of the GZK cutoff can differ

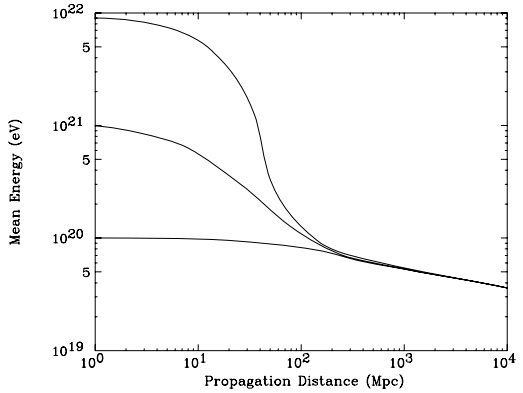

(a) Mean energy of protons as a function of propagation distance through the CMB. Curves are for energy at the source of 10^{22} eV, 10^{21} eV, and 10^{20} eV.

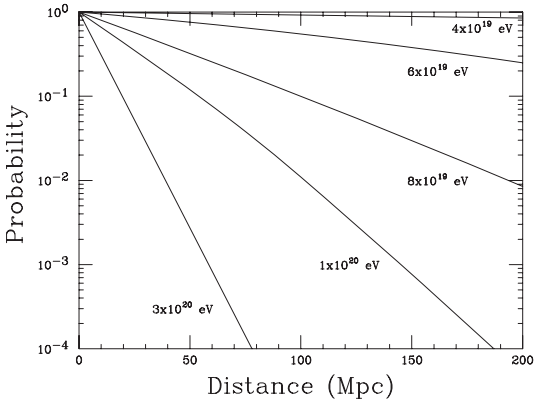

(b) Probability that a cosmic ray proton has travelled further than the indicated distance. Sources are assumed to be distributed uniformly throughout space and emitted with a differential spectral index a = 2.5.

Figure 2.2: Protons propagation features.

from the 50 EeV predicted by Greisen. In fact, there could actually be an enhancement at or near this energy owing to a "pile-up" of cosmic rays starting out at higher energies and crowding up in energy space at or below the predicted cutoff energy [52, 56]. The existence and intensity of this predicted pile-up depends critically on the flatness and extent of the source spectrum, (i.e., the number of cosmic rays starting out at higher energies), but if its existence is confirmed in the future by more sensitive detectors, it would be an evidence for the GZK effect.

For nuclei the situation is slightly different: the dominant loss process above about 10^{19} eV is photodisintegration in the CMB and InfraRed Background Radiation (IRB) due to the giant dipole resonance, followed at lower energy by the pair production. The photo-pion production process is negligible, except for light nuclei at very high energies.

The dominant process for neutrons is the β-decay. The average lifetime in the laboratory reference frame is $\tau_N \simeq 888.65 \pm 3.5$ s which is converted into the propagation distance by

$$R_N = \frac{\tau_N E}{m_N} \simeq 0.9 \left(\frac{E}{10^{20}\ \mathrm{eV}} \right) \mathrm{Mpc} \tag{2.4}$$

2.1.2 Photons

The propagation of photons and electrons is dominated by the interaction with the CMB. The main processes are the pair production $\gamma\gamma_{\rm CMB} \to e^+e^-$ and the Inverse Compton Scattering (ICS) of electrons on the CMB. The energy threshold for the Pair Production (PP) is

$$E = \frac{m_e^2}{\epsilon} \simeq 2.6{\cdot}10^{11}\left(\frac{\epsilon}{\rm eV}\right)\,{\rm eV} \tag{2.5}$$

where ϵ is the $\gamma_{\rm CMB}$ energy and m_e the electron's mass. The ICS has no threshold and the cross section is

$$\sigma_{\rm PP} \simeq 2\sigma_{\rm ICS} \simeq \frac{3}{2}\sigma_T\left(\frac{m_e^2}{s}\right)\ln\left(\frac{s}{2m_e^2}\right) \qquad (s \gg m_e^2) \tag{2.6}$$

where s is the square of the Center of Mass (CM) energy and $\sigma_T = 8\pi\alpha^2/3m_e^2$ is the Thompson cross section (α the fine structure constant). In the Klein-Nishina limt, $s \gg m_e^2$, either the electron or the positron of the pair production carries most of the energy of the incoming γ. This electron can undergo ICS whose inelasticity (relative to the electron) is close to 1 in the Klein-Nishina limit. As a consequence, the upscattered photon which is now the leading particle after this two-step cycle still carries most of the energy of the original γ-ray, and can initiate a fresh cycle of PP and ICS interactions. This leads to the development of an electromagnetic (EM) cascade which plays an important role in the resulting observable γ-ray spectra. EM cascades play an important role particularly in some exotic models of UHECR origin such as collapse or annihilation of topological defects in which the UHECR injection spectrum is predicted to be dominated by γ-rays. But, even if only UHE nucleons and nuclei are produced in the first place, for example via conventional shock acceleration, EM cascades can be produced by the secondaries coming from the decay of pions which are created in interactions of UHE nucleons with the low energy photon background.

2.2 Origin of UHECRs

The models that can be imagined to produce particles with sufficiently high energy to be called UHECR can be broadly divided in two categories: bottom-up and top-down. The first one involves the looking for possible acceleration sites in known astrophysical objects that can reach energies of

the order of 10^{21} eV. The second one involves the decay of very high mass relics from the early universe and physics beyond the standard model of particle physics. In this section we will briefly discuss the general characteristics of these two scenarios with just some hints at specific models.

2.2.1 The 'Bottom-Up' scenario

The apparent lack of a GZK cutoff (with the exception of the new HiRes results) has led theorists to go on a hunt for nearby "zevatrons", i.e., astrophysical sources which can accelerate particles to energies $O(1\ \text{ZeV} = 10^{21}\ \text{eV})$ In most theoretical work in cosmic-ray astrophysics, it is generally assumed that the diffusive shock acceleration process is the most likely mechanism for accelerating particles to high energy (see, e.g., [57] and references therein). A second class of models is based on the direct acceleration mechanisms, where the particles are boosted by extremely strong magnetic fields. The stochastic acceleration mechanism was investigated first by Fermi [58] in 1949.

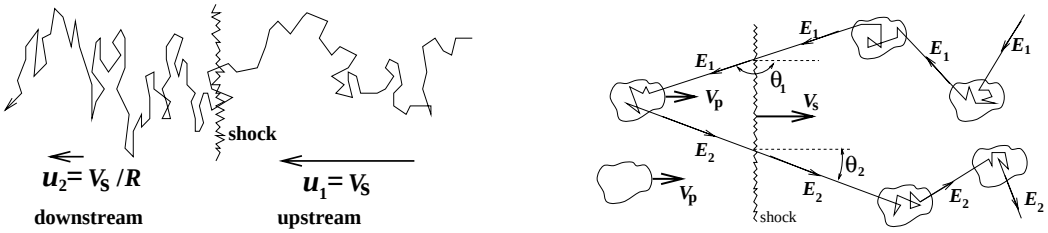

(a) CR-shock front interaction.

(b) The interaction as seen in the shock rest frame.

Figure 2.3: Interacion with an interstellar shock front.

Even if the average electric field vanishes a net transfer of macroscopic kinetic energy from the magnetized moving plasma to the single charged particles in the interstellar medium. The energy transfer is due to a sequence of collisionless scattering with either the magnetic field turbulence or the shocks in the interstellar medium, depending on the model considered. The original Fermi mechanism, which considers the collisions with the magnetic fields, is named 2^{nd} *order Fermi mechanism* because the average energy gain is proportional to $\left(\frac{u}{c}\right)^2$, where u is the relative velocity of the cloud in the CRF and c is the speed of light. Due to the dependence of the gain on the square of the speed of light, the mechanism is not efficient enough to explain the observed spectrum. An extension of the Fermi

acceleration mechanism is obtained considering the multiple scattering of the particle with plain shocks fronts. In this hypothesis the average gain in every interaction with the shock is $\propto \frac{u}{c}$. The Diffusive Shock Acceleration Mechanism (DSAM), the standard model for the CR acceleration, is based on the first order Fermi mechanism.

In this case, the maximum obtainable energy is given by

$$E_{\max} = keZ\left(\frac{u}{c}\right)BL, \tag{2.7}$$

where $u \ll c$ is the shock speed, eZ is the charge of the particle being accelerated, B is the magnetic field strength, L is the size of the accelerating region and the numerical parameter $k = O(1)$ [59]. Taking $k = 1$ and $u = c$, one finds

$$E_{\max} = 0.9Z(BL) \tag{2.8}$$

with E in EeV, B in μG and L in kpc. This assumes that particles can be accelerated efficiently up until the moment when they can no longer be contained by the source, i.e. until their gyroradius becomes larger than the size of the source.

Hillas used this relation to construct a plot of B versus L for various candidate astrophysical objects (Fig. 2.5). Given the relationship between $E_{\max}$ and BL there are not too many astrophysical candidates for zevatrons. Of these, galactic sources such as white dwarfs, neutron stars, pulsars and magnetars can be ruled out because their galactic distribution would lead to anisotropies above 10 EeV which would be similar to those observed at lower energies and this is not the case. Perhaps the most promising potential zevatrons are radio lobes of strong radio galaxies. The trick is that such sources need to be found close enough to avoid the GZK cutoff. Biermann has further suggested that the nearby radio galaxy M87 may be the source of the observed trans-GZK cosmic ray. Such an explanation would require one to invoke magnetic field configurations capable of producing a quasi-isotropic distribution of $> 10^{20}$ eV protons, making this hypothesis questionable. However, if the primary particles are nuclei, it is easier to explain a radio galaxy origin for the two highest energy events;

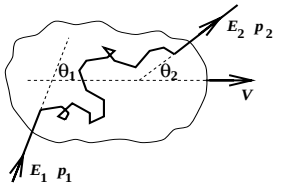

Figure 2.4: Interaction of the cosmic ray with an interstellar cloud.

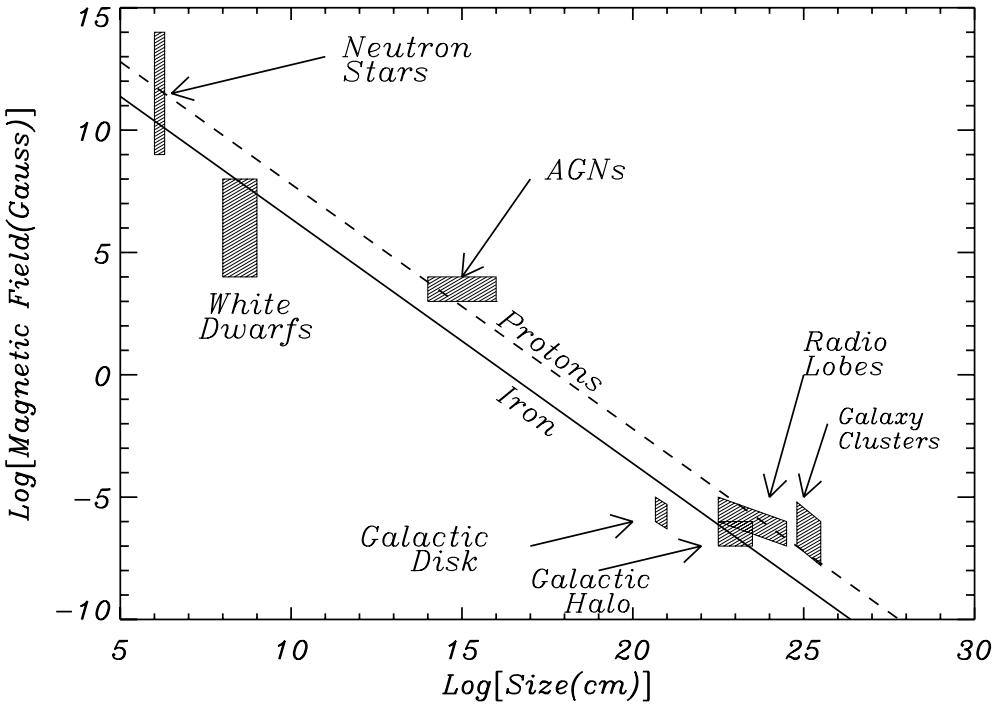

Figure 2.5: A 'Hillas plot' showing potential astrophysical zevatrons [60]. The lines are for B versus L for $E_{\max} = 0.1$ ZeV for protons and iron nuclei as indicated.

2.2.2 Some Classes of Models

As we saw in the previous paragraphs acceleration of UHECRs in astrophysical plasmas occurs when large-scale macroscopic motion, such as shocks and turbulent flows, is transferred to individual particles. The maximum energy of accelerated particles, Emax, can be estimated by requiring that the gyroradius of the particle be contained in the acceleration region. Therefore, for a given strength of the magnetic field, B, and size of the accelerator, L,

$$E_{\max} = ZeBL, \tag{2.9}$$

where Ze is the electric charge of the accelerated particle. The Hillas plot [117] in Fig. 2.5 shows that, for $E_{\max} \gtrsim 10^{20}$ eV and $Z \simeq 1$, the only known astrophysical sources with reasonable BL products are neutron stars, active galactic nuclei (AGN), radio lobes of AGN and clusters of galaxies. In the case of Iron the situation becomes more promising for other sources, like the

galactic halo or extreme white dwarfs. These sources would however have other problems that make them unlikely sources of UHECRs. Indeed the Hillas plot does not include the effect of energy losses in the acceleration sites and these can be quite large because typically in the proximity of the accelerating regions are present strong radiation fields that can cause severe energy losses when the particles leave the acceleration site. In the following we will briefly summarize the situation for the above mentioned models.

Neutron Stars

The possibility that neutron stars may be accelerators of UHECR was discussed in detail in Ref. [61] (and references therein). The main problem encountered in reaching the highest energies is related to the severe energy losses experienced by the particles in the acceleration sites. Most of the mechanisms discussed in literature refer to acceleration processes in the magnetosphere of the neutron star, where curvature radiation limits the maximum energy to a value much smaller than 10^{20} eV. An alternative approach was proposed in [61, 62] where the acceleration process occurs outside the light cylinder of young neutron stars. Rapidly rotating, newly formed neutron stars can induce the acceleration of iron nuclei through MHD winds outside the light cylinder [61]. Although the mechanism through which the rotation energy of the star is converted into kinetic energy of the wind is not yet completely understood, it seems from the observations of the Crab nebula that a relativistic wind does indeed exist, with a Lorentz factor of $\sim 10^7$. Possible nuclei with charge $Z_{26} = Z/26$ can be accelerated in young neutron stars to a maximum energy $Emax = 8{\cdot}10^{20} Z_{26} B_{13} \Omega_{3k}^2$ eV, as estimated in Ref [61]. B13 is the surface magnetic field in units of 10^{13} G and $\Omega_{3k} = \omega/3000 s^{-1}$ is the rotation frequency of the star. Energies gradually smaller are produced while the star is spinning down, so that a spectrum $E \sim E^{-1}$ is produced by a neutron star. The escape process of the accelerated particles becomes effcient about a year after the neutron star birth.

Active Galactic Nuclei

Active galaxies are thought to be powered by the accretion of gas onto supermassive black holes. Acceleration of particles can occur in standing shocks in the infalling gas or by unipolar induction in the rotating magnetized accretion disk [63]. In the former scenario energy losses and size of the acceleration region are likely to limit the maximum energy of the ac-

celerated particles to $\ll 10^{20}$ eV. In the latter case, the main limiting factor in reaching the highest energies is represented by curvature energy losses, that are particularly severe [64] unless moderately high magnetic fields can be kept with a small accretion rate. This may be the case of dormant supermassive black holes, possibly related to the so-called dark massive objects (DMO). Had this model to be right, it would not be surprising that bright counterparts to the UHECR events were not found, since DMOs are in a quiescent stage of their evolution. Very little is known of DMOs as cosmic ray accelerators: the spectrum is not known, and neither is known their spatial distribution. It is therefore hard to say at present whether DMOs can be the sources of UHECRs.

Jets and Lobes

One of the most powerful sites for the acceleration of UHECRs is the termination shock of gigantic lobes in radio galaxies. Of particular interest are a subclass of these objects known as Fanaroff-Riley class II objects (FR-II), that can in principle accelerate protons to $\sim 10^{20} \div 10^{21}$ eV and explain the spectrum of UHECRs up to the GZK cutoff [65]. These objects are on average on cosmological distances. The accidental presence of a nearby source of FR-II type might explain the spectral shape above the GZK energy, but it would not be compatible with the observed anisotropy [66]. Nevertheless, it has been recently proposed that a nearby source in the Virgo cluster (for instance M87) and a suitable configuration of a magnetized wind around our own Galaxy might explain the spectrum and anisotropy at energies above $\simeq 10^{20}$ eV [67] as measured by AGASA. This conclusion depends quite sensibly on the choice of the geometry of the magnetic field in the wind. Several additional tests to confirm or disprove this model need to be carried out.

Clusters of Galaxies

have a sufficiently high BL product to confine particles up to the highest energies, nevertheless they are not suitable to accelerate UHECRs because the propagation of these high energy particles inside the cluster medium causes photo-pion production losses on the CMB photons as in the case of the GZK effect. Losses limits UHECRs in cluster shocks to reach at most $\sim 10^{19}$ eV.

Gamma Ray Burst

GRB are not reported in Fig. 2.5 because they are transient phenomena, but they may accelerate protons to UHE as well [68, 69]. The systems that generate Gamma Ray Burst (GRB) remain unknown, but evidence that GRBs are of cosmological origin and involve a relativistic fireball have become strong with the discovery of X-ray, optical and radio afterglows [70, 71, 72] and the subsequent identification of host galaxies and their redshifts. The UHECR can be accelerated diffusely at the relativistic shock front created by the relativistic fireball. When the GRB explodes in the interstellar medium, with magnetic fields in the μG range, the maximum energy of the accelerated particles is $E_{\max} \simeq 10^{15}\ \mathrm{B}_{\mu}$, where B_{μ} is the magnetic field in mG. On the other hand, if the GRB goes off in the relativistic wind of a neutron star, then the magnetic field is expected to be much larger and the maximum energy can be in the 10^{20} eV range [73]. If UHECRs are accelerated in GRB, observations require the presence of an intergalactic magnetic field in order to dilute the time of arrival of the charged particles generated in the few GRB events occurring within about 100 Mpc. Depending on the power spectrum associated with such field, the upper limits derived from Faraday rotation measurements are in the range $10^{-11} \div 10^{-9}$ G. In a magnetic field of this order of magnitude, the average deflection angle of UHECRs is smaller than the angular resolution of the present experiments ($2^{\circ} \div 3^{\circ}$), therefore clusters of events are expected. If the observed multiplets are in fact the result of bursting sources, the higher energy particles should always reach the detector earlier than the lower energy ones. Although this condition is not satisfied by all the AGASA clustered events, it was proposed [73] that fluctuations may in fact invert the order of arrival of particles with energy.

2.2.3 The 'Top-Down' models

In these particle physics inspired models the problem of reaching the maximum energies is solved by construction. The UHECRs are generated by the decay of very massive particles (generically, X particles), $m_X > 10^{20}$ eV, originating from high-energy processes in the early universe. These X particles typically decay to quarks and leptons. The quarks hadronize producing jets of hadrons containing mainly light mesons (pions) with a small percentage of baryons (mainly nucleons). The pions decay to photons, neutrinos (and anti-neutrinos) and electrons (and positrons). Thus, energetic photons, neutrinos and charged leptons, together with a small fraction of nucleons, are produced directly with energies up to $\sim m_X$ with-

out any acceleration mechanism. The spectra of the particles generated in these decays are typically scatter than the astrophysical ones. In order for the decay products of the X particles to be observed as UHECRs particles today, three basic conditions must be satisfied:

a) the X particles must decay in recent cosmological epoch, or equivalently at non-cosmological distances ($\lesssim 100$ Mpc) from Earth. Otherwise the decay products of the X particles lose all energy interacting with the background radiation, and hence do not survive as UHECR particles;

b) the X particles must be sufficiently massive with mass $m_X \gg 10^{20}$ eV;

c) the number density and rate of decay of the X particles must be large enough to produce a detectable flux of UHECRs.

A powerful tool to constrain top-down models is given by the measurement of the diffuse γ-ray flux [74] because the gamma rays generated at distances larger than the absorption length produce a cascade that transfer most of the energy below ~ 100 GeV. There are basically two ways of generating the very massive particles and make them decay at the present time: 1) trapping them inside topological defects; 2) making them quasi stable (lifetime larger than the present age of the universe) in the early universe.

Topological Defects

Symmetry breaking at particle physics level are responsible for the formation of cosmic topological defects. Topological defects as sources of UHECR were first proposed in the pioneering work of Hill, Schramm and Walker [75]. The general idea is that the stability of the defect can be locally broken by different types of processes (see below): this results in the false vacuum, trapped within the defect, to fall into the true vacuum, so that the gauge bosons of the field trapped in the defect acquire a mass m_X and decay. As said above, at the production the composition of the decay products is dominated by gamma rays and neutrinos, with only about 5% of nucleons. After propagation over cosmological distances, the relative abundance of protons and gamma rays is such that protons dominate up to energies in excess of 10^{20} eV, while at even higher energies, the composition expected to be dominated by γ-rays.

Several topological defects have been studied in the literature: ordinary strings, superconducting strings, bound states of magnetic monopoles, networks of monopoles and strings, necklaces and vortons.

Cosmological Relic Particles

Supermassive particles can also be produced in the early universe independently of topological defects, either through gravitational production [76] or through direct coupling to the inflaton field. Relic particles produced gravitationally have mass $m_X \leq H(t) \leq m_\varphi$, where $H(t)$ is the Hubble constant and m_φ is the inflaton mass; if their decay time is sufficiently long, they can be natural candidates for cold dark matter [77, 78]. The long decay times may be the result of some weakly broken discrete symmetry (such as R-parity for the case of neutralinos). Supermassive relics accumulate in dark matter halos, and in particular in the halo of the Milky Way. Their rare decays may be sufficient to account for the observed fluxes of UHECRs above 10^{20} eV[79]. The strongest signature of the model is the anisotropy due to the asymmetric position of the sun in the Galaxy. Current observations are not yet stringent enough to rule against or in favor of the model.

Part II

Observation from Space

Chapter 3

The Space approach

Since the late '50, the quest for the most energetic particles in the Universe has driven the construction of experiments to monitor larger and larger portions of atmosphere. The largest ground experiment for the detection of UHECR, the PAO, is currently under construction in the *Pampa Amarilla*: it will be equipped with 1600 ground detectors and 4 fluorescence eyes and its extension will be ~ 3000 km^2. A second giant observatory in the norther hemisphere, with an overall active surface of ~ 6000 km^2, is currently under study. The aim of PAO is to measure with great accuracy the spectrum of cosmic rays in the GZK energy region, to investigate the GZK feature and to identify possible sources of UHECRs. At energies above the GZK feature the flux of primaries is so low that the trans-GZK statistic will be poor even with the huge PAO arrays.

Next generation UHECR experiments, aiming to shed new light on UHECR astronomy, will have to find out new techniques to further increase the detector's sensitive area: the construction of bigger arrays is in fact unlikely due to practical and financial constraints.

One of the most promising techniques is the observation from space of the fluorescence signal generated by the EAS crossing the atmosphere. In this Chapter we will introduce the space approach and we will discuss the basic requirements an UHECR detector must fulfill from the observational and instrumental point of view. We will outline the most important aspects of the detector design and investigate how they can be estimated from the scientific and observational requirements. The number of parameters to optimize is large and large is the number of constraints to satisfy.

Analytical and semi-analytical relations will be used in order to set the scenario for space-based observation, to show the limits and the possi-

bilities of this technique. These results cannot replace a full Monte-Carlo simulation for precise studies. However they are useful for the basic understanding, for a fast study and for the full simulation results.

3.1 Key points of the observational approach

An EAS can be detected from space by observing the air scintillation light, isotropically produced during the EAS development, and proportional, at any point along the EAS development, to the number of charged particles in the EAS. The additional observation of the diffusely reflected Cherenkov light (reflected either by land, sea or clouds) provides additional information. Therefore it is possible to estimate the energy and arrival direction of the primary UHECR, and to gather information about its nature. The atmosphere is thus used as a calorimeter. Any given EAS will be seen as a point moving with a direction and angular velocity depending on the EAS direction. The peculiar characteristics of the EAS, including the kinematical ones, allow one to distinguish them from the various backgrounds, because those have a typically different space-time development. Key points of the observational technique are the following.

- A large geometrical aperture can be obtained, thanks to the large distance, depending on the Instrument FOV. A large mass of atmosphere (the calorimeter medium) can therefore be observed.
- Detection of EAS produced by weakly interacting primary particles, starting to shower deeply in the atmosphere, is possible, by the direct observation of the EAS development and starting point.
- All sky coverage is possible with one single apparatus.
- The line of sight from the EAS to the detector is aligned with the atmospheric density gradient. This is twice an advantage: the amount of material traversed by the fluorescence light, and therefore its attenuation, is minimized. Moreover, being the EAS is observed from above, most of the light doesn't experience the Mie scattering on the Aerosol particles, mainly present in the boundary layer (h = 2500 m a.s.l).
- The approach is complementary to the ground-based one. In fact the space experiments are best suited for the observation of higher energy cosmic rays with respect to ground-based experiments. However an overlap of the observed energy spectrum with the one known

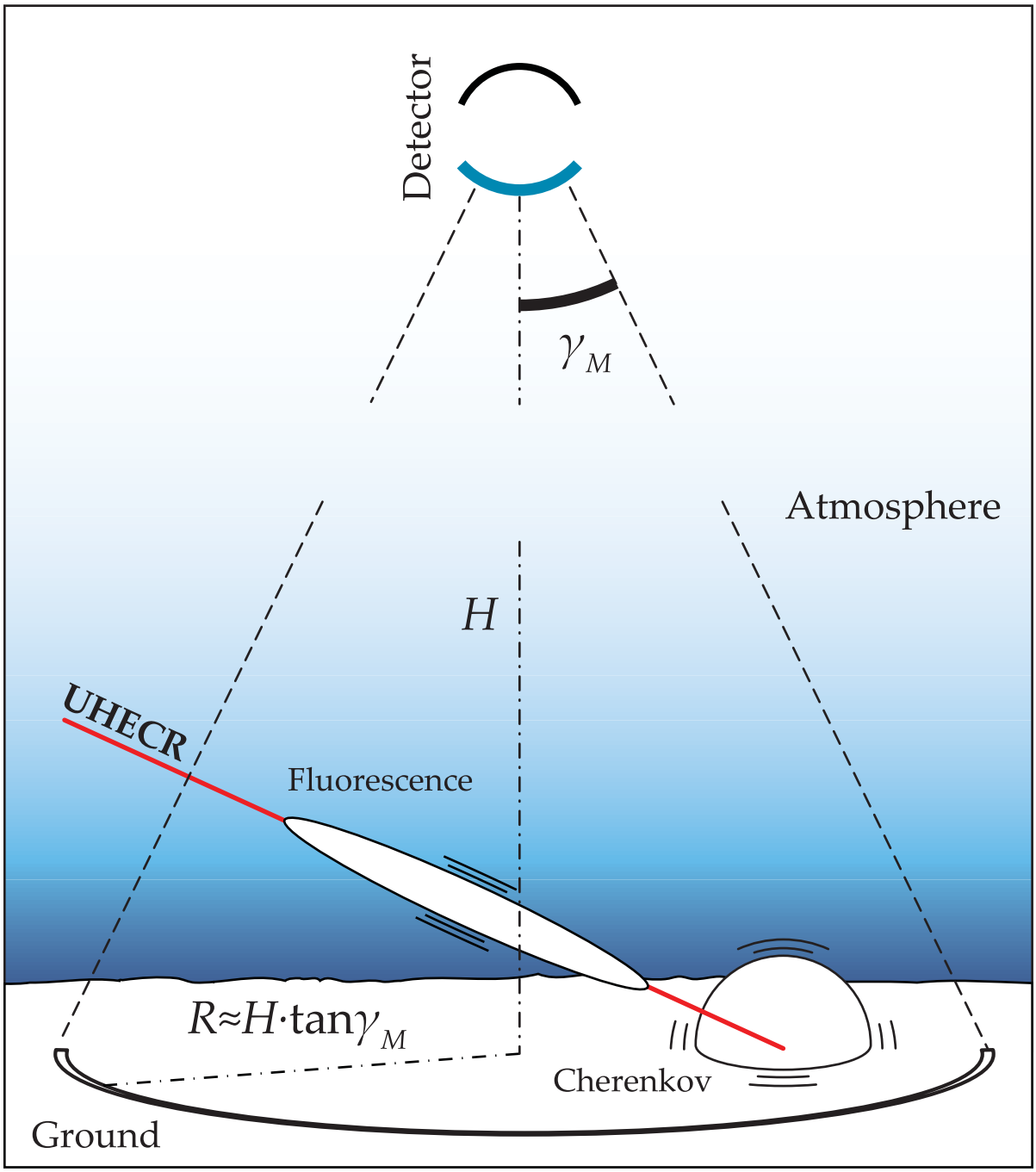

Figure 3.1: The approach from space. $\gamma_{\max}$ is the half FOV angle, H the detector's altitude and R the radius of the monitored Earth's surface.

from ground-based experiments is required for a better comparison. A larger geometrical aperture is obtained from space experiments with respect to ground-based experiments. The systematic effects are different in the two approaches.

The scintillation light, mainly emitted in the $330 \div 400$ nm wavelength range, is isotropic and proportional, at any point, to the number of charged particles in the EAS, largely dominated by electrons and positrons. The total amount of light produced is proportional to the primary particle energy and the shape of the EAS profile (in particular the atmospheric depth of the EAS maximum) contains information about the primary particle identity. In this wavelength range the atmosphere is relatively transparent, down to $\lambda \approx 330$ nm where the ozone absorption becomes strong.

The possible observation of the Cherenkov light diffusely reflected by the Earth (by land, sea or clouds) will help the determination of the EAS parameters. While the amount of observed Cherenkov photons depends on the reflectance and geometry of the impact surface, the directionality of the Cherenkov beam provides a precise extrapolation of the EAS direction to the first reflecting surface.

Many different kind of backgrounds are expected including: the night-glow, man-made lights, auroras, natural photo-chemical effects (in atmosphere, sea and land), low-energy cosmic rays, reflected moonlight and star-light. However the typical characteristics of EAS are quite different from the background ones, in particular the kinematic characteristics. The backgrounds, for instance, typically have a time-scale of the order of ms.

3.1.1 Definition of the basic quantities for an EAS detector

Before moving on with the discussion of the space observation is useful to define the basic quantites commonly used to characterise the performances of UHECR experiments. The ingredients are the active surface of the experiment S, the observed solid angle Ω , the Energy threshold $E_{\rm th}$, the local EAS zenith angle θ, the differential primary flux $J(E) = \frac{\mathrm{d}N}{\mathrm{d}E\mathrm{d}S\mathrm{d}\Omega\mathrm{d}t}$ [1], the duty cycle η and $\epsilon(\vec{x},\theta,E,\ldots)$, the overall detection efficiency, which includes all the possible causes of a lack of detection. ϵ depends maily on the EAS position $\vec{x}$, on θ and on E.

The CR differential flux is a power law [21]

$$J(E) = \frac{\mathrm{d}\Phi}{\mathrm{d}E\,\mathrm{d}\Omega} \simeq A\left(\frac{E}{\mathrm{GeV}}\right)^{-\alpha} \frac{\text{particles}}{\mathrm{km}^2\cdot\mathrm{sr}\cdot\mathrm{yr}\cdot\mathrm{GeV}} \tag{3.1}$$

[1] $[J] = [\mathrm{km}^{-2}\cdot\mathrm{sr}^{-1}\cdot\mathrm{yr}^{-1}\cdot\mathrm{eV}^{-1}]$

with $A \approx 5.6 \cdot 10^{17}$ and $\alpha \simeq 2.7$ above the ankle ($\sim 5 \cdot 10^{18}$ eV). Above $5 \cdot 10^{19}$ eV, where the GZK effect starts to affect the spectrum, the flux is extremely low, only few particles per km^2·sr·yr.

The expected event rate in nominal data taking conditions is:

$$\frac{\mathrm{d}N}{\mathrm{d}t} = \int_S \int_\Omega \int_{E_{\mathrm{th}}}^{\infty} \mathrm{d}S \, \mathrm{d}\Omega \, \mathrm{d}E \, \epsilon(\vec{x}, \theta, E) \cos\theta J(E), \tag{3.2}$$

where E_{th} is the energy threshold, defined as the energy where the efficiency flattens and the systematics can be kept under control. If required by a poor efficiency other particular circumstances, similar cuts could be applied to θ and x as well.

We define the geometrical aperture of the experiment as $\mathcal{A} = \int_S \int_\Omega \mathrm{d}S \, \mathrm{d}\Omega \cos\theta$. For a fluorescence detector the detection efficiency ϵ increases with energy until a certain point, after which $\frac{\partial \epsilon}{\partial E}$ becomes approximately constant. The reason of the increase is that the number of photons is proportional to the primary's energy: this ceases to be relevant when the intensity of the signal is high enough to clearly stand over the background and a further increase doesn't improve the detection efficiency any more. The equation (3.2) can be written as

$$\frac{\mathrm{d}N}{\mathrm{d}t} = \mathcal{A}_{\mathrm{eff}} \int_{E_{\mathrm{th}}}^{\infty} \mathrm{d}E \, J(E) \tag{3.3}$$

where

$$\mathcal{A}_{\mathrm{eff}} = \int_S \int_\Omega \mathrm{d}S \, \mathrm{d}\Omega \, \epsilon(\vec{x}, \theta) \cos\theta \tag{3.4}$$

is the effective aperture of the detector.

Assuming that the performance does not change sensibly with time, the total number of detected events during the experiment's lifetime ΔT is

$$N = \int_{\Delta T} \mathrm{d}t \, \eta \mathcal{A}_{\mathrm{eff}} \int_{E_{\mathrm{th}}}^{\infty} \mathrm{d}E \, J(E) = \Sigma \int_{E_{\mathrm{th}}}^{\infty} \mathrm{d}E \, J(E). \tag{3.5}$$

where $\Sigma = \eta \mathcal{A}_{\mathrm{eff}} \Delta T$ is the exposure of the experiment.

3.2 Guidelines for the design of the detector

The detector for the measurement of the light signal of giant EAS in the atmosphere shall be designed as a large field of view, large optics, fast, near-UV digital camera. The requirements on the instrument follow from the scientific requirements which are summarized below:

- All sky coverage. The distribution of graviting matter within the surrounding of the Earth is not uniform as shown in Fig. 3.2. Since the uncertainties of the UHECR production models are large, there is no region of the sky that can be excluded *a priori* in the search for source candidates. The monitoring of the full sky increases the chance of overlapping with ground based observatories and telescopes that may support source identification can be complemented with observations in the optical, radio and gamma wavelength ranges.

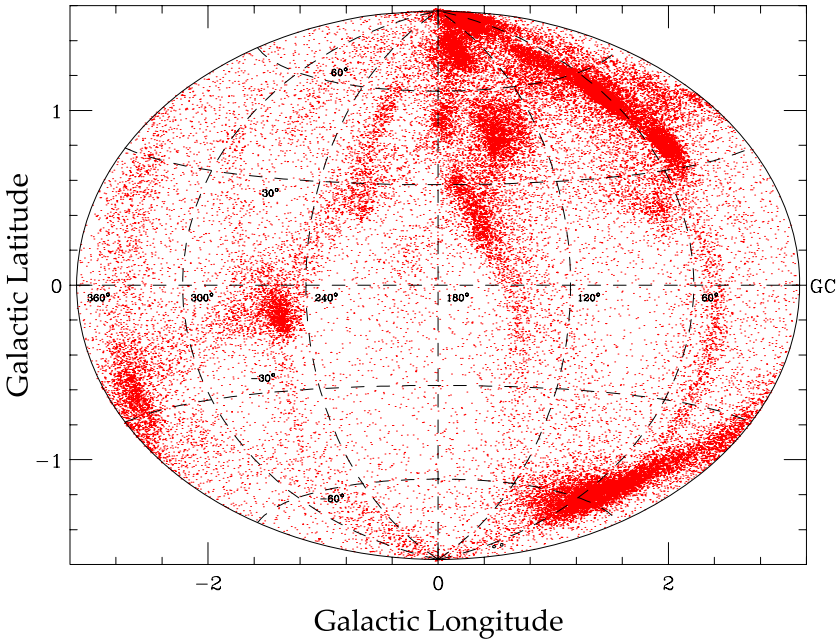

Figure 3.2: Distribution in galactic coordinates of gravitating matter at distance between 7 and 21 Mpc from [80].

- Angular resolution on the primary particle direction: $\lesssim 1^\circ$ for a large enough subsample of events. Due to the limitation on the source distance by the GZK effect and the high rigidity, UHECRs may be traced back to their sources above GZK energy. However the galactic

magnetic field and the less-known extragalactic magnetic fields may deflect the primary particle by few degrees. On average the angular resolution of 1° will be sufficient for point sources identification.

- Energy resolution: $\Delta E/E \lesssim 0.3$;
- Energy threshold: $E_{\rm th} \approx 10^{19}$ eV . Even if the energy region where the effectiveness of an UHECR space experiment is higher is above 10^{20} eV, a subsample of showers of $E > 10^{19}$ eV must be detected and reconstructed at full efficiency to provide a precise measurement of the spectrum in the region observed by ground experiments. The overlap has several advantages as the possibility to calibrate the absolute reconstructed energy of the showers using the features of the UHECR spectum itself. To achieve a good precision a flat efficiency plateau is required on a sufficiently large sample of events in well defined conditions at $E > E_{\rm th}$, to keep systematics under control.
- $X_{\rm max}$ resolution $\Delta X_{\rm max} \leq 35$ g/cm^2, which is half of the mean $X_{\rm max}$ difference between proton and iron induced EAS ≈ 70 g/cm^2. Such resolution will allow a separation of the iron/proton primaries on a statistical basis.

A space instrument has to fulfill a certain number of constraints and features which do not have a counterpart in ground experiments. The design shall be a balance between a large optics aperture to collect as much light as possible and the high compactness to match the requirements of a space mission. The instrument's is made of three main subsystems: the Optical Module, the Photo Detector and the electronics.

The two basic requiements can be expanded as follows:

- The instrument must collect as many photons as possible, in order to be able to detect the faint signal from the less energetic EAS and to discriminate it from the background. As a consequence a large aperture is required, as well as a good transmission of the optical elements and good photon detection efficiency in the $330 \div 400$ nm wavelength range.
- A large FOV is required to be able to observe a mass of atmosphere as large as possible, thus increasing the expected event rates.
- The physics requirements can be satisfied with a system having an angular granularity sufficient to ensure an angular resolution on the EAS direction of $\approx 1°$.

- A fast enough photo-detector to be able to follow the space-time development of the EAS (sampling time below $\sim 0.1\ \mu$s) and reconstruct the EAS kinematical parameters from one single observation point.
- A low noise and good signal to noise ratio are required to detect the faint signal produced by the less energetic EAS and discriminate it from the background. Small cross-talk and after-pulse rate are required to avoid degradation of the energy and angular resolution.
- An efficient and reliable trigger system, capable of a good background rejection, is required to cope with the limited data storage, data transfer and computing capabilities available on-board.
- All the constraints and requirements related to the space mission have to be accounted for. Mandatory characteristics are therefore: a compact and robust system with low mass, volume and power consumption, good reliability and time stability, radiation hardness and low sensitivity to magnetic fields.
- A system is required to protect the Instrument from possibly dangerous environmental factors, including intense light.

3.2.1 General assumptions

The EAS properties depend on the primary particle identity, energy (E), direction $\hat{v}$ (zenith angle θ, azimuth φ) while features of the signal detected on the instrument's focal surface basically depends on EAS location inside the instrument's FOV, defined by the off-axis angle γ, and on the angle ζ between the line of sight $\hat{o}$ and the shower direction. Since ζ is not independent of θ, φ and γ we introduce also ψ_{az} defined as in Fig. 3.3.

The general assumptions are:

1. Hadron-induced EAS, with $E = (0.1 \div 10) \cdot 10^{19}$ eV , observed in clear sky conditions. For several reasons, which will be discussed in the rest of the paper, we only consider EAS with a zenith angle $30° \lesssim \theta \lesssim 75°$.
2. Exponential density profile of the Earth's atmosphere as a function of the height, h, above the sea level:

$$\rho(h) = \rho_0 \exp\left(-\frac{h}{h_0}\right) \quad \text{with} \quad \rho_0 = 1.24\ \text{kg/m}^3 \quad \text{and} \quad h_0 = 8.3\ \text{km} \quad . \tag{3.6}$$

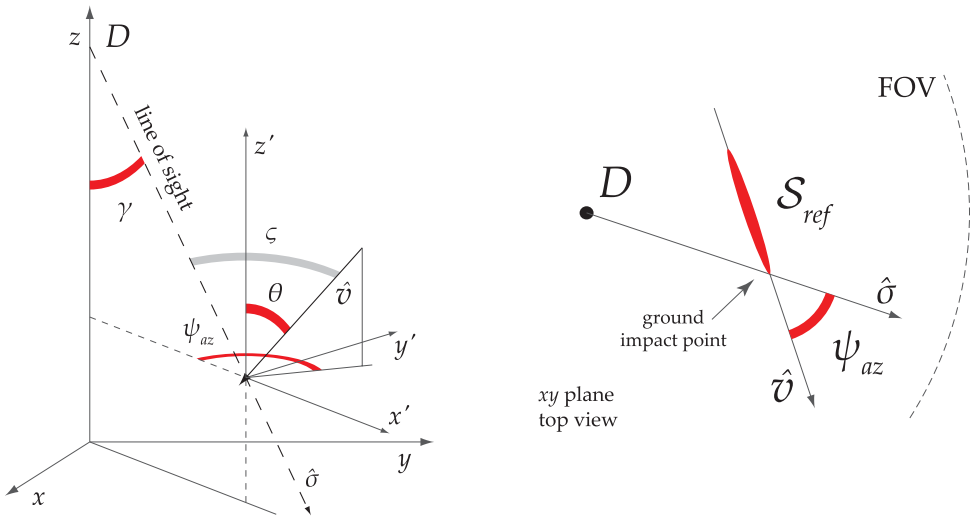

Figure 3.3: Definiton of ψ_{az}.

In some calculations we have also used the Linsley's parametrization of the US Standard Atmosphere as a cross-check [81].

3. Gaisser-Hillas parametrization [82] for the EAS longitudinal profile:

$$N(X) = N_{\max}\left(\frac{X - X_0}{X_{\max} - X_0}\right)^{\frac{X_{\max}-X_0}{\lambda}} \exp\left(\frac{X_{\max} - X}{\lambda}\right) \quad , \qquad (3.7)$$

where $N(X)$ is the number of charged particles, X_0 is the first interaction point of the particle[2], $X_{\max}$ is the depth of the EAS maximum, $\lambda = 65\,\mathrm{g/cm^2}$ [83] the EAS attenuation length[3] and $N_{\max}$ is the number of charged particles at the shower maximum. Moreover $N_{\max} = \alpha E$ with $\alpha \simeq 0.6/\mathrm{GeV}$ [84]. Typical values are given in the Table 3.1[4].

The height h_{M} of the EAS maximum vs the zenith angle θ is shown in

[2] X_0 is frequently assumed as the depth of the first interaction. In our calculations, as discussed by [83], X_0 can be fixed at the first interaction point.

[3] λ is rather energy independent and very similar for proton and iron in the energy range between 10^{19} eV and 10^{21} eV.

[4] The values of $X_{\max}$ are the mean of the values for different interaction models (MOCCA-Internal, MOCCA-SIBYLL, CORSIKA-SYBILL and CORSIKA-QGSjet). Note that these values are influenced by X_0 using the parametrization (3.7). See [83] for more details.

Particle	**Energy** [eV]	$\mathbf{X_0}$ [g/cm^2]	$\mathbf{X_M}$ [g/cm^2]
Proton	$1.0{\cdot}10^{19}$	35	824 ± 55
Proton	$5.0{\cdot}10^{19}$	35	853 ± 58
Proton	$1.0{\cdot}10^{20}$	35	880 ± 54
Proton	$5.0{\cdot}10^{20}$	35	907 ± 49
Iron	$1.0{\cdot}10^{19}$	10	724 ± 20
Iron	$5.0{\cdot}10^{19}$	10	754 ± 20
Iron	$1.0{\cdot}10^{20}$	10	784 ± 19
Iron	$5.0{\cdot}10^{20}$	10	814 ± 19

Table 3.1: Typical values of EAS parameters from [83]

.

Fig. 3.4 for three different values of the slant depth $X_{\max}$ of the EAS maximum.

4. Flat Earth approximation: this assumption does not substantially affect the results for EAS zenith angle $\theta \lesssim 70°$; in fact, for $\theta = 70°$ the difference between the exact and the approximated value of the slant depth at ground is only ~ 30 g/cm^2, as shown in Fig. 3.5. The following relation will be, therefore, assumed:

$$\frac{\mathrm{d}\ell}{\mathrm{d}h} = \frac{1}{\cos\theta} \quad , \tag{3.8}$$

between the quota above the Earth surface, h, and the distance ℓ measured along a straight line with zenith angle θ.[5]

5. A typical hadron-induced EAS of $E = (0.1 \div 10){\cdot}10^{19}$ eV with $\theta \lesssim 75°$ is seen on the focal surface of an orbiting instrument as a track not longer than a few degrees, as discussed in detail in Sec. 3.2.3. We can therefore neglect any possible change of the instrument properties with the field angle for any given EAS. Obviously this is not true any more for very inclined tracks which can be many degrees long.

6. The EAS develops in the atmosphere at an height $h \lesssim 20$ km. In this region the scintillation yield in the wavelength range WR = 330 nm $\leq \lambda \leq$ 400 nm can be considered nearly constant [85]: $Y \simeq 4.5$ ph·particle^{-1}·m^{-1}.

[5]The true relation is $\frac{\mathrm{d}\ell}{\mathrm{d}h} = (\cos\theta + \frac{\ell}{R_\oplus}\sin^2\theta)^{-1}$, where $R_\oplus$ is the Earth's radius; (3.8) is the limit for $R_\oplus \to \infty$. It is worth remembering the exact relation $\frac{\mathrm{d}X}{\mathrm{d}\ell} = \rho(h(l))$.

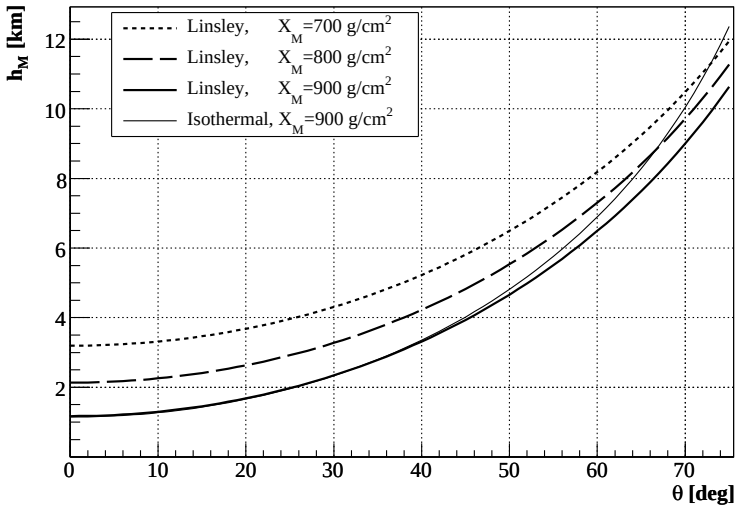

Figure 3.4: Height h_{M} of the EAS maximum vs the zenith for three values of X_{max}. Linsley's parametrization of atmospheric density profile is used. The exponential profile for $X_{\mathrm{max}} = 900$ g/cm^2 is shown for comparison.

7. The random background is assumed to be uniform and constant on the space and time scales of the EAS development. It is assumed that by suitably measuring the background nearby the EAS, both in space and in time, the underlying random background can be subtracted when the EAS is detected. This is justified by the rather large expected background rate, such that the relative error on the background estimate is small (see Sec. 3.2.12).

8. As far as the atmospheric transmission is concerned, we have taken in account only the Rayleigh scattering; in fact the Mie scattering is important below ~ 2 km of altitude, while the EAS develops generally above this height (see the fig. 3.4).

9. The instrument orbital height, H, is assumed to be: 300 km $\lesssim H \lesssim$ 1000 km. A reference altitude of $H \simeq 400$ km will be used.

Note that some of the above assumptions are optimistic with respect to the real conditions of the experiment. This means that the results we will obtain are necessary, but possibly not sufficient, requirements for observations.

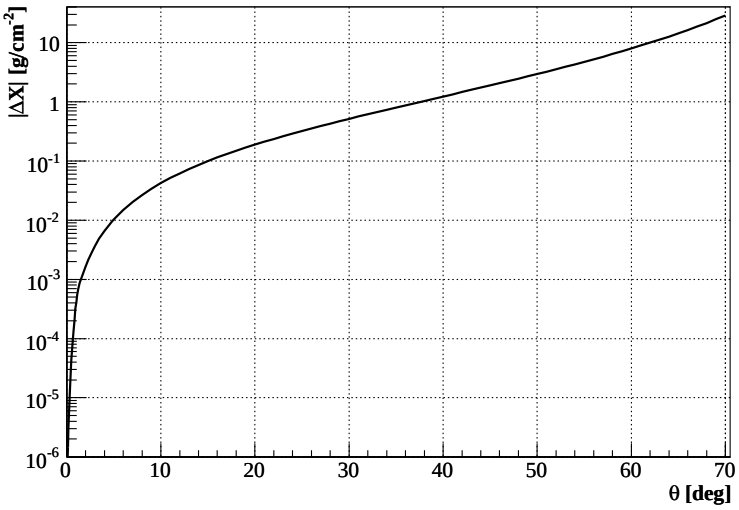

Figure 3.5: Absolute value of the difference $|\Delta X|$ between the true slant depth at ground and the one in flat Earth approximation versus the zenith angle.

3.2.2 The shower template $\mathcal{S}_{ref}$

In deriving the basic relations we apply some simplifications, using analytical calculations whenever possible. We define a simple frame by means of a template shower $\mathcal{S}_{ref}$ and a simple detector-shower configuration. The scenario is defined by 5 parameters: E, $\hat{v}$, ψ_{az}, H and γ summarized in Tab. 3.2. From this configuration and scientific requirements we will calculate requirements on the instrument.

Energy : E_{ref} is fixed by the scientific requirements to have a good superposition with the spectrum of running experiments. $E_{\text{ref}} = 10^{19}$ eV

Direction : the kinematic of the EAS signal at the pupil strongly depends on the zenith angle θ and on ψ_{az}. $\theta = 45°$ grants a good extension of the shower with a negligible shortening of the longitudinal profile due to the impact with the ground while $\psi_{az} = 90°$ is motivated by the request to have an average behavior of the signal (see Sec. 3.2.3).

Altitude : at the lowest energies, close to the required threshold E_{ref}, the flux of primaries is relatively high while the number of expected photons per shower is rather poor. According to the aim to work out a set of requirements, we choose the most favorable height for the photon's statistics, $H = 400$ km.

Off-axis angle : The detection efficiency depends strongly on the number of detected photons, particularly at low energies. In the current simplified scenario, the shower's irradiance M, number of photons per second per m^2, depends only on the position in the FOV γ, H and on the atmosphere transmission coefficient K_{atm}

$$M \propto K_{\text{atm}} \left(\frac{\cos \gamma}{H} \right)^2 . \tag{3.9}$$

The irradiance decreases as the EAS approaches to the border of the FOV (see Fig. 3.6). Since $\mathcal{S}_{ref}$ is at the energy threshold the consequence of this dependence is that a detector tuned to detect $\mathcal{S}_{ref}$ in γ with the required efficiency will collect more photons from any shower like $\mathcal{S}_{ref}$ in $\gamma' < \gamma$, but will collect less light if $\gamma' > \gamma$. As the primary energy increases, M increases proportionally and the shower is detected everwhere in the FOV. Close to the threshold, where the signal is weaker, the flux of UHECR is quite high compared to the acceptance of a space detector. Actually a low efficiency at the border of the FOV is not critical because the statistic in the central region is sufficient for a good measurement of the spectrum. A reasonable requirement, taking into account the request for compactness of space instruments, is to have full efficiency in at least half of the FOV, which corresponds to $\gamma = 20°$.

Energy	$E = 10^{19}$ eV
Zenith angle	$\theta = 45°$
Shower/line of sight angle	$\psi_{az} = 90°$
Angular extension in the FOV	$\xi_{\text{EAS}} \simeq 1.4°$
Duration of the EAS development	$T_{\text{EAS}} \simeq 76\ \mu$s
Detector's altitude	$H = 400$ km
FOV location	$\gamma = 20°$

Table 3.2: Features of the standard proton EAS $\mathcal{S}_{ref}$ used as model.

3.2.3 The length of the visible EAS track

The angle subtended by the visible EAS track on the focal surface of the instrument is easily estimated computing the EAS length between the first and last EAS point detected by the instrument.

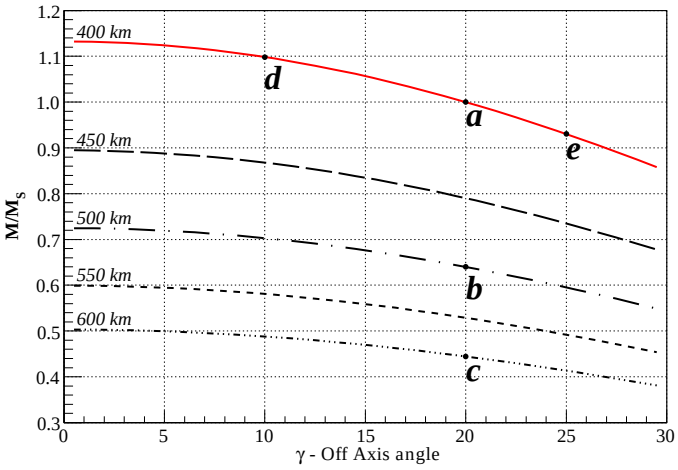

	H [km]	γ [°]	M/M_0
a	400	20	1.00
b	500	20	0.65
c	600	20	0.44
d	400	10	1.1
e	400	25	0.93

Figure 3.6: Functional dependence of the M/M_0 irradiance at the detector as a function of γ and H compared to the reference value for $\gamma_0 = 20°$ and $H_0 = 400$ km.

In the hypothesis of being able to subtract all the background, the shape of the signals is described by the Gaisser-Hillas function (3.7), which is a Gamma distribution

$$g(X) = \frac{1}{\Gamma(\alpha)} \Lambda^{-\alpha} X^{\alpha-1} \exp\left(-\frac{X}{\Lambda}\right) \tag{3.10}$$

where the parameters are $\alpha = (X_{\max} - X_0)/\lambda + 1$ and $\Lambda = \lambda$. The mean and the standard deviation of this Gamma distribution are therefore

$$\langle X \rangle = \alpha\Lambda = X_{\max} - X_0 + \lambda$$
$$\sigma_X = \Lambda\sqrt{\alpha} = \sqrt{\lambda(X_{\max} - X_0 + \lambda)}$$

For the sample shower of table 3.2, whose energy is $E = 10^{19}$ eV, we need $N = 100$ photons[6] in this case the minimum and maximum value and the range of X in the distribution are

$$\min(X) \approx \langle X \rangle - 2\sigma_X$$
$$\max(X) \approx \langle X \rangle + 3\sigma_X$$
$$\text{range}(X) \approx 5\sigma_X$$

[6] As it will be explained in section 3.2.7, this is the minimum number of photons required to achieve the required 30% energy resolution.

Using the values listed in Sec. 3.2.1, we obtain $\max(X) \approx 1561$ g/cm^2 and $\min(X) \approx 383$ g/cm^2, the corresponding positions in the Earth's atmosphere and the shower length. At this point it is trivial to estimate the angle ξ_{EAS} subtended by the EAS and the EAS duration T_{EAS} on the focal surface. Their dependence on the zenith angle θ are shown respectively in Fig. 3.7 and Fig. 3.8 for $\mathcal{S}_{ref}$, $\gamma = 20°$, $H = 400$ km for three values of the azimuth angle ψ_{az}.

The dependence of ξ_{EAS} and T_{EAS} from ζ for $\mathcal{S}_{ref}$ are shown respectively in Fig. 3.9.

As it is clear from the Fig. 3.7, $\xi_{\mathrm{EAS}} < 4°$, justifying the assumptions of the Sec. 3.2.1. Note also, from the figures 3.7 and 3.8, that for $\theta \lesssim 50°$ the EAS are truncated by ground, as is evident from the cusp in the figures.

Some values for $\mathcal{S}_{ref}$ are given in Table 3.3.

	EAS		**EAS Core**	
Total length in air	13.8 km		7.6 km	
Total duration in air	45.9 μs		25.3 μs	
Total flux F	58 ph/m^2		45 ph/m^2	
ψ_{az} [°]	ω_{EAS} [rad/s]	ξ_{EAS} [°]	T_{EAS} [μs]	ξ_{core} [°]	T_{core} [μs]
0	458	1.70	65	0.94	36
90	325	1.41	76	0.78	42
180	161	0.89	88	0.44	48

Table 3.3: Kinematic parameters of $\mathcal{S}_{ref}$ (at $\gamma = 20°$, $H = 400$ km). The EAS Core is defined as the portion of the fluorescence profile around the maximum whose intenisity is at least half of the maximum.

3.2.4 Orbit

The orbit parameters can be tuned to optimize the expected results. The orbital height is one of the most important parameters to tune the energy range and the effective aperture.

In fact an higher altitude implies a larger mass of observed atmosphere but also an higher energy threshold because of the smaller signal; so the choice of the right orbit's shape depends on the energy threshold, taking in account the fact that at higher energies the flux is lower and there is need of a bigger target mass. Varying the orbital height is useful in order to span a larger range of energies: with an elliptic orbit the satellite spends more time at a higher altitude, gaining in effective aperture, but it also spends

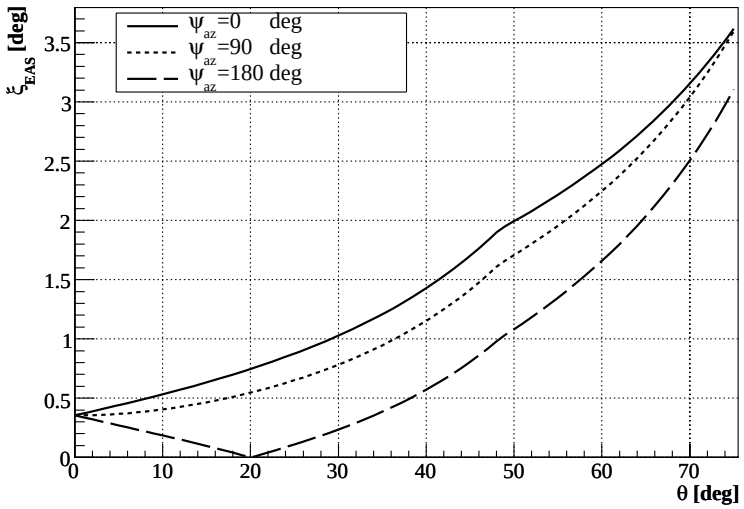

Figure 3.7: Average angle ξ_{EAS} subtended by $\mathcal{S}_{ref}$ on the detector's focal surface as a function of the zenith angle θ for three values of ψ_{az} (at H = 400 km, $\gamma = 20°$).

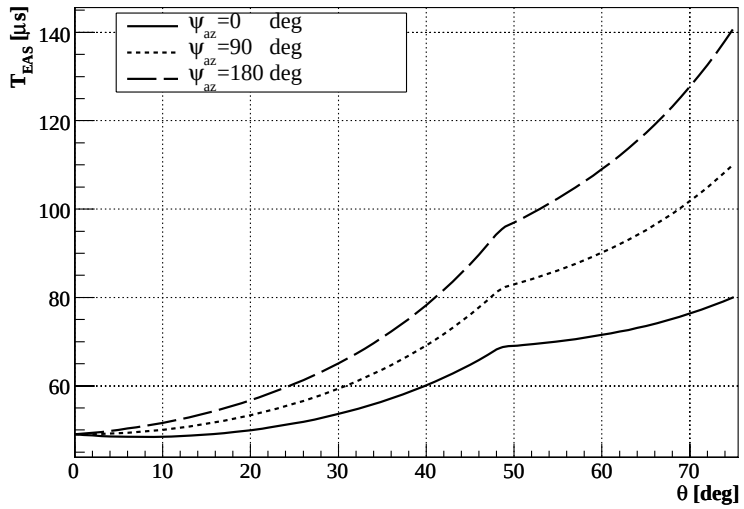

Figure 3.8: Average duration T_{EAS} of the development of $\mathcal{S}_{ref}$ on the detector's focal surface as a function of the zenith angle θ for three values of ψ_{az} (at H = 400 km, $\gamma = 20°$).

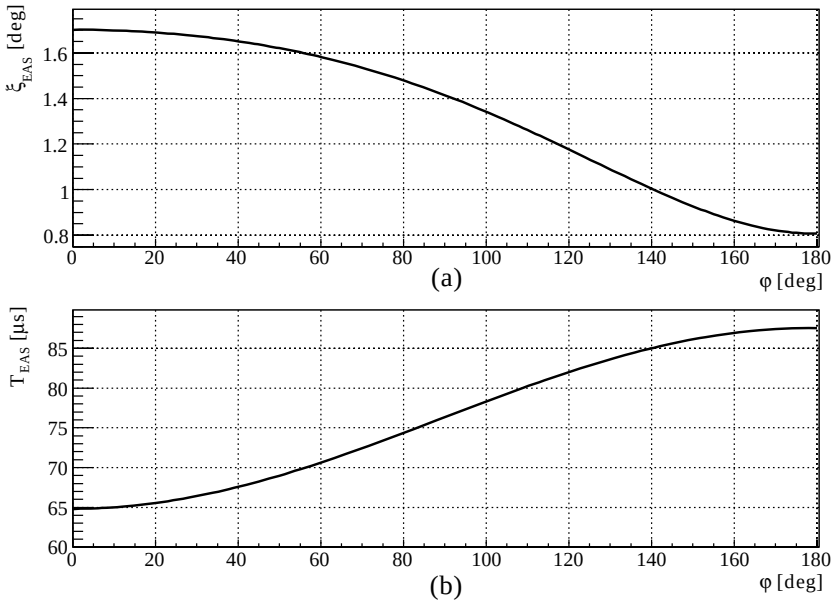

Figure 3.9: Average angular extension ξ_{EAS} (a) and time length T_{EAS} (b) of the $\mathcal{S}_{ref}$ development on the detector's focal surface as a function of the azimuth angle ψ_{az} (at $H = 400$ km, $\gamma = 20°$).

time at a lower altitude, decreasing the energy threshold, where a long measuring time might be not necessary.

Another way to vary the height might be to use different circular orbits during the mission lifetime (for example part of the time at a lower altitude and part of the time at an higher altitude). One should remember that the orbit lifetime depends on the height and it strongly depends on the epoch of the Solar cycle, which affects the atmospheric density. The orbit's inclination should be chosen in order to span as much as possible the Earth's surface (and atmosphere) and to obtain a full sky coverage. An important parameter that depends on the orbit is the duty cycle, that should be as large as possible. For this purpose, the orbit's design must be further optimized in order to avoid as much as possible the light pollution from the man-made sources at ground and from the lightings (that are concentrated mainly on the land) and the auroras. Note also that the duty cycle (the exposure) can be recovered increasing the mission lifetime. The orbit's design can be also optimized in order to access as much time as possible over fixed targets at ground (ground EAS experiments, weather stations, etc.). In particular, the accesses to other EAS experiments, as the

Pierre Auger Observatory, are very useful for the instrument calibration.

3.2.5 The detector

Within the cargo and orbits constraints, the number of detected photons is the main indicator of the efficiency of the detector.

We define the Photo-Detection Efficacy $\mathcal{E}_{\mathrm{PD}}$ as

$$\mathcal{E}_{\mathrm{PD}}(\gamma) = \frac{n_{\mathrm{pe}}}{M(\gamma)} \qquad [\mathrm{m}^2] \tag{3.11}$$

Where M is irradiance[7] of an the uniform beam of monochromatic photons, wide enough to light the optics, γ is the photon's incident angle and n_{pe} the number of detected photons per second. The larger $\mathcal{E}_{\mathrm{PD}}$ is the larger is the number of dteected photons and consequntly the lower is the energy threshold E_{th}.

$\mathcal{E}_{\mathrm{PD}}$ can be decomposed in factors which depend on the implementation of the instrument

$$\mathcal{E}_{\mathrm{PD}} = \varepsilon_{\mathrm{PD}} \cdot \rho_{\mathrm{el}} \cdot \mathcal{E}^{\mathrm{tri}}_{\mathrm{opt}} \cdot G \tag{3.12}$$

where $\varepsilon_{\mathrm{PD}}$ is the photo-detection efficiency of the photo-sensor, ρ_{el} is the efficiency of the electronics to measure the signal produced by the photosensor, $\mathcal{E}^{\mathrm{tri}}_{\mathrm{opt}}$ is the Optical Triggering Efficacy, related to the performaces of the optical system is basically proportional to the Entrance Pupil (EP) area (see Sec. 3.2.7) and G is the focal surface filling factor. $\varepsilon_{\mathrm{PD}}$ is limited to be smaller than 1. For standard photomultipliers, which have already been tested in the space environment and proved suitable for applications in space, $\varepsilon_{\mathrm{PD}} \simeq 0.12 \div 0.15$. Recently several new HighQE photodetectors became available on the market: GaAsP Hybrid Photodiodes (HPDs) and SiPMs. These devices, exploiting the intrinsic quantum efficiency of the silicon, aim to reach an $\varepsilon_{\mathrm{PD}}$ of $0.4 \div 0.6$. The best prototypes currently available have reached a sensitivity higher than Photomultipliers (PMTs) but many issues still remain open. The construction technology has to be refined to match the stability of the PMT and several open issues have to be tackled. Despite the current lack of reliability required by a space experiment, which has to operate unmanned for several years, it is conceivable that in the next years these problems will be solved, resulting in a photodetector 3 or 4 times more efficient. The SiPMs features seem especially suited for low-light space applications. Few mm thick, with a bias voltage

[7] $[M] = [\mathrm{ph}\cdot\mathrm{m}^{-2}\cdot\mathrm{s}^{-1}]$

of $50 \div 60$ Volts along with an high photodetection efficiency would considerably reduce the power and mass budget of the experiment. In Chapter 6 the feature of these devices are discussed and some measurements of their performances are presented.

Closely related to ε_{PD} is ρ_{el} as the electonics must be designed to fit the photo-sensor. For standard PMT working in photon counting mode and a digital electronics ρ_{el} can be as high as ~ 0.9. At higher light levels and with analog electronics ρ_{el} depends on the electronic's charge resolution.

The filling factor G is usually very close to 1. Square or exagonal photosensor can be organized in modules to tightly cover the whole Focal Surface (FS). A symmetric pattern is desirable to obtain a stronger structure that has better chances to tolerate the stress of the launch.

3.2.6 Optical system design

The two basic optical parameters, affecting both the performances and the engineering of the mission, are the EP diameter, D_{EP}, and the Field of View (FOV). The large desired aperture calls for an $f/\#$ as small as possible in order to reduce the size of the focal surface. However the large desired aperture implies, in any case, a large focal surface size.

Entrance pupil of the optics

Once defined the photodetector, the basic and unique sizable parameter, as far as the instrument sensitivity to low signals is concerned, is the optics aperture. The instrument's photon collection area is fixed by D_{EP}. In case of a refractive optics, the maximum D_{EP} corresponds roughly to the bay's diameter, while a deployable reflective optics could have a larger diameter. As a very large aperture optics is required a deployable optics might be required. The latter is more flexible than the former because depends also on the technology used for the optical system.

Note that the EP diameter is, basically, the only instrument parameter which can be sized, within external constraints. The lower limit of the allowed range of D_{EP} is set by the requirement on the energy threshold. The upper limit is fixed by external constraints (the tranporter's cargo bay).

FOV of the optics

The FOV, together with the satellite altitude, determines the geometrical aperture (discussed in the section 3.2.8) and therefore the number of events to be detected. The D_{EP} defines the detector's collection area and its

sensitivity, but also fixes the instrument size and, consequently, the mass and the volume of the payload.

The diameter D_{PD} of the focal surface is a function of the FOV (half-angle γ_{M}) and of the focal length F:

$$D_{\mathrm{PD}} = 2F \sin \gamma_{\mathrm{M}} \tag{3.13}$$

If we introduce the optics f-number, $f/\# \equiv F/D_{\mathrm{EP}}$ then

$$D_{\mathrm{PD}} = 2f/\# D_{\mathrm{EP}} \sin \gamma_{\mathrm{M}} \tag{3.14}$$

Note that for $\gamma_{\mathrm{M}} = 30°$ and $f/\# = 1$ the focal plane is as large as the EP pupil. A further discussion of these arguments can be found in [86].

As the instrument is basically photon-limited, the EP shall be as large as possible, up the limit allowed by external, technological and practical constraints. Therefore the size of the optics will be approximately set by the maximum allowable size. Therefore a reasonable assumption for any real instrument is that the focal surface is not larger that the optics: if the latter is approximated by the EP, as it would be desirable for a high-efficiency optics, this implies the rough estimate: $2f/\# \sin \gamma_{\mathrm{M}} \lesssim 1$

3.2.7 Optical triggering efficacy

To quantify the performances of the optics O we parameterize its behavior as a function of the photons' incident angle γ and wavelength λ. For each γ and λ we are interested in the number of photons reaching a predefined region close enough to the centroid of the spot. All the photons outside that region are considered lost. Given an uniform beam of monochromatic photons of irradiance M, wide enough to light the whole EP, we define the optical efficacy as

$$\mathcal{E}_{\mathrm{opt}}(\gamma) = \frac{n_{\mathrm{ph}}(d_b)}{M(\gamma)}$$

where n_{ph} is the number of photons per time unit within a circular bucket of radius d_b on the focal surface. The efficacy takes into account both the optic's focusing power and transmission properties in one parameter, directly relating the incoming radiance to the number of photons on the focal surface. It has the dimension of an area and represents the optics effective collection area. If the bucket matches the size of the photodetector's pixel and $\varepsilon_{\mathrm{PD}}$ is the photosensor's photo-detection efficiency, $n_{pe} = \mathcal{E}_{\mathrm{PD}} M = \varepsilon_{\mathrm{PD}} \mathcal{E}^{tri}_{\mathrm{opt}} M$ is the expected number of photoelectrons in the

pixel per time unit. In this case the efficacy is named triggering $\mathcal{E}^{tri}_{\rm opt}$. The number of photoelectrons in a time interval Δt is

$$N_{\rm pe} = \varepsilon_{\rm PD} \int_{\Delta t} {\rm d}t \int_{\Delta\lambda} {\rm d}\lambda \, \mathcal{E}^{tri}_{\rm opt}(\gamma, \lambda) \, \frac{{\rm d}M(t,\lambda)}{{\rm d}\lambda}. \tag{3.15}$$

To discuss the minimum performances of the detector and define the requirement on the size of an UHECR telescope we introduce an ideal optical system O_{id}. We define an O_{id} as a light collector system, refractive or reflective, which focuses all the photons crossing it entrance surface S^{id}_{O} into a point-like spot over the focal surface. S^{id}_{O} can be assumed flat, which is a rather general hypothesis within the constraints of a space experiment. The amount of photons per second collected by O_{id} is $n_{\rm ph} = (\vec{M} \cdot \vec{n})\, S^{id}_{O}$ from which follows

$$\mathcal{E}_{\rm opt} = S^{id}_{O} \cos\gamma. \tag{3.16}$$

The $\cos\gamma$ dependence is the natural consequence of the absence of an aperture correction device among the hypothesis. For the observation of UHECR, the priorities are a good local uniformity (few degrees) of the optics response, a small and sharp point spread function and low absorption, while the global lack of uniformity within the FOV is not critical because, like in the case of O_{id}, doesn't spoil the shape of the signal.

Number of detected photons, efficacy and energy resolution

The required 30% energy resolution implies a relative error due to the statistics of the detected photons not larger than $\sigma_N/N \sim (0.10 \div 0.15)$, assuming an equal contribution from statistical and systematics errors, as it is appropriate for a well-designed apparatus. This implies a number of detected photons per EAS at least of the order of one hundred (for $E \approx 10^{19}$ eV).

Using $O_{\rm id}$ and applying the relations described in the previous section to $\mathcal{S}_{ref}$ we can derive the requirement on the optical triggering efficacy from the requirement on the energy resolution. The angular extension of $\mathcal{S}_{ref}$ is about 1.5° (Tab. 3.2, Fig. 3.7) so that the properties of the optical system can be considered constant and consequently $\mathcal{E}^{tri}_{\rm opt}$ accordingly. The flux of photons generated by the whole development of the shower is 58 ph/m^2 (Tab. 3.2).

The $\mathcal{E}_{\rm PD}$ necessary to detect one hundred photons follows from the

definition eq. 3.12.

$$\mathcal{E}_{\rm PD}(\gamma = 20^\circ) = \frac{N_{pe}}{F} \simeq 1.7\ {\rm m}^2 \tag{3.17}$$

This result is independent from the implementation of the optical system and on the photosensor employed but to proceed to calculate the requirements on the $\mathcal{E}_{\rm opt}$ a value for $\varepsilon_{\rm PD}$ must be chosen. Since $\mathcal{E}_{\rm PD} = \varepsilon_{\rm PD}\mathcal{E}_{\rm opt}$ the efficiency of the photodetector has a strong impact on the requirements on the optics and on the size of the instrument. As introduced in Sec. 3.2.5, there are two main possibilities, standard PMTs and HiQE-PMTs. To be conservative we assume to use the standard PMTs with $\varepsilon_{\rm PD} = 0.12$

$$\mathcal{E}_{\rm opt}(\gamma = 20^\circ) \simeq 15\ {\rm m}^2 \tag{3.18}$$

If applied to the $O_{\rm id}$, the triggering optical efficacy at $\gamma = 0$, $\mathcal{E}^{tri}_{\rm opt}(0^\circ)$, is not only the effective collection area but also the physical area of the optics and consequently a requirement on the size of the telescope. Translated into minimum diameter for the optics we obtain, using (3.16),

$$\begin{aligned} S_{\rm min} &= \mathcal{E}^{tri}_{\rm opt}(0^\circ) = \frac{\mathcal{E}^{tri}_{\rm opt}(20^\circ)}{\cos 20^\circ} \simeq 16\ {\rm m}^2 \\ D_{\rm min} &= 2\sqrt{\frac{\mathcal{E}^{tri}_{\rm opt}(0^\circ)}{\pi}} \simeq 4.5\ {\rm m} \end{aligned} \tag{3.19}$$

This result can't be applied without accounting for the absorption, reflection and shape of the point spread function of a real optical system. The inefficiencies may reduce the amount of photons in the bucket to $20-25\%$, depending on the employed technology. Therefore, the previous lower limit $D_{\rm min}$ may rise by a factor of 2.

3.2.8 Aperture

In order to estimate the instrument's aperture we must know, at first, the geometrical area spanned by the FOV on the Earth's surface. The simplest case occurs when the detector is pointing at nadir. The area on ground A_0 is simply the area of a spherical cap,

$$A_0 = 2\pi R^2_\oplus (1 - \cos\beta_{\rm M}), \tag{3.20}$$

being $R_\oplus = 6378.14$ km the Earth's radius, γ_{max} the FOV (semi-angle) and β_M the angle at Earth's center between nadir and the FOV's border as shown in Fig. 3.10a:

$$\beta_M = \arcsin\left(\frac{R_\oplus + H}{R_\oplus}\sin\gamma_{max}\right) - \gamma_{max} \tag{3.21}$$

In this case one cannot neglect the Earth's curvature. For $H = 400$ km and $\gamma_{max} = 30°$, we have $A_0 \simeq 1.71{\cdot}10^5$ km^2.

At high energy where the shower signal is strong and the UHECR flux is low, the aperture may be increased tilting the detector from the nadir direction by an angle α_{tilt}. The easiest way to calculate the area in the FOV, the intersection of the FOV cone with the Earth surface, is to use a simple Monte-Carlo integration, because the geometrical solution is rather complex. We ran the Monte-Carlo over several values of α_{tilt}, from 0° to 40°.[8] The result is shown in Fig. 3.10b.

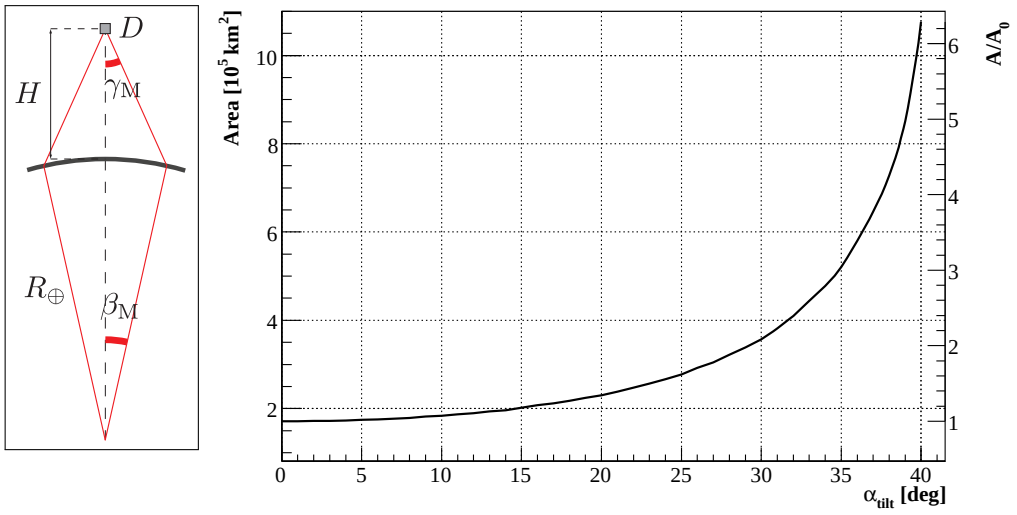

(a) (b)

Figure 3.10: (a) Scheme of the FOV area (b) Area seen by the detector at the Earth's surface versus α_{tilt}, for $H = 400$ km and $\gamma_{max} = 30°$. On the right axis, the area is shown in units of A_0

[8] For $H = 400$ km the horizon angle is $\beta_{hor} = \arcsin\frac{R_\oplus}{R_\oplus + H} \simeq 70°$. If $\gamma_{max} = 30°$, $\alpha_{tilt} = 40°$ is the maximum tilt angle for which the FOV is enclosed within the horizon.

The general expression for the geometrical aperture is:

$$\mathcal{A} = \pi A_0 f(\alpha_{\text{tilt}}) \left(\sin^2 \theta_{\text{max}} - \sin^2 \theta_{\text{min}} \right) \tag{3.22}$$

where the area has been splitted into A_0 times the factor $f(\alpha_{\text{tilt}}) = A/A_0$ (fig. 3.10). To be conservative, we consider only the shower with a zenith angle $\theta \geq 30\,\text{deg}$, which are less truncated by the impact with the ground and have the best chances to be reconstructed correctly. For $\alpha_{\text{tilt}} = 0°$ we obtain a geometrical aperture of $\mathcal{A} \approx 4{\cdot}10^5$ km^{2}sr. if $\alpha_{\text{tilt}} \neq 0°$, the aperture is increased by the corresponding factor $f(\alpha_{\text{tilt}}) = A/A_0$ (Fig. 3.10). Another possibility could be a reduction of the FOV, compensated by a larger altitude or by a tilt, might have beneficial effects as it implies a smaller focal surface size and a better optics performance.

3.2.9 Pixel size and angular resolution

Any EAS will be seen as a point moving inside the FOV whose kinematics is fixed the EAS direction. In every moment is induces a natural decomposition of the EAS's velocity in two components: one parallel to the line of sight from the instrument to the instantaneous position of the EAS and the other lying on the perpendicular plane. As the EAS develops approximately at the speed of light, both of them can be reconstructed out of the two-dimensional image on the focal plane plus the time information.

In particular the former is inferred from the observed angular velocity of the EAS inside the FOV, while the latter can be reconstructed out of the direction of the EAS' track on the focal plane.

To factors concurs to the choice of the optimal pixel size δ: the scientific requirements and the limited resources available resources. The pixel size affects:

- the trigger efficiency and the signal contamination: the number of signal photons divided by the number of random background photons on the pixel roughly scales as $S/B \sim 1/\delta$ for a pixel larger that the EAS track width on the focal surface (which basically depends on the optics point spread function) while it saturates to a constant for small enough pixel size;
- the angular resolution;
- the X_{max} resolution (i.e. the primary particle identification capabilities).

The faintness of the EAS signal at the lower energies makes necessarly to have the pixel size has not larger than the istantaneous image of the shower on the focal plane. Due to the large distance, the EAS' image is point-like, therefore the pixel has to match the Point Spread Function of the optics. Moreover, the number of pixels has a strong impact on the Instrument budgets and complexity. A trade-off on the pixel size is therefore very important.

An approximate and simplified analysis, leading to determine the required pixel size, is presented below. Note that the following elementary analysis ignores the effect of the background (making the angular resolution worse) and assumes to have an unbiased estimator of the EAS arrival direction. Therefore the derived requirements must be considered as necessary requirements. On the other hand the use of the diffusely reflected Cherenkov flash might improve the angular resolution.

Angular resolution perpendicular to the line of sight

The expected angular resolution $\Delta\beta_\perp$ on the EAS direction perpendicularly to the line of sight is readily estimated by assuming to perform a linear fit. In this case one has for the error on the angle:

$$\Delta\beta_\perp \approx \frac{\delta}{\sqrt{12}} \frac{1}{\sigma_\alpha} \frac{1}{\sqrt{N}}, \tag{3.23}$$

where N is the number of detected photons, σ_α is the standard deviation of the observed EAS image (easily determined from simulations) and δ is the uncertainty on the position on the focal surface which can be roughly taken as the pixel size;

Using again the sample EAS (table 3.2) and exploiting the Gamma-like shape (Gaisser-Hillas function) of the EAS longitudinal profile, the relation between the observed (angular) EAS length, α_{EAS}, (i.e. the range of the sampled values) and σ_α turns out to be $\alpha_{\mathrm{EAS}} \approx 5\sigma_\alpha$ (for $N = 100$), as discussed in Sec. 3.2.3. Therefore one finds that, in order to reach an angular resolution of the order of $\Delta\beta_\perp \sim 1^\circ$, a FOV granularity of $\delta \sim 0.1^\circ$ is required.

Angular resolution parallel to the line of sight

The relation between the observed angular velocity ω_{EAS} and the angle β between the EAS velocity vector and the line of sight (Fig. 3.11) is the

well known relation:

$$\omega_{\mathrm{EAS}} = \frac{c}{R}\left(\frac{1-\sin\beta}{\cos\beta}\right) = \frac{c}{R}\tan\left(\frac{\beta}{2}\right) \tag{3.24}$$

where c is the speed of light and R is the distance of the EAS. In the present case, one assumes that the EAS develops in the lower layers of the atmosphere, within ~ 15 km from the ground so that R is approximatively known (the relative error is $\Delta R/R \lesssim 0.05$).

Due the non-linear relations between ω_{EAS} and β the estimation of the best fit error is more complex in this case. Therefore the error on β is estimated by assuming a simple measurement of the angular velocity of the EAS. One obtains:

$$\Delta\beta_{\|} = \frac{\Delta\omega_{\mathrm{EAS}}}{\omega_{\mathrm{EAS}}} = \left(\frac{\delta}{\alpha_{\mathrm{EAS}}} + \frac{\delta_T}{T_{\mathrm{EAS}}}\right). \tag{3.25}$$

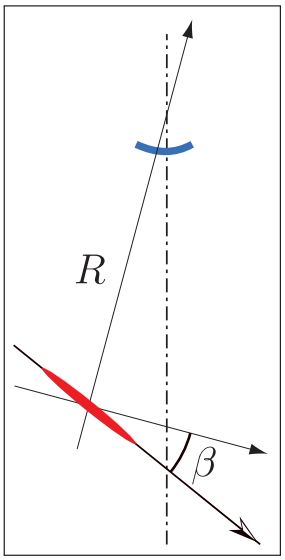

Figure 3.11: Scheme of the shower-detector system

For the typical EAS of table 3.2, by assuming an EAS sampling time not larger than $\delta_T \sim 2.5$ μs the second term is smaller than the first one. One finds $\Delta\beta_{\|} \approx 0.15$ rad $\approx 10°$ by assuming again $\delta \sim 0.1°$. One might assume that, with a best fit, this results will scale as $N^{-1/2}$ obtaining the desired $\Delta\beta_{\|} \approx 0.015$ rad $\approx 1°$. Therefore one finds that, in order to aim to get an angular resolution of the order of $\Delta\beta_{\|} \sim 1°$, one needs $\delta \sim 0.1°$ and $\delta_T \sim 2.5$ μs. Note that, as long as δ_T is smaller than the pixel transit time the error is dominated by the pixel size and not by timing.

3.2.10 Time resolution

The sampling time τ shall be tuned to maximize the signal to noise ratio and the longitudinal profile sampling.

The optimal sampling time τ_{opt}, defined as the sampling time foe which the signal to noise ratio is more favourable, corresponds to the transit time of the EAS signal of the shower spends in one pixel of the FS. Assuming the angular pixel size δ fixed by the requirements on the angular resolution, the value τ_{opt} depends only on the angular velocity of the EAS signal, $\tau_{\mathrm{opt}} = \delta/\omega_{\mathrm{EAS}}$. A shorter τ keeps the S/N constant and provides, in principle, a more accurate sampling of the EAS which may be employed in the

reconstruction algorithms. However, in the cases when the signal is very faint, the task of the trigger becomes difficult and would probably require complicate on-line trigger algorithms. The sampling time length must also take into account the constrains on the telemetry, since the data flow that must be transitted to the ground stations is $\propto 1/\tau$. A larger transit time would reduce the fluctuations but also collect more background because the number of background photoelectrons integrated in the pixels with signal depends on the sampling time

$$N_{\rm bck} = n_{\rm s}\nu_{\rm B}\tau \simeq \begin{cases} \frac{\zeta_{\rm EAS}}{\delta}\nu_{\rm B}\tau & \text{if } \tau < \tau_{\rm opt}, \\ T_{\rm EAS}\nu_{\rm B} & \text{if } \tau > \tau_{\rm opt}, \end{cases} \tag{3.26}$$

being $n_{\rm s}$ the number of samples with at least a signal photoelectron and $\nu_{\rm B}$ the background rate per pixel. The equation (3.26) shows that, if $\tau > \tau_{\rm opt}$, $N_{\rm bck}$ is proportional to the EAS extension and to the sampling time and consequently $S/N \propto 1/\tau$. The effect is negligible for short showers and becomes more relevant for very inclined showers. Unfortunately $\tau_{\rm opt}$ varies with the angle between the shower's direction and the line of sight ζ up several orders of magnitude as shown in Fig. 3.12.

However, the range of τ can be narrowed using simple considerations.

The lower limit is the shortest transit time allowed by the geometry which is the transit time in a pixel of an horizontal EAS below the detector:

$$\tau_{\rm min} = \frac{\delta H}{c} = 2.4\ \mu{\rm s} \tag{3.27}$$

On the other hand, τ should be short enought to allow a good sampling of the longitudinal profile in the core region for the fit of the shower maximum. From Tab. 3.3 the $\mathcal{S}_{ref}$ core length is $\approx 36 \div 48\ \mu$s and at least 5/6 bins are necessary for the profile fit. Therefore τ should not exceed $6 \div 8$ ms. The present assessment does not take into account the background.

3.2.11 $X_{\rm max}$ resolution

The requirement $\Delta X_{\rm max} \leq 35$ g/cm^2 is satisfied following the previous Instrument Requirements. In fact the relation between slant depth X and the coordinate along the EAS l is, in the approximation (3.6) and neglecting the Earth's curvature:

$$\left|\frac{{\rm d}X}{{\rm d}\ell}\right| = \frac{|\cos\theta|}{h_0}X. \tag{3.28}$$

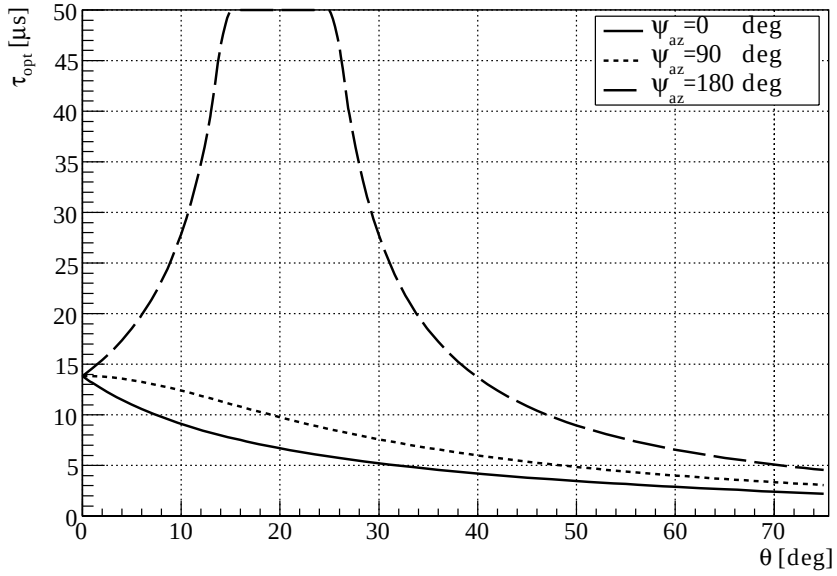

Figure 3.12: The optimal sampling time $\tau_{\rm opt}$ as a function of the zenith angle θ for $\psi_{az} = 0°, 90°$ and 180° (at $H = 400$ km, $\gamma = 20°$). When the EAS is moving away from the detector (as in the case $\psi_{az} = 180°$), at the limit where $\hat{v}$ and $\hat{\sigma}$ are aligned ($\theta = 20°$) the shower image has no angular extension and $\tau_{\rm opt}$ diverges. If the alignment doesn't occur $\tau_{\rm opt} \leq 15$ ms

Therefore for $\mathcal{S}_{ref}$ the $\Delta\ell$ corresponds $\Delta X_{\rm max} \sim 35 {\rm g/cm}^2$ ($X_{\rm max} \sim 824 {\rm g/cm}^2$) is larger than 0.49 km. Therefore, neglecting the geometrical and kinematical details of the EAS development, it is larger than half the pixel size projected at the Earth[9]. The required $X_{\rm max}$ resolution is therefore compatible with the pixel size. A resolution $\Delta X_{\rm max} \sim 20 {\rm g/cm}^2$ might be reached by a suitable fitting procedure.

3.2.12 The Background

Due to the low expected signal level the noise level has to be kept well below the physical background level. The random mean background detected by the whole apparatus, mainly due to the atmospheric nightglow, is $B \approx (3 \div 9) \cdot 10^{11}$ ph$\cdot$m$^{-2}\cdot$s$^{-1}\cdot$sr^{-1} (from the results of the experiments NIGHTGLOW [87], BABY [88] and Arizona-Airglow [89] and

[9] For an orbital height $H \sim 400$ km and a pixel granularity of $\Delta\alpha \sim 0.1°$, the pixel size projected on ground is ~ 0.8 km.

the Universitetsky-Tatiana microsatellite [90]) in the wavelength range 330 nm $\leq \lambda \leq$ 400 nm. Therefore the random background rate in the detector is

$$\mu_{\mathrm{B}} = BA\Omega_{\mathrm{det}}\varepsilon_{\mathrm{PD}}\,. \tag{3.29}$$

With a collection area (in the case of an ideal optics) $A = \mathcal{E}^{tri}_{\mathrm{opt}}(0^\circ) \simeq 16\ \mathrm{m}^2$, a photo-detection efficiency $\varepsilon_{\mathrm{PD}} = 0.12$ and $\gamma_{\mathrm{max}} = 30^\circ$, corresponding at a solid angle $\Omega_{FOV} \simeq 0.84$ sr, the background rate expected is $\mu_{\mathrm{back}} \simeq (4.8 \div 15)\cdot 10^{11}\ \mathrm{ph\cdot s^{-1}}$ over the full FOV.

For a given pixel granularity $\Delta\alpha$, the number of pixel in the detector is $n_{\mathrm{pix}} \simeq \Omega_{\mathrm{det}}/(\Delta\alpha)^2 \approx 2.8\cdot 10^5$ for $\Delta\alpha = 0.1^\circ$.

Following the previous result, the intrinsic Instrument noise (all sources) is required to be less than three GHz (over the whole Photo-Detector) in order to be negligible with respect to the natural background. Note that this requirement also include the effect of the stray-light.

Chapter 4

The *EUSO* project

In this chapter we will introduce the *EUSO* experiment, in whose context the work described in this document was carried on. *EUSO* mission was proposed to ESA as a pathfinder in the observation of UHECR cosmic rays by means of a 2.5 m, 30° FOV telescope installed on the ISS. A large part of the work of this thesis has been focused on the development of the *EUSO* software framework for the Monte-Carlo simulation and reconstruction, ESAF. We aimed to create a full simulation and reconstruction chain, starting from the primary particle interacting in the atmosphere to the reconstruction of the primary parameters from the detector's simulation data. The task is complex due to the large number of effects which must be included to obtain a realistic Monte-Carlo simulation. One of the most critical aspects is the atmosphere which is continuously changing due to the orbital motion of the ISS. As regards the detector simulation, ESAF was developed in the *EUSO* feasibility study which during which the design of the instrument has undergone several major changes. We had to provide the instrument's simulation with a flexible structure in order to follow the modifications. A preliminary but detailed work on the reconstruction software has been carried out as well, focused on the most relevant parameters: energy and direction.

In future prospect, ESAF is also suitable for the simulation of any spaceborne apparatus for the observation of UHECR. The modular structure can accommodate any future detector with a small effort. A complete set of tool to to derive the ancillary quantities from the Monte-Carlo code, like the optical triggering efficacy of the expected background rate on the focal surface has been implemented.

ESAF is currently used in the mission planning for a ESA Cosmic Vision proposal to be submitted in the next future.

4.1 The *EUSO* mission

The first proposal for the *EUSO* project was submitted to ESA in response to the Announcement of Opportunity for a free-flyer mission in 1999. The original design was a 3.5 m diameter telescope, as the available volume, mass, power and telemetry resources on a free flyer were less constrained compared to the ISS. The altitude of the orbit was a free parameter that could be adjusted to span over different energy ranges and increase the acceptance at the energies where the UHECR flux is very small. In 2000 ESA recommended to consider the accommodation on the ESA Columbus module on the ISS. After a successful adaptation study, *EUSO* was accepted as a payload of the Columbus module and an ESA mission feasibility study (Phase A) started in 2001.

The accommodation on the ISS

The accommodation process had a strong impact on the mission performances. The orbit was fixed by the ISS and influenced by the solar cycle (see Fig. 4.1 and 4.2). The resources on the ISS are limited, and the payloads are constrained in mass ($\lesssim 1.5$ tons), power ($\lesssim 1$ kW), volume and telemetry ($\lesssim 180$ Mbit/orbit). The collecting power of the instrument was reduced by a factor of two. The design of the instrument within these constraints is very challenging considering the huge number of channels ($\approx 10^5$), the on-board self-triggering electronics and all the issues related with the security and the unmanned operations in space for several years. Despite the difficulties the strength of the scientific case remained intact and after a successful Phase A, in mid 2004 *EUSO* was declared technically ready to proceed to the "Study Phase", the Phase B. Despite of the the feasibility study success, *EUSO* was not allowed to proceed to Phase B and put on hold due to financial and programmatic issues related to the Columbia Space Shuttle accident in 2003. However, ESA recognized the soundness of the scientific case and recommended the *EUSO* community to apply for free-flyer mission in the context of the ESA Cosmic Vision.

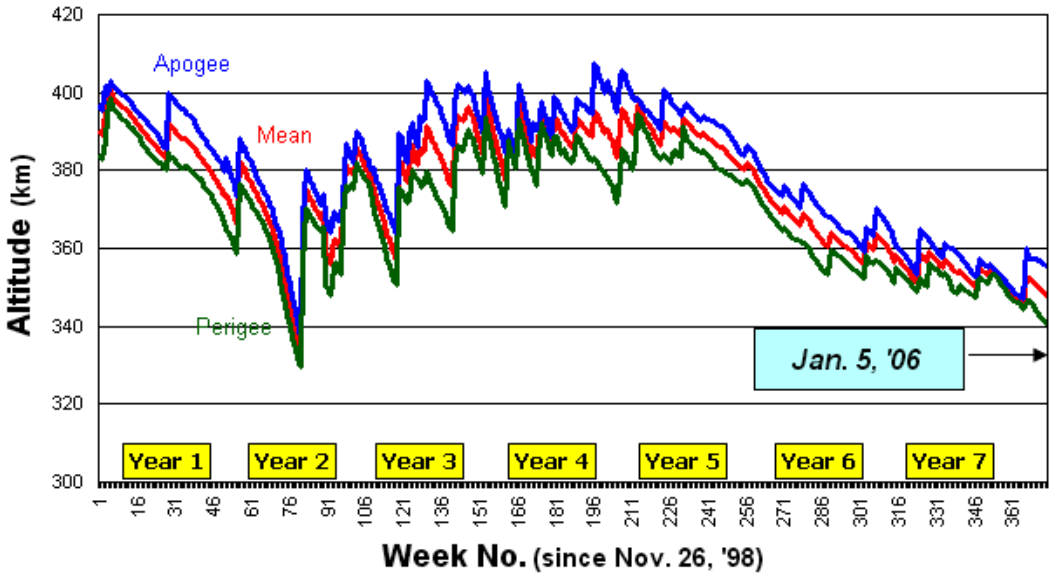

Figure 4.1: History of the orbital altitude of the ISS.

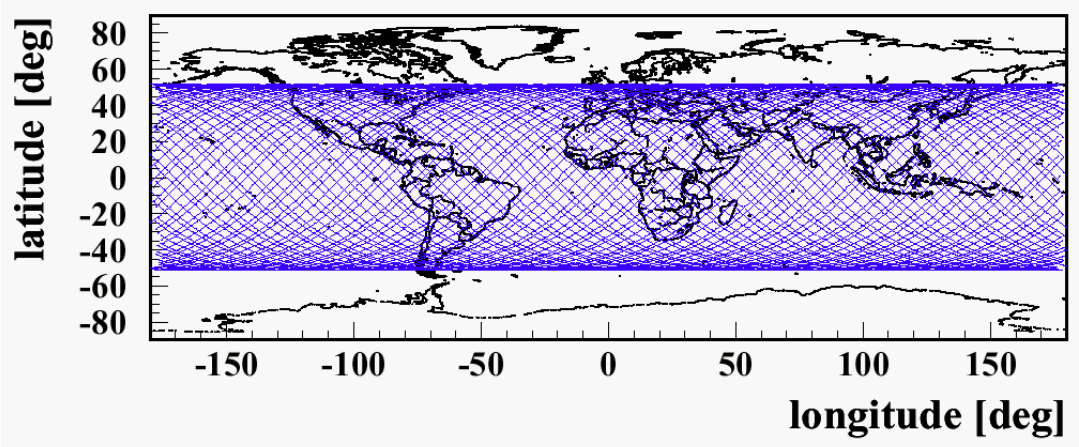

Figure 4.2: The ISS orbit.

EUSO parameters and design goals	
Desired pixel size at the Earth surface	$\Delta \simeq (0.5 \div 1.0)$ km
ISS average orbit height	$H \approx 430$ km (in 2010)
Observation duty cycle	$\eta \simeq (0.10 \div 0.15)$
Orbital period	$T_0 \simeq 90$ min
Operational lifetime	> 3 yr
Effective aperture $\mathcal{A}^{\rm eff}$	$\simeq (6 \div 9) \cdot 10^4$ km^2·sr
Optics maximum diameter	$D_M \simeq 2.5$ m
$\mathcal{E}_{\rm opt}(\gamma)$	$1.6 - 0.28\gamma^2 - 2.1\gamma^4$
Optics $f/\#$	$f/\# \leq 1.25$
Optics FOV (half-angle)	$\gamma_{\rm max} \simeq 30\,$deg
Optics spot size diameter on the FS	$3 \div 6$ mm
Average transmission of the optics	$K_{opt} \approx 0.5$
Overall PD detection efficiency	$\varepsilon_{\rm PD} \approx 0.1$
Pixel dimensions	$\approx 3 \div 6$ mm
Number of channels	$\approx 10^5 \div 4 \cdot 10^5$
Overall atmospheric transmission ($330 \leq \lambda \leq 400$ nm)	$K_{atm} \gtrsim 0.4$
Background ($330 \leq \lambda \leq 400$ nm at ≈ 400 km height)	$B \approx (3 \div 9) \cdot 10^{11}$ ph·m^{-2}·s^{-1}·sr^{-1}

Table 4.1: The *EUSO* parameters and design goals.

4.1.1 The Instrument

The reader should remember that the Phase A study leaves many open issues and that the design is brought to the final version during the Phase B. However, the *EUSO* instrument has reached a considerable maturity and the gathered experience is the starting point for any new mission. First an overview of the instrument will be given and afterward the main subsystems will be discussed in detail.

The basic logical and functional components of the *EUSO* Instrument (Fig. 4.3) are:

i) The main (refractive) optics, the Optical Module (OM), based on Fresnel lenses, to collect the incoming light and focus the EAS track image onto the Photo-Detector on the Focal Surface.

ii) The Photo Detector (PD) on the FS of the main optics, detecting the near-UV light focused by the main optics and providing both position and arrival times.

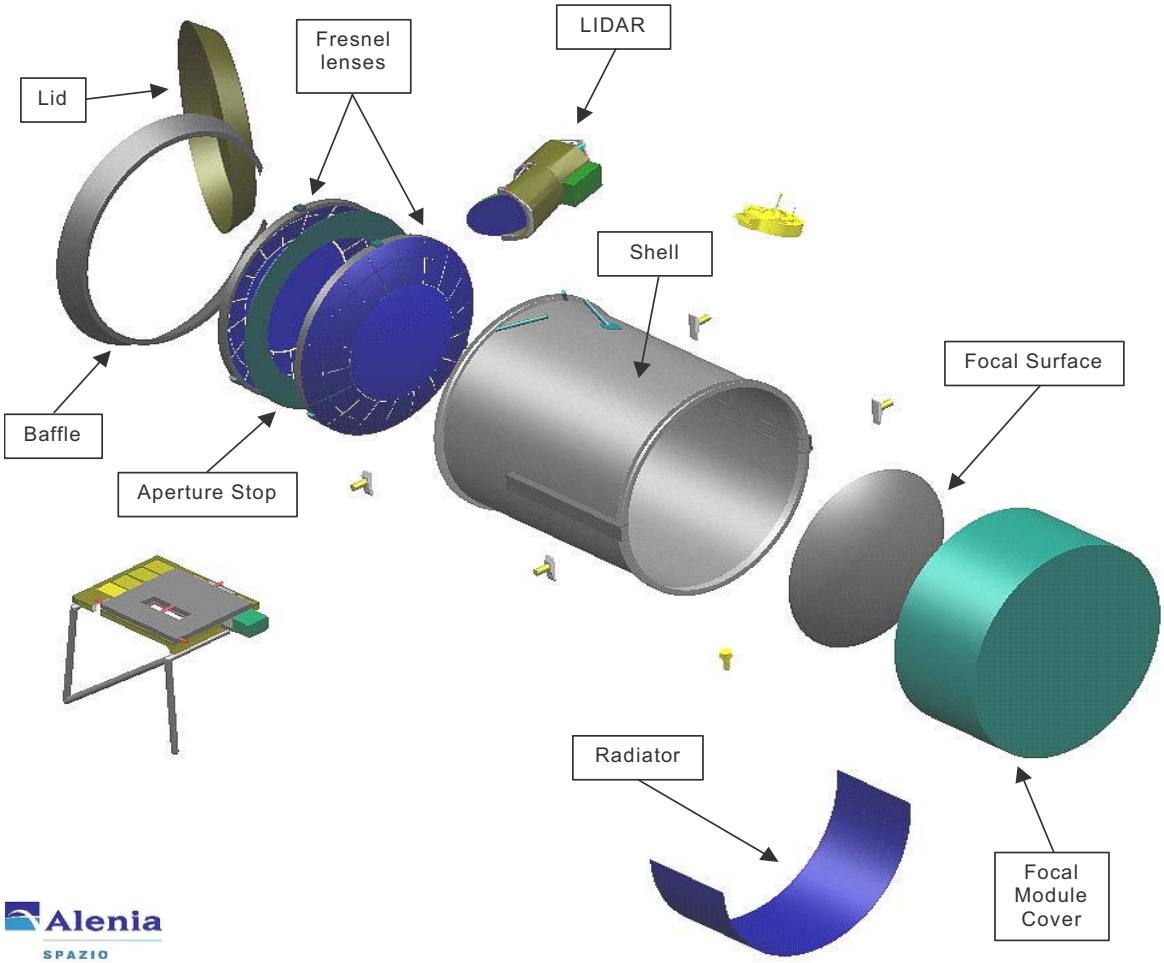

Figure 4.3: The *EUSO* instrument.

iii) The System Electronics, controlling the Instrument at system level, performing the Trigger and Data Handling at system level and interfacing to the *EUSO* Payload.

iv) The Instrument Structure, including the external and internal structures, the body and envelope, the lid and the baffle as well as the meteoroids, orbiting debris and thermal protections and blankets

Optics

The *EUSO* optical system is The flow down from the scientific objectives of the *EUSO* mission yields the baseline requirements for the OM, including

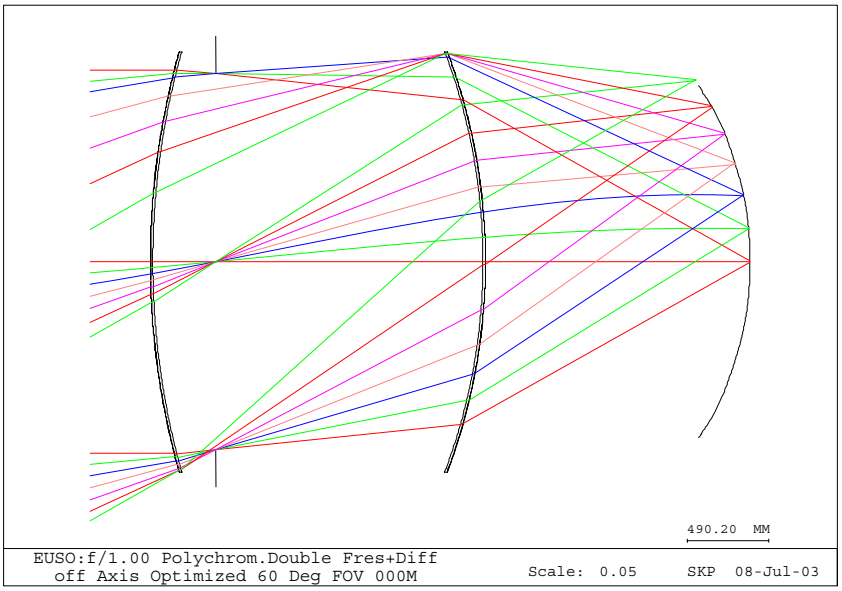

Figure 4.4: *EUSO* Optical Module design baseline.

the imaging characteristics of the light-collecting Telescope. The OM key design parameters are:

- A $330 \div 400$ nm optical bandwidth. This bandwidth provides the best signal to noise ratio for detecting both the air fluorescence signal and the Cerenkov signal.

- A triggering efficacy, in square meters, larger than $\mathcal{E}_{\rm opt}(\gamma) = 1.6 - 0.28\gamma^2 - 2.1\gamma^4$ is required for the collection and detection of the faint fluorescence from EAS with energies above $3{\cdot}10^{19}$ eV and full Instrument sensitivity above 10^{20} eV.

- A full angle FOV larger than 50°. This large FOV allows EUSO to view a sufficiently large volume of atmosphere to ensure a sufficient statistical sample of EAS events at high energies.

- A 6 arcmin ($\simeq 0.1°$) angular resolution. This resolution corresponds approximately to 0.8 km on the Earth.

- A fast optics with $f/\# = 1.00$, limited in size to be 2.5 m in diameter. The deployment of *EUSO* by the Space Shuttle and its attachment to the ISS place severe limits on the mass and size.

The *EUSO* mission has an unusual set of requirements to be met by an optical system. The large aperture, the wide FOV, and the low $f/\#$ requirements, coupled with the mass and size constraints are major challenges. On the contrary the resolution of the *EUSO* Telescope is three orders of magnitude less stringent than a diffraction limited astronomical Telescope.

The Photo Detector

One of the main driving points of the PD design is to combine different functions as much as possible, in order to save mass and volume. The packing of the devices has to be optimized to reduce losses in the geometrical acceptance, due to dead regions between the close packed devices, and defocusing effects, originating from a positioning of the sensor at some distance from the ideal FS.

A modular structure is preferred. Therefore the overall structure shall consist of small autonomous functional units Elementary Cell (EC) assembled in larger modules Photo-Detector Modules (PDM) as shown in Fig. 4.5. The EC consists of a limited number of Multi Anode PhotoMulTiplier (MAPMT) sharing some common resources. The EC can be a thick multi-layered Printed Circuit Board (PCB). Several EC form a PDM. PDM are independent structures tied to each other by a common support structure and having a shape determined by the layout of the FS. The EC concept is useful because it implements the desired modular structure allowing the sharing of many resources among four MAPMT, such as the supporting PCB, the HV/LV lines, the MAPMT voltage divider, cables, connectors and electronic chips. This sharing improves the economy of the architecture and makes design, production and testing easier. It will be assumed that any PDM is made of an array of close-packed EC with a suitable shape, determined by the FS layout. Of course the detailed design of the PDM geometry will require the final fine tuning of the geometry of the optics FS, which needs the final design of the main *EUSO* optics.

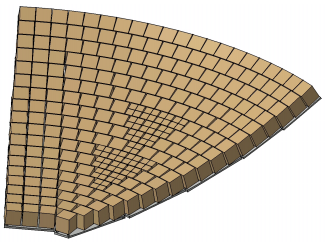

Figure 4.5: Sector of the *EUSO* focal surface. The big cubes represent the ECs while the small ones the MAPMTs

Electronics

The core of the *EUSO* electronics is the front-end chip installed on every EC. The front-end electronics must amplify the small signals from the sensors with a limited available power and without spoiling the fast sensor response. A programmable threshold is required to discriminate the signals. The ability to mask noisy or bad channels is very important, in order not to compromise the trigger operation. Detected photons must be counted for each channel during an externally driven time interval, the Gate Time Unit (GTU), in order to fire the first level trigger when the number is above a programmable digital threshold. The required logical signals for the trigger should be generated. The number of photons detected per channel must be stored for a sufficient time interval waiting for read-out in case of trigger. Required features are a very compact design with minimal distance between the sensors and the front-end electronics, a completely modular system with minimal cabling and self-triggering capabilities.

The *EUSO* front-end electronics is implemented in the form of an Application Specific Integrated Circuit (ASIC). The front-end ASIC provides both the MAPMT signal interface and the pixel-level trigger. The main functions of the *EUSO* ASIC are the following:

- Collect and pre-amplify the anodic signals via DC coupling.
- Discriminate the amplified anodic signals above a programmable analogue threshold. The threshold is individually programmable for each pixel from a fraction of a photoelectron up to several photoelectrons.
- Provide a photon counting capability with about 10 ns double-hit resolution and 10 bits of counter depth.
- Compare for every pixel the counted events within the GTU with a programmable digital value.
- Store the number of photoelectrons counted in each GTU into internal ring memories and allow readout of these memories when a trigger occurs; the depth of these memories will be large enough to allow waiting for the trigger. The baseline is 128 GTU depth.
- Accept commands, parameters and settings from a serial line and read-out through the same serial line.

4.2 ESAF, The EUSO Simulation and Analysis Framework

In the context of the *EUSO* collaboration, we have dedicated a big effort to build a dedicated Monte-Carlo simulation and to start the development of the core of the reconstruction software for *EUSO*.

In our intentions it will provide the scientists with a consistent framework for the whole process of data- simulations and data-analysis, from the simulation of the primary particle interaction in atmosphere, to the transport of light to the optical pupil, to the detector response simulation and finally to the reconstruction and the physical analysis. We designed ESAF so that each one of the above steps could be run individually and independently from the other ones. With this approach it is possible to run the same reconstruction and analysis code for the real data and for the simulated ones. Moreover, it is also possible to run single parts of this chain and check quantitatively the differences between different configurations of the detector or different approximations for the physical processes involved.

4.2.1 The Simulation of the Physical Process

The most common and sophisticated MonteCarlo programs [91, 92] provide a detailed description but paid with a very high computing time, even in their "thinning" versions. In ESAF, we have opted for a simulation focused on the correct treatment of the longitudinal EAS profile, the fluorescence yield and Cherenkov light emission with less emphasis on the tracking of all the secondary particles produced in the shower.

The code uses the hybrid approach UNISIM [93] and on EAS parameterization SLAST [94]. In UNISIM the EAS is simulated following all the particles produced in the showering process, according to the SIBYLL [95, 96, 97] minijet model for high energy hadronic interactions, down to a threshold energy ($E = 10^{17}$ eV, where E is the energy of the secondary particles, selected as a trade-off value between the accuracy of the fluctuation reproduction and the execution speed). Below this threshold a parametric description of the shower, based on a library of pre-simulated events is used, to work out the longitudinal profile. A global NKG fit is then used to generate the lateral particle distribution, relevant to simulate the shape of the EAS front, where the fluorescence and Cherenkov light starts from. The generation of Cherenkov light during each step of EAS propagation is calculated using the energy distribution of electrons given

in [98]. The angular distribution of the emitted photons is simulated using the parameterization of electrons angular distribution [99] convoluted with the Cherenkov cone emission. The UNISIM package includes also the LPM effect for electromagnetic interactions and it is able (unique in the panorama of the existing EAS generators on the market) to simulate neutrino interactions inside the target mass seen by the detector. As additional unique feature, UNISIM is able to simulate perfectly horizontal (90°) showers which develop perfectly horizontal without any interaction point with ground. Neutrinos charged current (CC) and neutral current (NC) differential cross sections used in the simulation for neutrino interactions have been calculated in the framework of QCD improved parton model. The effect of LPM interaction in neutrino induced showers is discussed in [93]. Both the shower maximum and its profile are affected (in case of CCν_e interactions, sometimes two clear peaks are observed in the EAS profile, due to hadronic and electromagnetic shower superposition, the latter being shifted by the LPM effect)

4.3 The Atmosphere Models

4.3.1 The Atmosphere as a light emission medium

The fluorescence yield. As already mentioned the fluorescence light is produced in the interaction of charged particles with air. The fluorescence spectrum of air consists almost entirely of nitrogen contribution. Light is emitted isotropically and is dominant in the wavelength region from 300 nm up to 450 nm. The light comes from the de-excitation of the two electronic states: the $2P$ band and the $1N$ band. From fig. 4.6a below one sees that the main contributing transitions lines are the $2P$ at 337.1 nm, 357.7 nm and 315.9 nm and the $1N$ at 391.4 nm and 427.8 nm. As the bandwidth of interest is in the range $330 \div 400$ nm, and since the atmospheric transmission is highly suppressed in the region below 330 nm by the ozone layer absorption, the simulation study concentrated, in the present Phase A study, on the fluorescence yield in the wavelength range $330 \div 400$ nm. The simulation of the fluorescence yield is based on the results of F. Kakimoto [85] and M. Nagano [100]. The dependence of the fluorescence yield with density ρ and temperature T is given by the $g_i(\rho, T)$ functions respectively for the 1N (391 nm) and $2P$ (337 and 357 nm) bands.

$$g_1(\rho,T) = \frac{\rho A_1}{F_1(1+\rho B_1\sqrt{T})} \quad , \qquad g_1(\rho,T) = \frac{\rho A_2}{2.76\cdot F_1(1+\rho B_2\sqrt{T})} \tag{4.1}$$

where ρ is in g/cm^2, T in Kelvin and $F_1 = 10^{-5}$ cm^2/g, $A_1 = 0.574$ cm^2/g, $A_2 = 0.927$ cm^2/g, $B_1 = 6.5{\cdot}10^3$ cm$^3{\cdot}$g$^{-1}{\cdot}$K$^{1/2}$, $B_2 = 1.85{\cdot}10^3$ cm$^3{\cdot}$g$^{-1}{\cdot}$K$^{1/2}$ are constants. The relative weights of the 337 and 357 nm wavelengths have been extracted from [101].

The dependence on ionization loss is also clearly established and the yield of fluorescence photons emitted by an electron of energy E is then parameterized by the following formula, in ph/(m·particle).

$$N_{ph}(E,\rho,T) = \left(\frac{\mathrm{d}E}{\mathrm{d}x}\right)_E \cdot \frac{g_1(\rho,T) + g_2(\rho,T)}{\left(\frac{\mathrm{d}E}{\mathrm{d}x}\right)_{E=E_0}} \tag{4.2}$$

where ρ is the local density and T the temperature, E_0 is a reference energy ($E_0 = 1.4$ MeV in [99]). The $\frac{\mathrm{d}E}{\mathrm{d}x}$ dependence given in [85], has been approximated by computing the weighted mean of the the energy spectrum of the electrons/positrons in EAS shower and assuming the mean value, $\langle E\rangle = 32$ MeV, and $\left(\frac{\mathrm{d}E}{\mathrm{d}x}\right)_E = \langle E\rangle$. Thus, the overall yield is normalized to achieve 4.8 ph·m^{-1} at normal conditions of pressure and temperature. The results given in [100] the pressure and temperature dependence given in (4.2) is confirmed, as a good approximation of the contribution given by six different emission bands. The overall yield is however higher by $\sim 10\%$. The energy dependence and the humidity dependence of the fluorescence yield are the main concerns, where a definite experimental effort is still required. Fig. 4.6b shows the behaviour of the total (right axis) and relative (left axis) yield of the three lines as a function of the altitude in a standard US atmosphere. An interesting feature is the rough independence of the yield from the altitudes below ~ 15 km: this is due to a compensation effect between the decrease of the number of molecules on one side (a smaller number molecules are excited by the secondary particles), and the increasing weight of radiative versus collisional de-excitation processes on the other side (more excited molecules de-excite through fluorescence emission at low density). A detailed work on the fluorescence yield dependence upon the atmospheric condition and its impact on the space observation is contained in [102].

Cherenkov light is produced as the charged particles in the EAS travel through the atmosphere faster than the speed of light in air, and is highly beamed forward along the shower axis with an aperture $\theta_{\max} \simeq 1.3°$. The energy threshold for Cherenkov light production is: $E_{th} = \frac{mc^2}{\sqrt{2(n-1)}}$, valid for $n \simeq 1$, where n is the wavelength-dependent refraction index at the current atmospheric depth. The number of Cherenkov photons emitted by a single particle of energy E, charge Ze and velocity $\beta = \frac{pc}{E}$, per unit path length, in

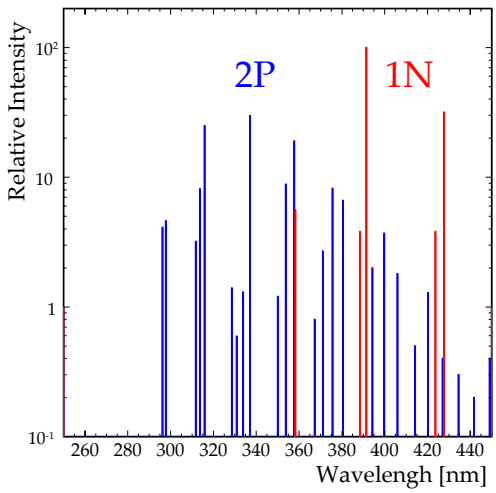

(a) The fluorescence emission lines of nitrogen.

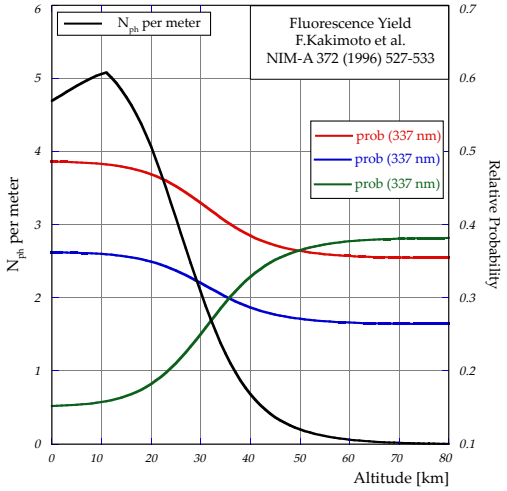

(b) On the left axis (black curve) the fluorescence yield, (ph/m^{-1}·particle^{-1}) as a function of altitude. On the right (coloured curves) the relative abundance of the three main fluorescence lines used in the calculations.

Figure 4.6: Nitrogen Fluorescence Yield

the wavelength range $\lambda_1 \div \lambda_2$ is described by the well known equation:

$$\frac{dN_{ph}^{\text{part}}(E)}{dx} = 2\pi\alpha Z^2 \int_{\lambda_1}^{\lambda_2} \frac{d\lambda}{\lambda^2}\left(1 - \frac{1}{(\beta n(\lambda))^2}\right) \tag{4.3}$$

with α the fine structure constant. The integral is limited to the value of λ for which $\beta n > 1$. To calculate the total amount of light produced by the EAS per meter, at the depth X, both the refraction index dependence on λ and X, as well as the charged particle energy distribution in the shower $f(E,X)$ has to be taken into account:

$$\frac{dN_{ph}(E)}{dx} = \int_{E_{th}}^{\infty} dE\, f(E,X) \frac{dN_{ph}^{\text{part}}(E)}{dx} \tag{4.4}$$

Since $n(\lambda)$ changes by less than 5% in the range $300 \div 400$ nm it can be assubed constant, while the dependece on the air density cannot be neglected.

4.3.2 The Atmosphere as a transmission medium

The transmission of the photons in the atmosphere is affected both by scattering (Rayleigh, Mie) and absorption effects. The Rayleigh scattering is produced by the air molecules, and is strongly wavelength dependent. When the diameter of the targets is of the order of the radiation wavelength, the Mie scattering takes place. Aerosols (dust, smoke, ...) in atmosphere and droplets (clouds) are responsible for Mie scattering of light. In the UV range of interest, absorption is mainly due to the ozone.

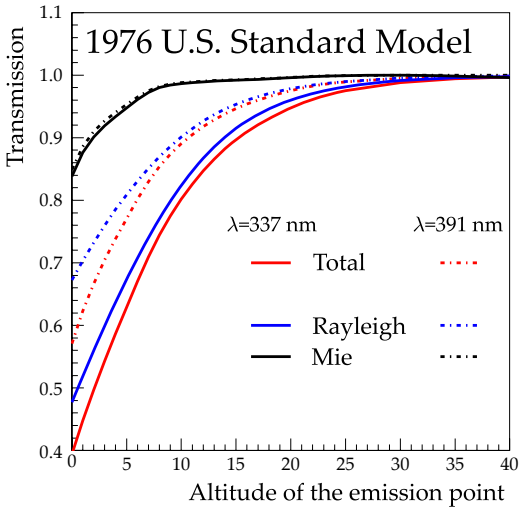

(a) Transmission as a function of the altitude of the starting point of the photons, for a vertical path, computed with LOWTRAN7, for two wavelengths, in case of the 1976 US Standard model. Contributions of Rayleigh and Mie ("Navy maritime" aerosols) scatterings are shown.

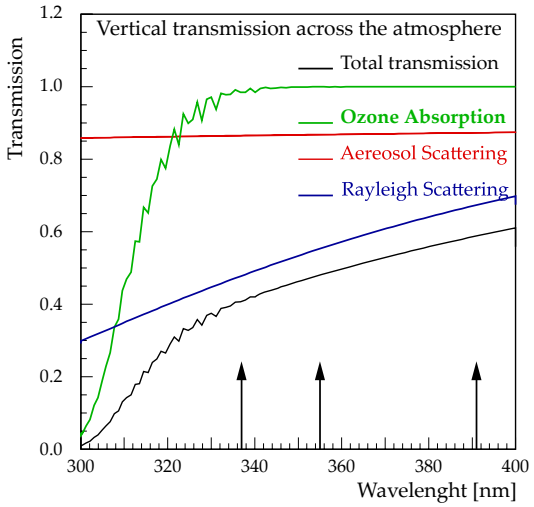

(b) The atmosphere transparency, for vertical paths, as a function of the radiation wavelength in a U.S. Standard atmospheric "Navy maritime" environment.

Figure 4.7: Nitrogen Fluorescence Yield

The impact of Rayleigh scattering, Mie scattering and Ozone absorption for different wavelengths and different atmospheric profiles has been studied with the LOWTRAN7 [103] program which allows to compute the light transmission, for different atmospheric models. It is important to notice that multiple scattering has been implemented but not used in the simulations.

In Fig. 4.7a, the transmission is plotted as a function of the altitude, given in kilometers, of the light emission point, assuming a vertical photon path and for two different wavelengths. To get the transmission curves

shown, the US Standard Model was used. It can be seen that the main light attenuation is due to Rayleigh scattering, in particular for low wavelength values, and that it is the dominant attenuation process in upper atmosphere. For $\lambda = 337$ nm, 40% of the light emitted from ground is transmitted to the detector on a vertical path, and 83% of the total attenuation is due to Rayleigh scattering. Fig. 4.7b shows the expected wavelength dependence of the attenuation for light emitted at ground level. While rather transparent for large wavelengths, ozone presents a sharp cut-off below ≈ 330 nm. Therefore, the influence of ozone is strongly dependent on the fluorescence light spectrum and on the bandwidth of the telescope. In Fig. 4.8a the effect of ozone on the light transmission as a function of the wavelength is plotted. To estimate the influence of the ozone thickness, the US standard ozone profile has been scaled by factors 1, 1.5 and 2. The effect is non negligible below 330 nm, and then it will have a larger impact on the Cherenkov light transmission than on the fluorescence one. The effect (reflection, diffusion) of a cloudy sky on the fluorescence and Cherenkov signals is treated in the next section. Using other atmospheric models has a tiny influence on the above results, provided that the aerosol contents are not modified, and even more, to the extent that clear, ideal atmosphere is a good representation of the real situation we will get on an event by event basis. Fig. 4.8b shows the attenuation of light when changing the aerosol models (the atmospheric model is fixed). The aerosols are mainly present in the boundary layer, and then the attenuation could be important for light emitted or transmitted at low altitudes.

The observational approach from space, contains some peculiarities, as far as the impact of the atmosphere is concerned, which turn essentially into a complication and several advantages:

Weather variability in the FOV

Due to the orbital speed mainly to the extent of the atmosphere portion contained in the FOV is the largest complication to be handled are the rapid variations of the atmosphere conditions at ground. The first step in the study of atmosphere variability and its effect on the radiative transfer is to test different atmospheric models. The US Standard Atmosphere 1976 models are commonly used in the atmosphere community. Using US Standard values as inputs whatever the space-time location of the EAS can lead to large systematic errors, in the UHECR energy determination or particle identification. As far as we are concerned by the global properties and profiles such as pressure, temperature and the number densities of the main constituents, it seems better to use the empirical models recommended by

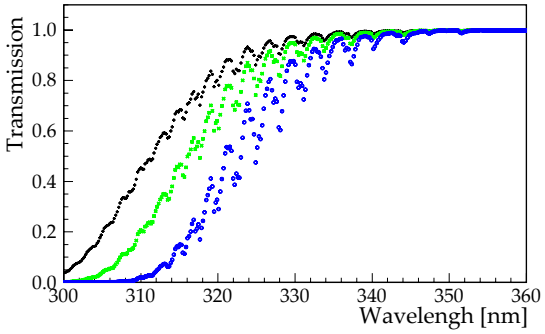

(a) Light transmission as a function of the wavelength in case of ozone absorption. The curves corresponds to three ozone profiles (US standard one scaled by factors 1, 1.5 and 2).

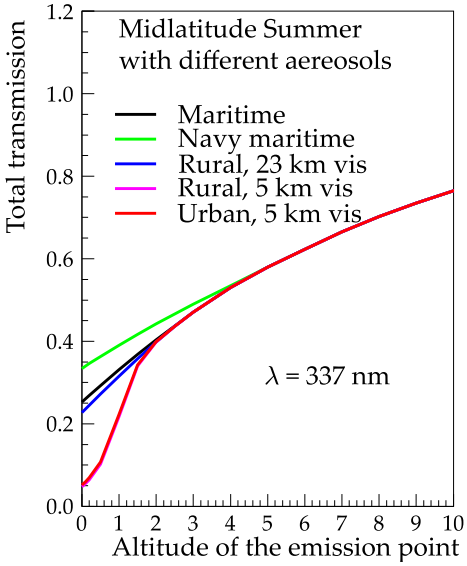

(b) Transmission as a function of the altitude computed with LOWTRAN7, for different types of aerosol contents and for a vertical path.

Figure 4.8: Ozone and Aereosols

the Committee for Space Research (COSPAR). The MSISE [104, 105, 106] model doesn't contain secondary constituents at low concentration at a given altitude such as water vapor, ozone or aerosols, which are of importance for light production and transmission. This lack of information can be recovered by the use of US-Standard Atmosphere 1976 profiles or by the data of a dedicated measurement. The use of MSISE model, although not implemented in this phase, will be added, in the full simulation software, with a twofold goal: modeling, in a detailed way, the real atmospheric environment, and retrieving, at the real event analysis stage, the actual atmosphere seen during the data taking.

The two sources of signal, fluorescence and Cherenkov light, suffer a different attenuation as a consequence of the atmosphere crossing. Fluorescence light in fact, isotropically emitted by the EAS, directly reaches the detector from its source, eventually suffering multiple scattering effect. Cherenkov light on the contrary, which is highly beamed around the shower axis, travels with the EAS "front" down to its "beam dump" surface, and bounces partially up diffusing again from it toward the detection site. This means a double path: from the source point to the Earth (the

clouds), and then back to the detector, for that part that, according to the reflecting surface albedo, diffuses upward in the atmosphere.

The contribution of the clouds

The clouds in the FOV modify the detector acceptance and the expected duty cycle. We have used the ISCCP International Satellite Cloud Climatology Project database [107] which provides extensive data on precise cloud situations around the globe as observed with satellite based atmosphere sounding devices. The ISCCP has divided the globe in equal 280×280 km^2 areas and gives, on a 3-hour period, a number of cloud parameters for each of these cells. Among the many accessible parameters for each cell, we use the clear sky fraction, the average cloud optical depth, the average cloud top altitude, the latitude, longitude and the nature (land, coast or sea).

Notice that, due to the type of atmospheric sounding devices used on these satellites, the data used in these calculations correspond to daytime measurements. Special attention should be given to the notion of the local clear sky fraction. In fact, each cell is itself divided into a variable number of sub-pixels. Each of these pixels is observed for cloud presence and the clear sky fraction is the fraction of the clear pixel. This definition does not therefore take into account the topology of the clear or cloudy pixels. Due to the extension of an UHECR EAS, this may lead to an overestimation of clear sky conditions. The effect of such over-estimation will be discussed below. As an example, Fig. 4.9 gives a representation of the total cloud amount (1 - the clear sky fraction) over the globe, averaged over the 1983-2004 period. This data, combined with reference to the seasonal variation, shows that, although could situations vary significantly over short periods of time, the average in time is quite stable. This allows us to have some confidence on the average values.

The atmospheric situation in the FOV and its variability will however impact also on the signal shape on an event-by event basis. The clouds coverage, the cloud topology, all the thermodynamical parameters in the area where an EAS develops and the trigger comes from, has to be known and corrected for to have a correct reconstruction of the parent longitudinal distribution generated by the primary Cosmic Ray.

4.3.3 The Expected background

Looking at nadir, the detector will be sensitive to the light coming from space and upward reflected through Earth albedo and to any source of light located in upper atmosphere below 430 km [108].

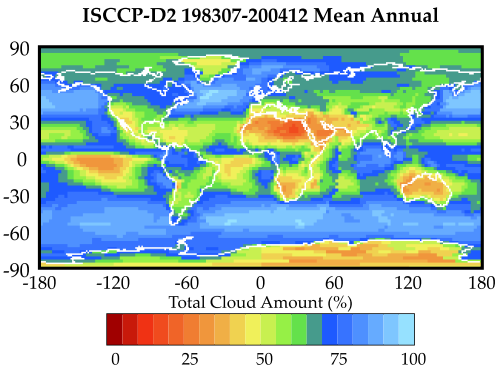

Figure 4.9: Annual Mean of the Total Clouds Cover.

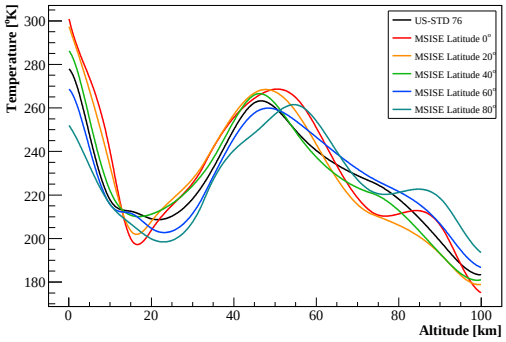

Figure 4.10: US-STD 76 and MSISE models: temperature profiles at different latitudes.

- natural night sky diffuse and slowly varying sources;
- ground sources, mainly man made sources like city lights;
- transient luminous phenomena in lower and upper atmosphere.

Natural night sky diffuse and slowly varying sources

The first category includes the whole sky stars and planets brightness, Moon phases and diffuse night sky brightness, as well as light coming from the outer space, to which contribute to the upward radiance through the Earth albedo. The so-called Airglow is the main component of the light produced in the upper atmosphere and contributes both as light directly detected and as reflected light.

Diffuse night brightness

Leaving apart the contribution due to the Moon phases, which deserves a separate treatment deeply connected with the Experimental Duty Cycle, we evaluated the diffuse night sky brightness taking the data from the "1997 reference of the night sky brightness" work [109] performed under the International Astronomical Union recommendations. For the $300 \div 400$ nm band, three main components contribute: the Zodiacal light for 100 ph·m^{-2}·sr^{-1}·ns^{-1} and the Diffuse Star Light (DSL or Faint stars) for 80 ph·m^{-2}·sr^{-1}·ns^{-1}, and the Airglow (O_2) which amounts to 300 ph·m^{-2}·sr^{-1}·ns^{-1}, as a reference value in the $250 \div 600$ nm range. The contibution of stars and planets has been estimated to be lower. Using the nomalization

to the Sun U-band, the total integrated flux of the incoming starlight on the top of the atmosphere is 190 ph·m^{-2}·sr^{-1}·ns^{-1}. The sum of the three main components of the diffuse night sky light, as mentioned above, implemented with the distinct star flux averaged over 2p (30 photons/m2/sr/ns), amounts to a total radiance (reference value) incoming above atmosphere (no moon, no planets):

$$R_{\downarrow}^{\text{diff}} = 510 \text{ ph·m}^{-2}\text{·sr}^{-1}\text{·ns}^{-1}$$

The fraction of upward reflected light depends on the transmissivity of the atmosphere and the reflectivity of the ground. The presence of clouds (with the above characteristics) should then increase the reflectivity by a factor ≈ 1.4. The above numbers are given as a guide for our estimate, but should vary according to the specific conditions. The reference value of $R_B = 510$ ph·m^{-2}·sr^{-1}·ns^{-1} turns then into a mean number of expected detected photons:

$$R^d_{B\,\text{clear}} = 200 \text{ ph·m}^{-2}\text{·sr}^{-1}\text{·ns}^{-1} \text{ in clear sky} \tag{4.5}$$

$$R^d_{B\,\text{cloudy}} = 280 \text{ ph·m}^{-2}\text{·sr}^{-1}\text{·ns}^{-1} \text{ in cloudy sky} \tag{4.6}$$

An important experimental cross check of the validity of our assumptions is given by the direct measurement done during the BABY balloon flights, expressly devoted to the measurement of the background for *EUSO*, and performed in 1998 and 2002. These flight, performed in moonless nights over the Mediterranean area, where the pollution due to human induced background canŠt be completely avoided, gave a mean value of:

$$R_B \approx 300 \text{ ph·m}^{-2}\text{·sr}^{-1}\text{·ns}^{-1} \tag{4.7}$$

at 40 km height which is fairly consistent with the previous extrapolation.

Airglow

The night Airglow is possibly the most important source of background for moonless and clear sky with no pollution light: it is an isotropic source of light located in a thin layer of upper atmosphere centred near an altitude of 100 km. It will be in direct view of the detector looking at nadir, and it will also contribute through its reflected light from atmosphere (already taken into account for in the diffuse night sky light) back. The BABY measurements, performed at an altitude of ~ 40 km, are therefore blind to its direct component. The production zone comes from the molecular oxygen

dissociation by solar radiation, the maximum production rate occurs in a thin Chapman layer located near 100 km with a few kilometres width. Once produced, the atoms encounters collisions in the mono-atomic oxygen residual gas leading to the formation of molecular oxygen witch decays via the Hertzberg transition band located mainly in the $300 \div 400$ nm band. The intensity of the emitted light depends on the solar radiation exposure, then depends on the inclination on ecliptic (season and latitude variation) and on the initial solar flux (solar cycle variation). The relaxation time of atomic collision induces a local time dependence and a longitude variation. The estimate for the mean airglow radiance prepared for the *EUSO* experiment, computed taking into account the latitueds spanned by the ISS orbit, varies $250 \div 600$ ph$\cdot$m$^{-2}\cdot$sr$^{-1}\cdot$ns^{-1} .

Total Moonless expected background

Table 4.2 summarises the expected total flux of photons, as a result of the sum of atmospheric reflected light and of the direct view of the Airglow, that we can refer to as the "steady or slowly varying sources of background".

	Incident Radiace R_b	Reflected Light Above Sea (Cloudy)	Airglow (Direct)	Background On Orbit
Minimum	460	190(260)	250	440(510)
Reference	510	200(280)	300	500(580)
Maximum	810	320(450)	600	920(1050)
BABY		300	$250 \div 500$	$550 \div 900$

Table 4.2: Reflected and Transmitted light in atmosphere

Artificial light of the night sky

We expect that city lights and gas oil extraction flares are the most important sources of artificial light of the night sky. Data were taken from nadir observation by satellites in the astronomical photometric V band in [110]. Flux data are mapped with an intensity relative to the diffuse night sky light flux, which in V band is $B_V = 860$ ph$\cdot$m$^{-2}\cdot$sr$^{-1}\cdot$ns^{-1}. The intensity ranges from 0.1 B_V (above oceans) up to values greater than 27 B_V (above the largest cities). Even if the extrapolation from V-band to U-band is not straightforward, making the assumption that the same ratio holds in

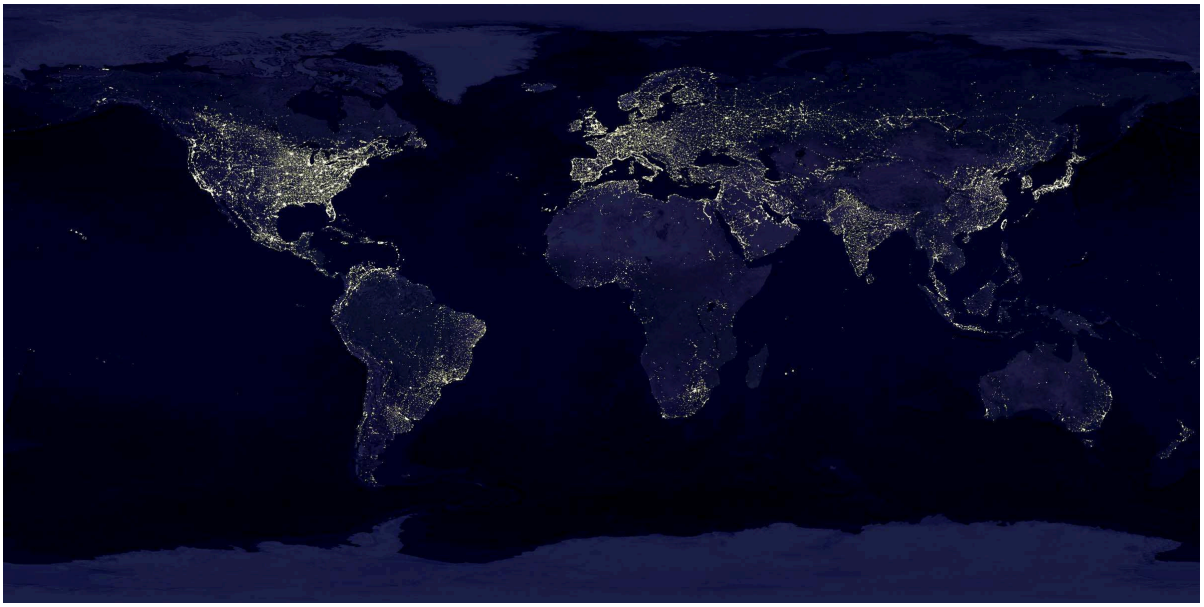

Figure 4.11: Human-made lights during the night time

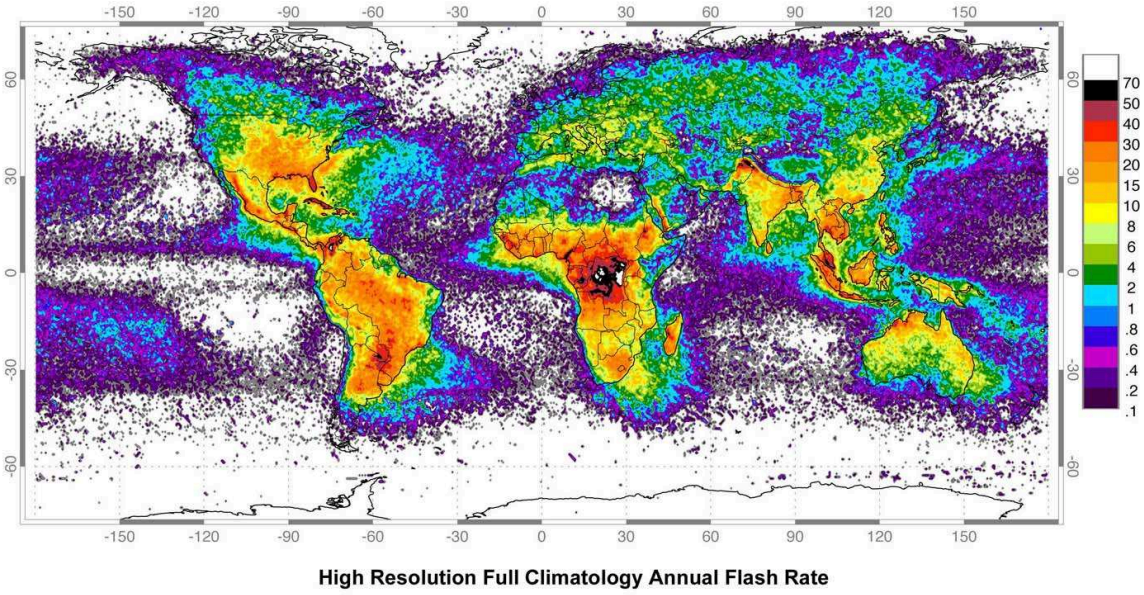

Figure 4.12: Global Distribution od lightnings, April 1995-February 2003

the *U*-map, with reference to the previously discussed reference value of 510 ph·m^{-2}·sr^{-1}·ns^{-1}, as it does in the *V*-band, we can guess the pollution level induced by the presence of the cities within our FOV.

Lightnings and transient luminous phenomena

Every second, lightning strikes the ground up to 200 times around the world with flashes occurring more frequently in the Earth's equatorial region (Fig. 4.12). Lightnings in the Earth's troposphere are among the largest impulsive energy sources within the bounds of the magnetosphere, and with 50 to 100 cloud-to-ground discharges per second globally, provide a steady source of electrodynamic excitation. Lightning effects on the magnetosphere in the form of whistler-mode waves have been recognized for decades, and whistlers are known also to cause lightning electron precipitation in the ionosphere. Recently, however, a range of spectacular and more immediate lightning effects on the lower ionosphere and the mesosphere have been discovered. These were first detected by very low frequency (VLF) radio remote sensing, which inspired studies of possible optical effects at about the same time as two fortuitous discoveries in 1989 and 1990 revealed remarkable visual evidence of direct electrodynamic coupling between lightning and the upper atmosphere. These new phenomena were soon to be called *elves*, *sprites* and *blue jets* [111].

In the elves, an electromagnetic pulse launched by a cloud-to-ground lightning stroke impinges on the lower ionosphere, is partially absorbed, and causes optical emissions between 80 and 95 km altitudes over a horizontal region several hundred km wide and over a period of about 1 ms.

Sprites consist of longer laster (up to $\sim$ 100 ms) emissions which may be highly structured and can extend from 40 to 85 km altitudes and over $\sim$ 10 km horizontally. Sprites occur in response to the intense electric fields developed in the high altitude, thin, conducting atmosphere following a major redistribution of electric charge in the troposphere, typically a positive cloud-to- ground lightning return stroke, which moves positive charge from a cloud to the Earth's surface.

Blue jets are a second high altitude optical phenomenon, distinct from sprites, observed above thunderstorms using low light television systems. As their name implies, blue jets are optical ejections from the top of the electrically active core regions of thunderstorms. Following their emergence from the top of the thundercloud, they typically propagate upward in narrow cones of about 15 degrees full width at vertical speeds of roughly 100 km/s, fanning out and disappearing at heights of about $40-50$ km.

Recent measurements

The most recent data of the night sky background from space come from the Tatiana satellite, launched in January 2005. Tatiana measured the integrated radiance in the near-UV band over an area of 250 km on ground from an orbit of 950 km inclined by 82°. The results from Tatiana agrees with the previous estimation of the background, reporting an average value of

$$R_B = 300 \div 600 \text{ ph}\cdot\text{m}^{-1}\cdot\text{ns}^{-1}\cdot\text{sr}^{-1} \tag{4.8}$$

for at least half of the lunar cycle as shown in Fig. 4.13.

The lowest measured background level was $R_B = 300$ ph·m^{-1}·ns^{-1}·sr^{-1} during flights over Siberia and the sea in moonless nights. During moon night flight the variation within the same orbit are quite intense, due to the presence of the clouds (Fig. 4.14)

Tatiana has also recorded the increase of light radiance over several major cities, as shown in Fig. 4.15.

Moreover, the satellite observed UV flashes mainly in the equatorial region of the Earth. They can be explained under the assumption that they are caused by electric discharges in regions of storm clouds, which form a separated belt in the equatorial region. Experimental data on UV flashes that do not include the spectral characteristics of fluorescence are insufficient for the final conclusions on the nature of a discharge [90].

4.4 Detector Simulation

The detector's simulation in ESAF is divided in two parts. The tracking of the photons through the inner structure of the detector, and the simulation of the electronic's response.

The main modules of the tracking engine are the optical system and the focal surface. Two optical system were implemented for the *EUSO* Phase A. A full Monte-Carlo simulation of the double Fresnel optics baseline and a multi-purpose parameterized optical system. The latter has been included to have the possibility to compare the effect of the Fresnel optics with the performances of the optical system quoted in the requirements. The parameterized optics has the secondary advantage to be configurable to match any optical system.

The focal surface module is conceived to host different focal surface layout. Two design were proposed during the *EUSO* Phase A, a cartesian layout and a polar layout (Fig. 4.16) Both have been implemented as

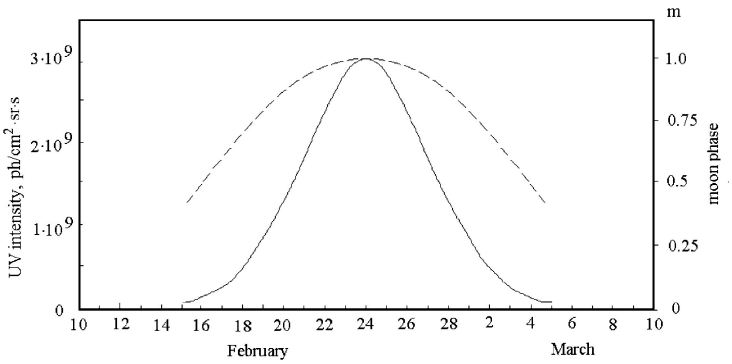

Figure 4.13: Average UV intensity (left Y-axis, solid line) and the Moon phase (right Y-axis, dashed line) during one moon month.

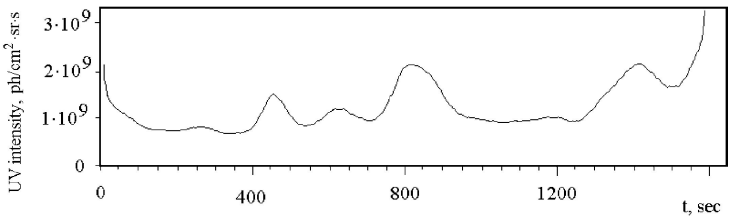

Figure 4.14: UV intensity recorded in one circulation at the full moon night side of the Earth.

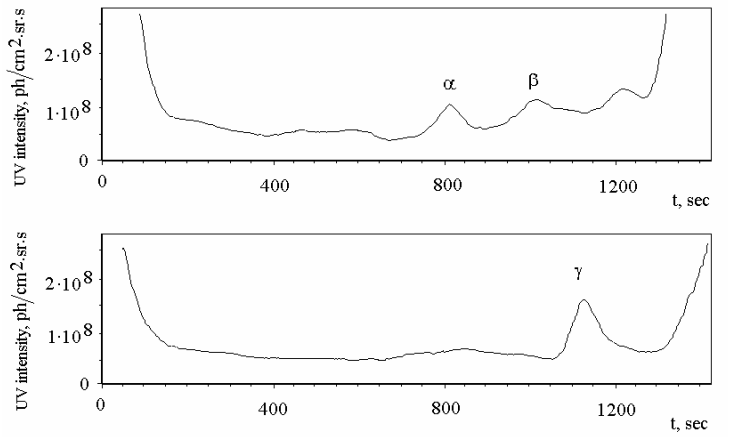

Figure 4.15: Examples of UV intensity recording at night side of the Earth. Top panelŮthe circulation, in which the satellite crosses Mexico City (α) and Houston (β). In the bottom panel the satellite crosses Los Angeles (γ).

focal surface module to compare the effect of the dead areas in the two configurations on the detector's performances.

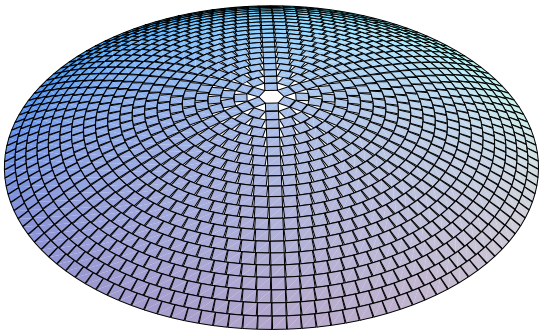

Figure 4.16: Focal Surface Polar layout.

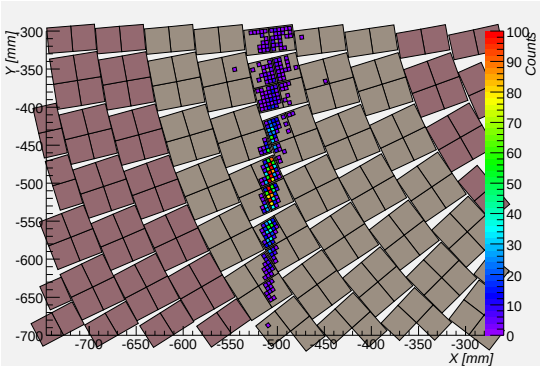

Figure 4.17: Integrated 10^{20} eV, $\theta = 75°$ shower track as appears on the FS. The large squares represent the PMTs and the small ones the pixels.

The photons reaching the EC is tracked through the optical adapter to the MAPMT's photocathode. ESAF includes several MAPMT models, which were considered as *EUSO* baseline, like the *Hamamatzu R8900* 16-pixel MAPMT, or the *Hamamatzu R7600* 64-pixel MAPMT. The PMT signals are collected and stored, waiting to be processed by the electronics.

The electronics simulation performs the second step of the detector's Monte-Carlo chain. The collected signals are ordered in time and counted according the GTU. For every channel and every GTU a random number background distributed according the intensity of the background in the channel are added to the channel count budget.

After all channels have been processed, the electronics runs the trigger over the collected samples. A multiple trigger engine was conceived to run in parallel several trigger algorithms to compare the trigger results on event-by-event basis. The trigger algorithms and the calculation of the background distribution are discussed in detail in the next chapter.

Chapter 5

Montecarlo studies

In Chapter 3 we have followed a top-down approach. From a set of scientific requirements we have inferred a set of observational/instrument requirements that could grant fair performances. Out of the requirements we have outlined a possible realization of an ideal detector. In this Chapter we will follow the opposite approach. We will use the *EUSO* design implemented in ESAF to determine the performance of a realistic detector. *EUSO* was strongly volume, mass and power limited by the accommodation on the ISS. A future mission aiming to observe UHECRs from $E \gtrsim 10^{19}$ eV will require a larger and more efficient instrument. The question is: how much the performances of the detector shall be improved? A precise answer is not easy. The detector's design is a trade-off between the scientific requirements and the Space constraints. New technological developments are involved, which outcome is not always certain. Considering the framework of the ESA Cosmic Vision program for the next decade, *EUSO* will be the reference point of any new missions for the observation of UHECR from space. Likely a new experiment will not suffer from the strict constraints of the ISS, will employ a better optical system, new high quantum efficiency photo-sensors and a different implementation of the electronics. Nevertheless, exploiting the same observational approach it will share with *EUSO* several systematics. For instance, all the issues related with the optics' aberrations, the geometrical inefficiencies, the atmosphere and the background will be present. For these reasons we have chosen to use *EUSO*, in its Phase A configuration, as a reference model for a set of simulation aiming to establish the relation between the instrument's efficiency and the detectors photo-detection power, i.e. the $\mathcal{E}_{\mathrm{PD}}$.

The study is based on the Contiguity Tracking Trigger (CTT) algorithm

developed during the Phase A. As far as concern this thesis, the algorithm has been implemented in ESAF and using ESAF its parameter has been optimized. The CTT has been the tool to compare the trigger efficiency and the trigger threshold of several *EUSO*-like detectors with different $\mathcal{E}_{\mathrm{PD}}$.

A preliminary remark is necessary: the expected number of detected UHECRs is a function of the efficiency ϵ and the energy threshold E_{th} as introduced in Sec. 3.1.1. We refer to E_{th} as the energy at which $\epsilon = 90\%$.

The efficiency ϵ is actually the product of the trigger efficiency ϵ_{tri} and the reconstruction efficiency ϵ_{R}. This distinction is motivated by the fact that the two efficiencies are influenced by different factors. While ϵ_{tri} is limited by the power and telemetry constrains in space, the reconstruction efficiency has a theoretical upper limit corresponding to the amount of information carried by the detected signal.

Similarly we have the thrigger threshold in energy $E_{\mathrm{th}}^{\mathrm{tri}}$ and the reconstruction threshold $E_{\mathrm{th}}^{\mathrm{R}}$. The overall energy threshold is approximately the lower between $E_{\mathrm{th}}^{\mathrm{tri}}$ and $E_{\mathrm{th}}^{\mathrm{R}}$.

In this Chapter we will limit our discussions to the trigger efficiency and to the trigger threshold in clear sky conditions which must not be mistaken for the real efficiency and energy threshold. The assessment of the total efficiency requires the EAS reconstruction under various atmospherical conditions and background levels. Although the ESAF reconstruction framework development stage is rather advanced, it has not reached the full maturity yet and could not be employed in our studies.

5.1 The trigger

The trigger is one of the challenging aspects of the design of a space-based observatory of UHECRs: A detector with a 30° FOV and a granularity of 0.1° has $\sim 3{\cdot}10^5$ channels that have to be analyzed with a frequency of the order of $400 \div 100$ kHz within the constrains of power and telemetry. Power and telemetry that has to be shared with the other subsystems. The general trigger requirements for a generic UHECR mission can be summarized as:

i) Efficiency: the Fake Trigger Rate (FTR) must be compatible with available telemetry. The atmosphere as a calorimeter is a very active media. The trigger must efficiently reject the uniform background but also the transient events.

ii) Rate: The high sampling rate combined with the large number of channels requires a multi-level trigger. The first level shall rapidly

filter the incoherent noise, letting the next levels to apply more sophisticate and time consuming algorithms.

iii) Power consumption: the large number of channels suggests a first level trigger integrated as much as possible with the front-end electronics.

iv) Adaptability: the background varies over the FS on local and global scale. The background varies continuously according the atmospheric conditions and the background sources in the FOV. The trigger must be able to quickly adapt its thresholds to the current background rate.

From the *EUSO* experience, a possible implementation of the multi-level trigger structure could be:

1. A first trigger level operating at the single EC to select the signal candidate according to elementary properties, like the intensity or the contiguity between pixels.

2. A second level trigger that performs a track fitting and rejects the events which do not show the correct space and time kinematics. This trigger could operate on neighboring EC or at MacroCell level. Since the fit requires much more time than the intensity/contiguity, the second level must operate at much lower rate.

3. An optional third level could connect pieces of track on different MacroCells whenever necessary or apply further cuts according to the shape and duration of the signal.

The design of the trigger chain cannot be performed without the technical details of the mission and is one of the issues typically addressed during the Phase A and Phase B. However, in the view of a possible Cosmic Vision mission, the scheme that has been studied during the *EUSO* phase A can be applied and provide significant information on the performances of a future mission. In particular, the algorithm developed as a first level trigger, the Contiguity Tracking Trigger, is well suited for the studies of the trigger threshold. The algorithms exploits the space and time contiguity between neighboring pixels to identify possible track candidates. As the contiguity is one of the basic requirements to detect the EAS signal, the results obtained can be applied to detector which have similar instrument requirements.

5.1.1 The simulated configuration

All the simulations used in the discussion are based on a standard configuration which derives from the *EUSO* Phase A design. From the base configuration 4 similar detectors have been implemented. They are identical, actually the same detector, but for the size. The smaller detector is *EUSO*, 2.5 m diameter. The others are 4 m, 8 m and 12 m diameter wide corresponding to a larger collection area by a factor 2.56, 10 and 23 times respectively. A larger collection area implies a larger number of signal and background photons, therefore in the electronics simulation the background rate is increases according to the scale factor of the detector.

In the simulation of the FTR and the triggers The main components are summarized here for future reference.

- Event generator: Unisim.
- Atmosphere: US-STD, Clear Sky
- Detector simulation: *EUSO* Phase A
  - Optical System: Parameterized optics with 2D gaussian Point Spread Function (PSF) of 5 mm RMS.
  - Counting electronics. For detectors larger than *EUSO* the amount of collected light could be not suitable for a counting digital electronics. In counting mode an increase of the expected number of photons by a factor A should be compensated by a reduction of the electronic's dead time by a factor $1/A$. From the trigger's point of view the effect is marginal and doen't affect the result. It becomes not negligible instead in the Energy reconstruction algorithms.

5.1.2 The EAS signal

Here we briefly summarize the most relevant features of the EAS signals from the detection and reconstruction point of view of a Space experiment. The signal appears as a luminous spot on the focal surface becoming brighter up to the maximum and then gradually diminishing. The profile of the luminosity vs. time is bell-shaped and its amplitude and width depend mainly on the primary cosmic rays energy, on the zenith angle and on the interaction altitude in the atmosphere. In detail, for fixed the atmospheric conditions:

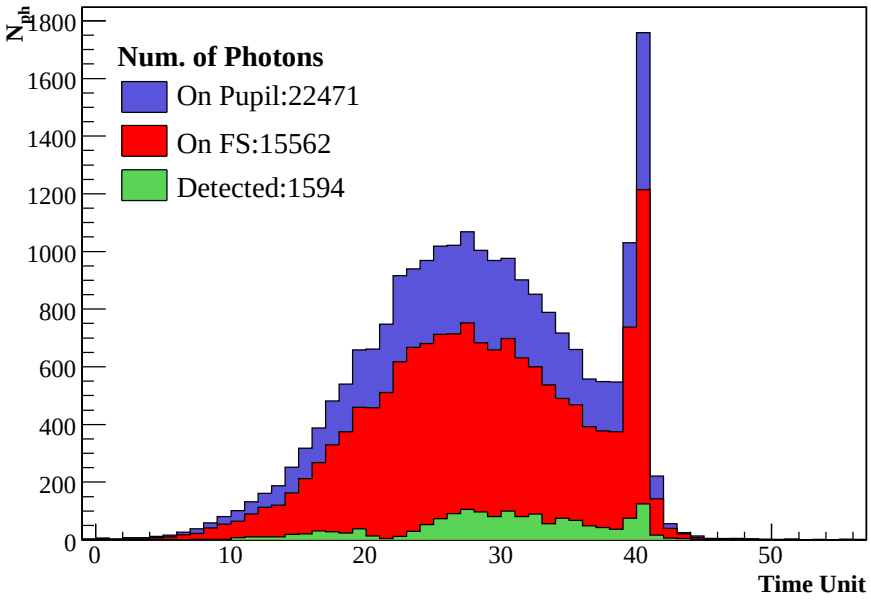

(a) $E = 10^{20}$ eV, $\theta = 45°$.

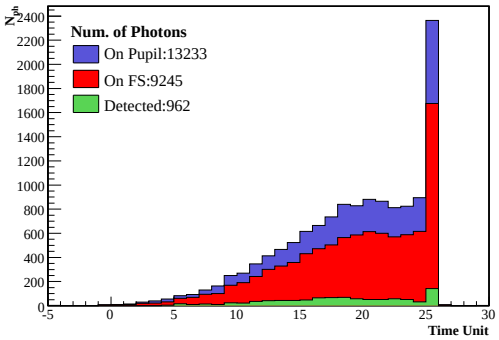

(b) $E = 10^{20}$ eV, $\theta = 15°$.

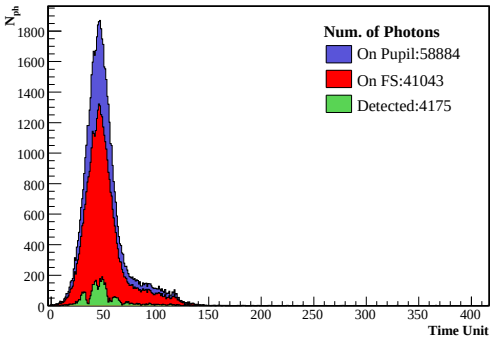

(c) $E = 10^{20}$ eV, $\theta = 75°$.

Figure 5.1: Number of photons reaching the pupil of a 4 m diameter detector for a $E = 10^{20}$ eV shower in clear sky at three different values of $\theta = 15°, 45°, 75°$. The blue histograms refer to the photons reaching the pupil, the red to the photons the focal surface and the green one to the photons which have generated a signal in one of the PMTs. The Cherenkov peak is present in the showers at $\gamma = 15°$ and 45°. The profiles of detected photons have several dips due to the dead areas on the focal surface.

- The number of photons in the track N_{ph} is directly proportional to the energy of the primary.
- At higher altitude, where the atmosphere is thinner several contribution increase the luminosity of the shower. Developing into a the less dense atmosphere, the EAS grows long due to the relation between the X and ℓ, $\frac{\mathrm{d}X}{\mathrm{d}\ell} = \rho$. On the other hand the fluorescence yield is almost constant between 0 and 20 km. N_{ph} is expected to grow proportionally to the length of the shower. On the contrary, the peak of photons depends weakly on the altitude, therefore the ratio between the length of the shower and the number of photons in the maximum $N_{\mathrm{ph}}^{\mathrm{max}}$ is an indicator of altitude of h_{max} [112].
- On average, the first interaction and the EAS maximum take place at higher altitude as the zenith angle increases (see Fig. 3.4). N_{ph} increases as explained in the previous point. In Fig. 5.1 are shown 3 EAS luminosity profiles at different zenith angles.

During the conversion from photons to photo-electron counts in the electronics, the signal suffers from three types of losses:

- an overall attenuation due to the absorption in the optics or the quantum efficiency of the photo-sensor,
- the blurring of the spot on the focal surface due to aberration of the optics,
- the geometrical inefficiencies of the focal plane.

While the former two effects degrade the time profile uniformly, the latter alters the shape of the profile. The geometrical losses must be taken properly into account when using the signal profile to infer the UHECR energy. A typical shower image on the FS is shown in Fig. 5.2. The image has been built summing all the signal counts up. The intensity peak (the red pixel) in the center of the image does not necessarily correspond to the maximum of the longitudinal profile because it's the sum of counts taken in different GTUs.

An example of the number of counts generated by the shower signal in the electronics is shown in Fig. 5.4, where for each GTU the maximum number of counts per pixel is plotted. The showers which extend over more than one EC have the chance to present a dip when the spot falls in the dead area between the EC. The probability of such event and the depth of the dip depend on the sharpness of the PSF and on the geometrical layout of the focal surface.

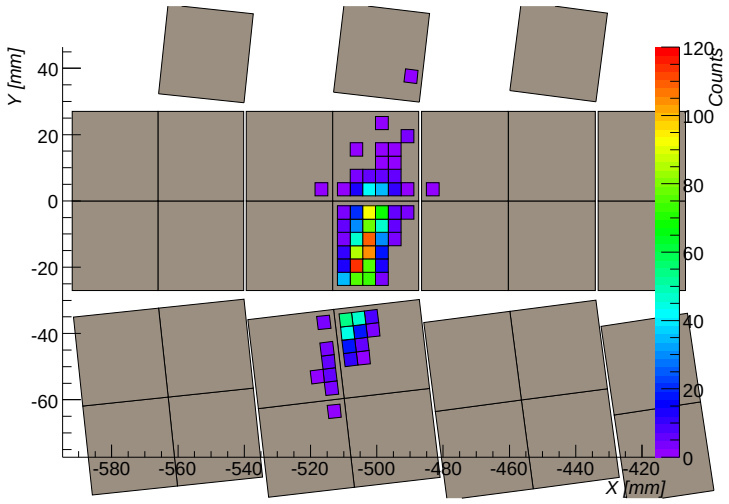

Figure 5.2: Image of the $E = 10^{20}$ eV, $\theta = 45°$ shower on the FS. The image is the sum of all the signal counts collected in all GTUs of the development of the signal. The light brown squares are the PMTs, grouped in ECs. The small colored squares are the PMTs' pixels which has collected at least one signal photon.

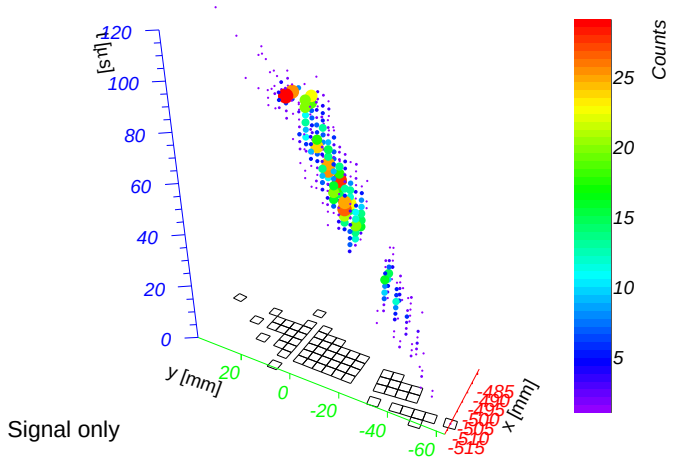

Figure 5.3: The 3D image of the $E = 10^{20}$ eV, $\theta = 45°$ shower. the points represent the counts in a pixel at time t. The x and y axis are the xy coordinates of the pixels while the z axis is the time from the first signal photon counted. On the xy-plane is plotted the profile of the pixels with signal.

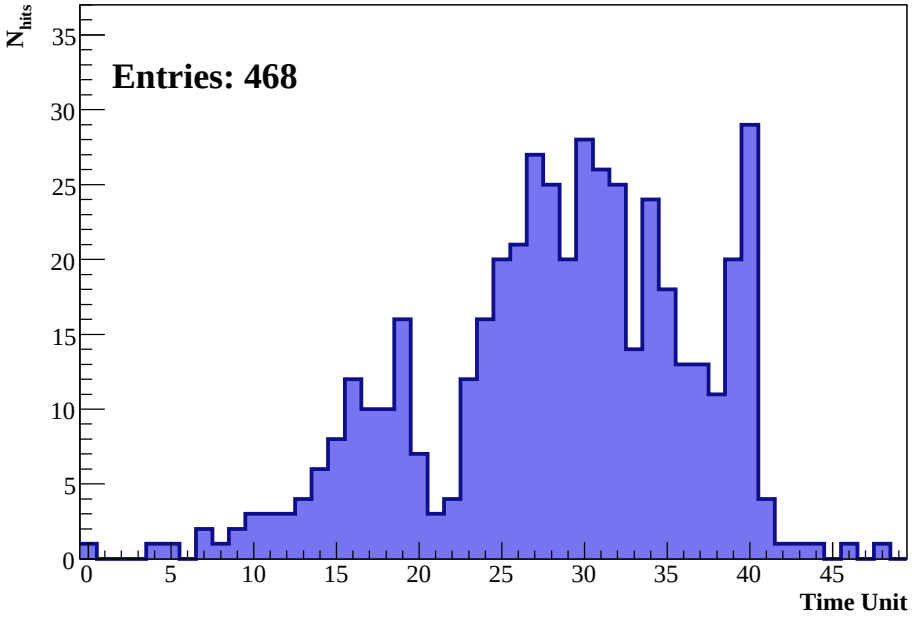

(a) $E = 10^{20}$ eV, $\theta = 45°$.

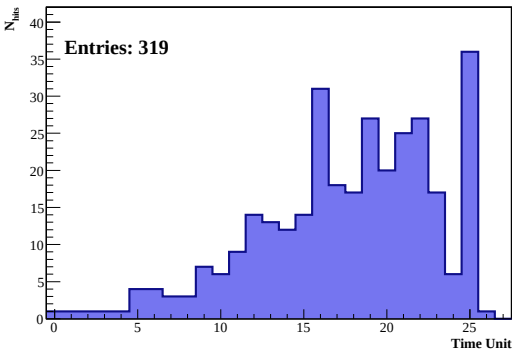

(b) $E = 10^{20}$ eV, $\theta = 15°$.

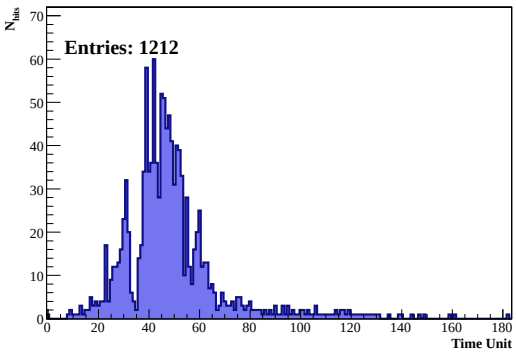

(c) $E = 10^{20}$ eV, $\theta = 75°$.

Figure 5.4: Counting profiles of the EAS of Fig. 5.1 as detected by the instrument (4 m diameter detector, 2.5 μs GTU). For every GTU is plotted the maximum number of signals counted N^{hits} in a pixel in the GTU. Compared to the plots of Fig. 5.1 the counting profiles present some differences: i) the dips corresponding to the dead areas and ii) the reduction of the Cherenkov beam due to the saturation of the electronics.

5.1.3 The background

The expected background on the focal surface is expressed as the background counting rate per pixel ν_B. The background rate ν_B is a function of the incoming background radiance on the entrance pupil B, of the optical efficacy $\mathcal{E}_{opt}$, of the photo-sensor's photo-detection efficacy ε_{PD} and the angular resolution δ:

$$\nu_B(\gamma) = B \cdot \delta^2 \cdot \varepsilon_{PD} \cdot \mathcal{E}^{tri}_{opt}(\gamma) \tag{5.1}$$

In our simulations we have used the background radiance reference value at the entrance pupil: $B = 500$ ph·m^{-2}·ns^{-1}·sr^{-1}, uniform and constant. The equation (5.1) is a exact in case of an ideal optics without aberrations that focus all the photons from an incident direction in a 0-size spot. The aberrations of a real optics, especially for a Fresnel optical system like the *EUSO* baseline, give a relevant contribution to the distribution of the background. At large incident angle the PSF becomes strongly uneven spreading a fraction of the photons all over the focal surface. In particular, in Fig. 5.5b is plotted a PSF corresponding to an incident angle $\gamma = 25°$ along with a red circle approximately representing the size of the pixel. A large photon's fraction cannot be contained in a single pixel. Moreover, in Fig. 5.5b is plotted the distribution of photons on the rest of the FS. Even though the photons are mainly focused in the spot the red arrow points to, there is a large contribution on the rest of the FS, the so called stray light. To compute the ν_B distribution over the whole FS, the distributions of all incident direction must be summed up and the stray light cannot be neglected.

The photon's density $\rho_B(\vec{x}_{px})$ on the FS has been obtained simulating several million of photons with an uniform incident angles distribution, according to the estimated background distribution. The result, as a function of the distance from the center of the FS is shown in Fig 5.6.

The number of counts of 5.6a have been calculated for a 4 m diameter detector according

$$\nu_B(\vec{x}) = \rho_B(\vec{x}_{px}) \cdot \varepsilon_{PD} \cdot d^2 \tag{5.2}$$

where ρ_B is the number of background photons per mm^2, $\vec{x}_{px}$ is the position of pixel on the FS and d is the pixel's side.

For our studies we have simulated $3{\cdot}10^5$ proton showers in the energy range 10^{19} eV $< E < 5{\cdot}10^{20}$ eV. The starting point for the development of a trigger algorithm is the signal-background behavior in the events under study. To check the behavior of the signal as a function of the energy and the zenith angle, we have plotted in Fig. 5.7 the total number of counts

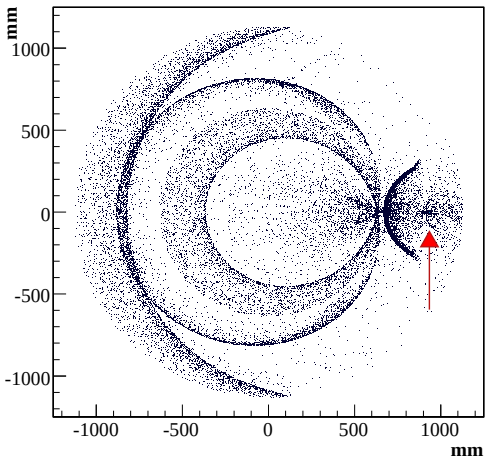

(a) Distribution of photons on the focal surface produced by an uniform flux of incident photons with angle $\gamma = 25°$. The red arrow points to the position of the spot.

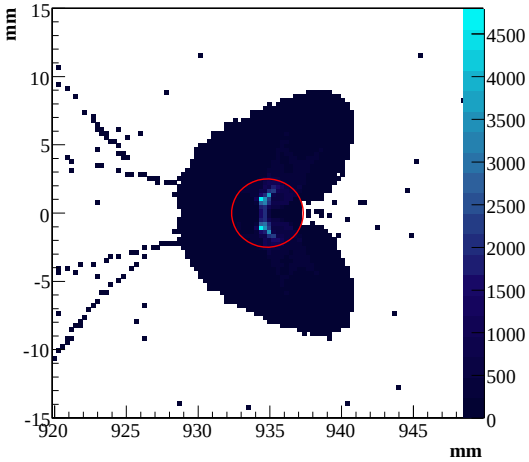

(b) Zoom on the spot of the previous picture. The red circle corresponds to the 5 mm bucket used in the definition of the $\mathcal{E}_{\text{opt}}^{\text{tri}}$ which is also the pixel size.

Figure 5.5: An example of the irregular PSF of the Fresnel optics generated using an incident flux at $\gamma = 25°$.

$N_{\text{tot}}^{\text{cnt}}$ and the maximum counts in one GTU and one pixel $N_{\text{max}}^{\text{cnt}}$ for the showers in our sample. The graphs have been produced for three reference energies, $E = 5{\cdot}10^{19}$ eV, 10^{20} eV and 10^{20} eV using a 4 m diameter, 2.5 μs GTU detector. In the left column $N_{\text{tot}}^{\text{cnt}}$ is plotted vs. θ. At large zenith angle the expected elongation of the EAS image corresponds to an increase of $N_{\text{tot}}^{\text{cnt}}$; the number background counts increases accordingly as the image is distributed over a larger number of pixels. At $E = 5{\cdot}10^{20}$ eV, the curve is flattened for $\theta \gtrsim 70°$ because near to the shower maximum the signal is so strong that the average time separation of two photons become less than the 10 ns double hit resolution of the electronics.

Supposing to perform a perfect signal identification, i.e. select all and only the pixels which have at least one signal, the blue distribution represent the amount of background that would be collected with the signal. At $E \gtrsim 10^{20}$ eV (Fig. 5.7c) the signal equals, on average, the background in the shower image.

The larger photons' fraction is concentrated around the maximum. On the right column of Fig. 5.7, the maximum number of counts $N_{\text{max}}^{\text{cnt}}$, signal plus background, is compared to the maximum background counts in the same EC. Vertical showers at $5{\cdot}10^{19}$ eV, the number of signal photoelec-

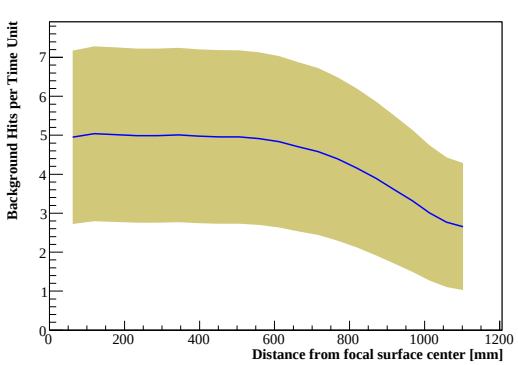

(a) Background rate (Counts per GTU) of a 4 m diameter detector and a 2.5 m GTU as a function of the distance from the center of the FS. The beige band is 1 σ wide.

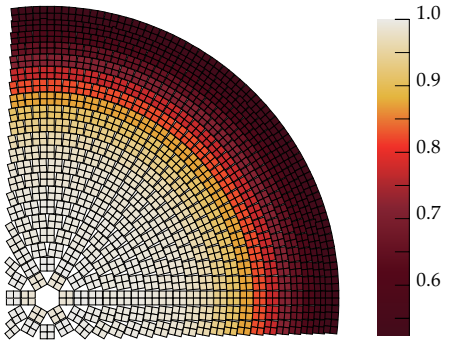

(b) Relative distribution of background photons on the focal surface.

Figure 5.6: Background on the focal surface generated by an uniform radiance.

trons counted in the maximum is of the same order of the background fluctuations. At larger θ, $N_{\max}^{\text{cnt}}$ rises above surrounding background by a factor $\sim 2 \div 3$. In this situation, where the maximum is of the same order of magnitude of the background, the detection of the shower's track is problematic. The situation changes at higher energies where the intensity of the maximum is at least twice than the maximum of the surrounding noise. In this case the shower signal produces a track of pixel brighter than the background that carries the information of the EAS.

5.2 The Contiguity Tracking Trigger

We have developed a first level CTT to fulfill the strict constrains of the *EUSO* mission on the ISS. The algorithm exploits the elementary properties of the EAS signal over an incoherent background, the time and space contiguity. An important features of this trigger scheme is the possibility to be integrated in the EC's front-end chip with the combinatory logic. The advantages are the low power consumption and the absence of dead areas within the EC, a fact that contributes to keep the trigger scheme simple, from the conceptual and implementation point of view.

Using the *EUSO* configuration, we remind that the EC is a 2×2 array of PMT installed on a PCB. Every EC is a 12×12 matrix of pixels. On the back side of the PCB is installed a front-end chip. The chip digitizes the signal and counts the number of signals in a GTU.

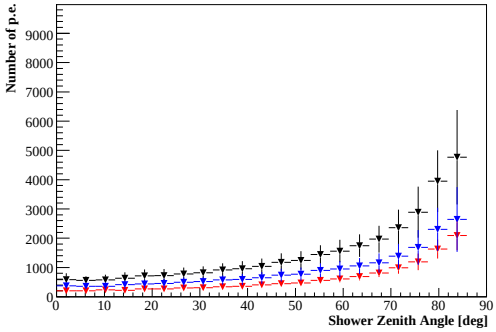

(a) N^{cnt}_{tot} vs. θ at $E = 5{\cdot}10^{19}$ eV.

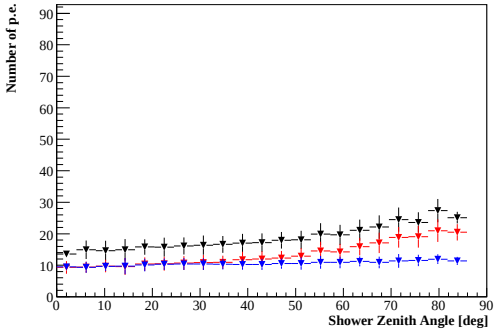

(b) N^{cnt}_{max} vs. θ at $E = 5{\cdot}10^{19}$ eV.

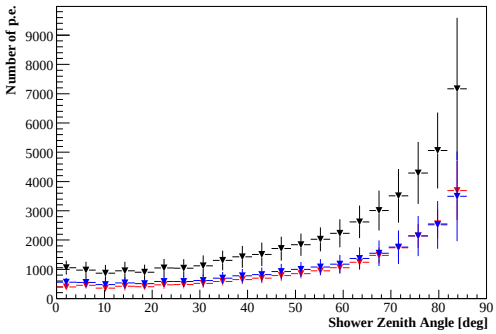

(c) N^{cnt}_{tot} vs. θ at $E = 10^{20}$ eV.

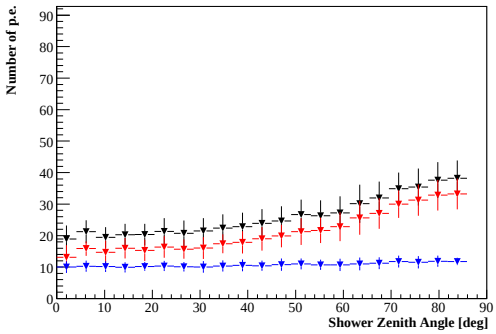

(d) N^{cnt}_{max} vs. θ at $E = 10^{20}$ eV.

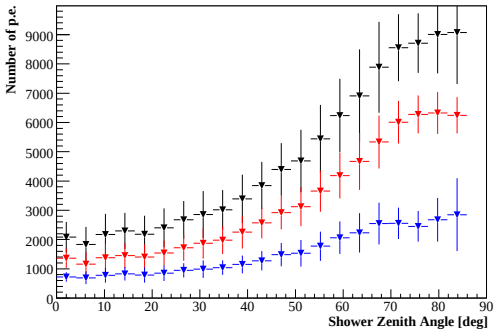

(e) N^{cnt}_{tot} vs. θ at $E = 5{\cdot}10^{20}$ eV.

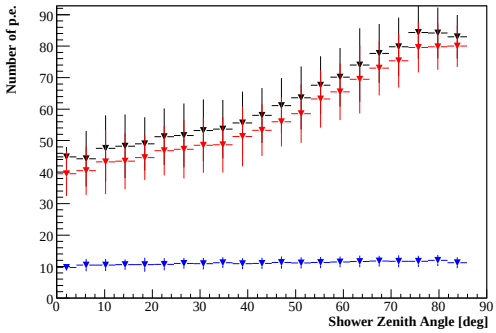

(f) N^{cnt}_{max} vs. θ at $E = 5{\cdot}10^{20}$ eV.

Figure 5.7: Signal (red), background (blue) and signal+background (black) for 3 shower samples as detected by a 4 m, 2.5 μs GTU detector. (a) and (b) $E = 5{\cdot}10^{19}$ eV, (c) and (d) $E = 10^{20}$ eV, (e) and (f) $E = 5{\cdot}10^{20}$ eV. On the left the total number of counts N^{cnt} in the EAS development; only the pixels which have at least one signal count are considered. On the right is shown the maximum number of PMT counts in one pixel and in one GTU N^{cnt}_{max} (black). In red the number signal counts in the maximum and in blue the maximum number of background counts in the same EC and GTU where N^{cnt}_{max} has been recorded. Only the background counts in the pixels with signals have been taken in accounts for the background plots (blue).

The main idea is simple. We require that a bright spot is detected for L times and that each pixel has a position that is kinematically compatible with the previous one, i.e. at each GTU the pixel trigger must occur in the same position or in as adjacent position of the previous one.

Digital threshold

A "bright spot", or active pixel, is defined as a pixel that, in one GTU, counts a number of signals above a threshold T. The threshold must take into account that the average background rate varies with the position on the FS and in time, even if on a time scale much longer than the EAS development.

We have parameterized T as follows

$$T = n_{\mathrm{B}} + k\sqrt{n_{\mathrm{B}}} \tag{5.3}$$

where n_{B} is the mean number of background counts per time unit in the pixel and k a real number (usually an integer). Since the background is poissonian, for large values of n_{B}, k assumes the meaning of the number of sigmas. This parameterization that uses the local background rate is intrinsically adaptable. From the implementation point of view: fixed k, n_{B} can be continuously measured by the front-end and T updated accordingly.

An example of the active pixels above the threshold in the MacroCell where the signal of a 10^{20} eV EAS is detected is shown in Fig. 5.8. Four different thresholds have been applied to the background+signal counts. At $k = 1$ and 2 the number of randomly activated pixels is large and so the chance of a random contiguity.

Contiguity algorithms

At each GTU, each pixel can be above or below the digital threshold, i.e. cab be active or not. We define $\vec{x_i}$ a boolean array of dimension $N = 144$, whose n^{th} component is 1 if, at the i^{th} GTU, the channel n is active, 0 otherwise. In other words, $\vec{x_i}$ indicates the active channels of the i^{th} GTU.

Let $\varphi(\vec{x})$ an operator that for a given $\vec{x}$ returns another vector that has all nearest neighbors of the channel active in $\vec{x}$, i.e. the k^{th} component of $\varphi(\vec{x})$ is 1 if k is a nearest neighbor of an active component of $\varphi(\vec{x})$. There is a matrix A that gives:

$$\varphi(\vec{x}) = A \cdot \vec{x} \tag{5.4}$$

A is a squared matrix of boolean elements. Being a linear boolean operation, the operation $A \cdot \vec{x}$ can be implemented with a purely combinatorial circuit.

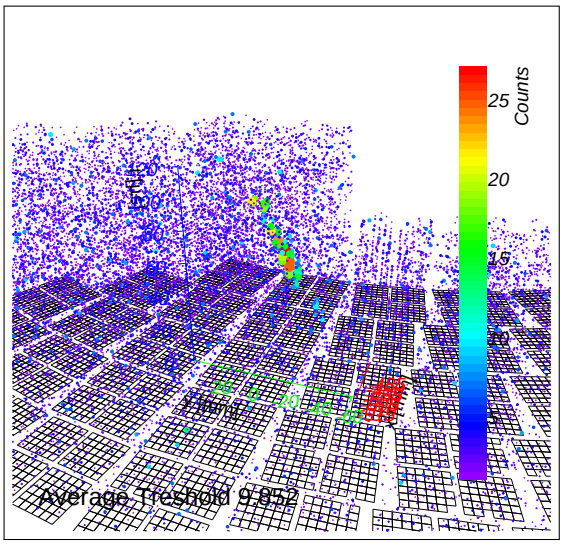

(a) $k = 1$.

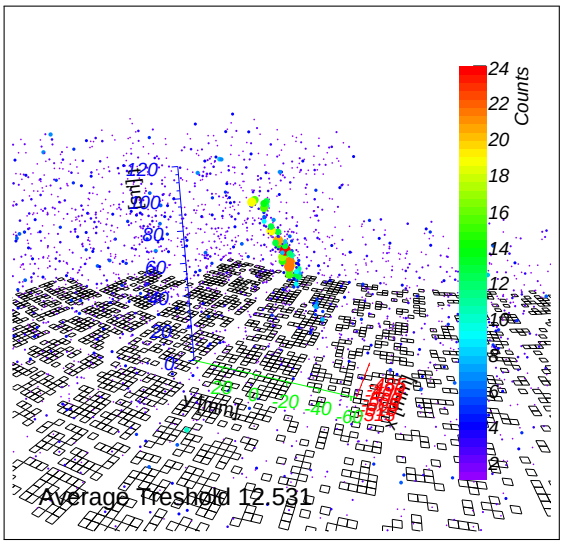

(b) $k = 2$.

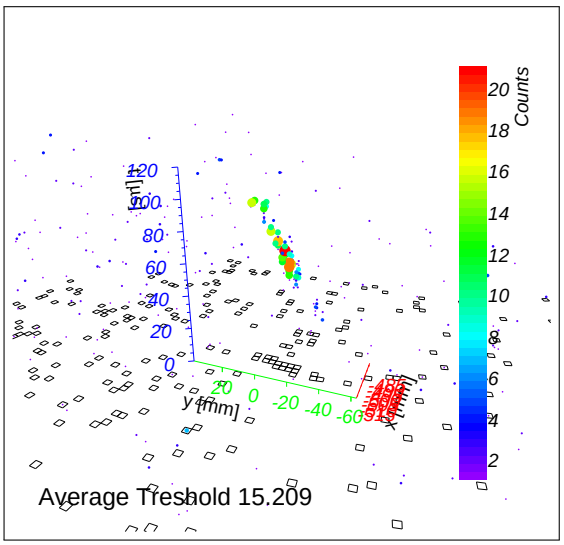

(c) $k = 3$.

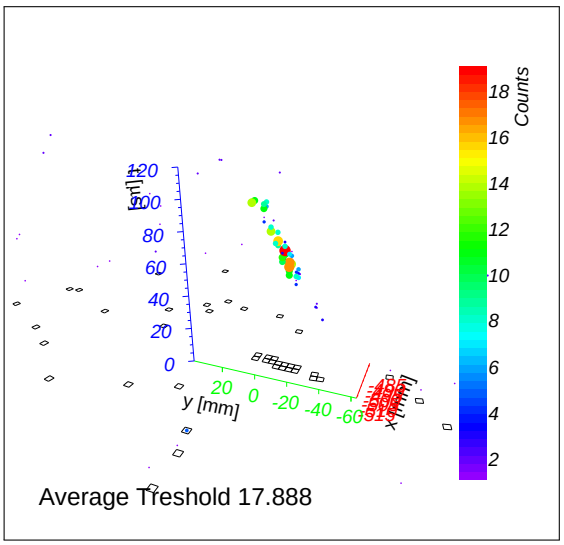

(d) $k = 4$.

Figure 5.8: Four plots of the active pixels in a MacroCell on the FS for a $E = 10^{20}$ eV, $\theta = 45°$ EAS after the thresholds: $k = 1, 2, 3$ and 4.

Let us now consider two consecutive GTUs that we call TU1 and TU2. The two boolean state vectors $\vec{x_1}$ and $\vec{x_2}$ that describe which pixel were active. The condition that there is persistency and that there is at least one active pixel of TU1 that is a nearest neighbor of one pixel active in TU2 can be formally stated as follows:

$$C_2 = \vec{x_1} \star \varphi(\vec{x_2}) \tag{5.5}$$

where the $\star$ is a "scalar product" in boolean sense (each component of the vector is AND-ed with the corresponding component of the other vector and all N results OR-ed together). It is then obvious to generalize. Requiring a track of L elements is equivalent to asking that the variable:

$$C_L = \prod_{j=1}^{L} \vec{x_j} \star \varphi(\vec{x}_{j+1}) \tag{5.6}$$

where the product is considered as a normal boolean operation (AND). The logical operation described above can be implemented at ASIC level using purely combinatorial circuits.

The algorithm does not perform a real track fitting. The contiguity considers a temporal sequence of contiguous active pixels as a valid track even if they are not aligned. Therefore L does not represent the track length but the duration of the cluster of contiguous pixels. However, in the following we will refer to L as an generalized track length.

Summarizing, two parameters of the CTT define the trigger condition, the minimum track length L and the digital threshold k. We will identify the trigger configurations using the convention $[L;k]$.

The CTT has been implemented in ESAF. The code has the capability to run in parallel the trigger algorithm using a range of L. This feature becomes important to save CPU time in the trigger optimization, FTR simulation and simulation of the events.

5.2.1 Fake trigger rate

L and k have to be tuned to satisfy the requirement on the first level trigger rate $\lesssim 100$ Hz on the whole FS.

The FTR for one EC can be computed assuming the background poissonian. We define $P(n_B;T)$ the poissonian probability for a pixel to count more that T in one GTU, when the average number of background counts

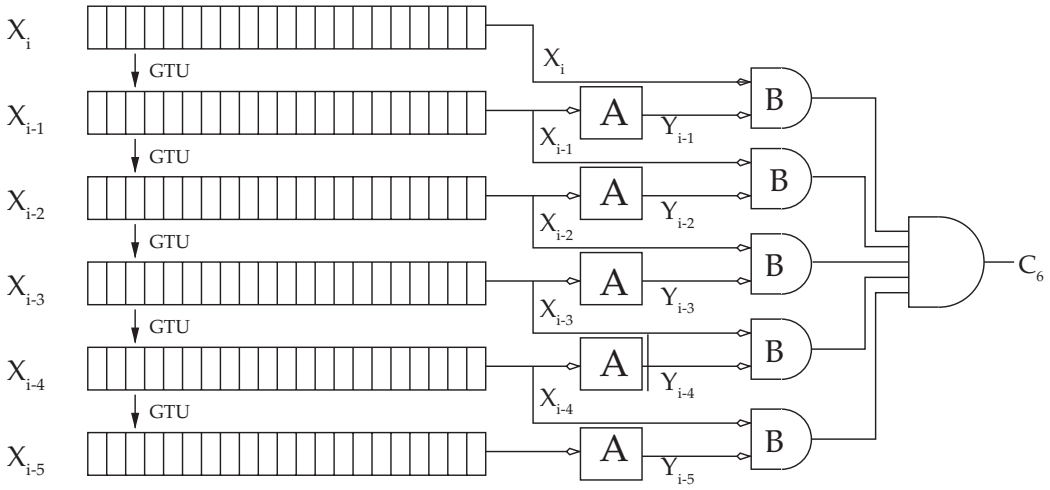

Figure 5.9: Block diagram of a possible implementation of the contiguity trigger at the level of the front end ASIC. Its detailed functions are described in the text. The block indicated with the letter A is a logic block that implements the operator φ. The block indicated by B is the boolean scalar product of vectors. The figure shows the contiguity trigger with tracks of length $L = 6$ but L can be made programmable by means of properly designed bit masks.

is n_{B}

$$P(n_{\mathrm{B}};T) := 1 - \sum_{i}^{T-1} \frac{e^{-n_{\mathrm{B}}} n_{\mathrm{B}}^{i}}{i!} \tag{5.7}$$

(5.8)

In all GTUs after the first one, the probability that the random background activates a pixel Nearest Neighbor to one pixel hit in the previous GTU is $\approx 9 \cdot P(n_{\mathrm{B}};T)$, neglecting the border effects. It follows that the probability that in a EC, during the n$^{\mathrm{th}}$ GTU the active pixels in the previous L GTUs has formed a track is

$$P(L;n_{\mathrm{B}};T) \approx 9^{L-1}[P(n_{\mathrm{B}};T)]^{L}. \tag{5.9}$$

The eq.(5.9) gives the fake trigger probability with a good approximation under the condition that a $L = 2$ track is a rare event $9 \cdot P(2,n_{\mathrm{B}};T) \ll 1$. In any case, a high probability of $L = 2$ tracks corresponds to a regime where the contiguity becomes useless to reject the noise. The eq.(5.9) has

		[L;k]					
D	n_B	[3;3]	[5,3]	[6;3]	[3;4]	[4;4]	[5;4]
2.5 m	2.0	$2.39{\cdot}10^{5}$	$2.34{\cdot}10^{3}$	232	40.8	0.22	$1.2{\cdot}10^{-3}$
4 m	5.2	$2.93{\cdot}10^{4}$	70.9	3.5	61.6	0.39	$2.4{\cdot}10^{-3}$
8 m	20	$3.54{\cdot}10^{3}$	2.09	$5.1{\cdot}10^{-2}$	1.87	$3.7{\cdot}10^{-3}$	$7.2{\cdot}10^{-6}$
12 m	46	$1.40{\cdot}10^{3}$	0.45	$8.0{\cdot}10^{-3}$	0.38	$4.4{\cdot}10^{-4}$	$5.0{\cdot}10^{-7}$

Table 5.1: FTR (in Hz) for the simulated detectors for some trigger patterns. The average number of background counts per pixel per GTU is reported as well. Highlighted in orange the configuration with a FTR exceeding 100 Hz. In green the configuration satisfing the requirement for all the detectors.

been verified simulating ~ 10 s of pure background in ESAF, equivalent to $\approx 4{\cdot}10^{6}$ GTUs. The fake trigger simulation has been performed for all the four detector configurations.

The overall fake is calculated as

$$\nu_{FTR} = \frac{N_{EC} \cdot P(L; n_B; T)}{\tau} \tag{5.10}$$

where N_{EC} is the number of elementary cells and τ the GTU's length.

In Tab. 5.1 are reported some FTR as a function of the trigger pattern for the different detectors. Even if k is not a priori an integer number we consider integer values of k, because of the long computing time required by the FTR and the efficiency simulations. In general an increase of k appears more effective than an increase of L from the point of view of the noise rejection. Another reason to favor an high k is that at low energies the EAS development is contains in few pixels. A large value of L would reject the low energy, small θ showers not because they are not bright enough to stand out against the noise but because they're not long enough.

Among the considered trigger patterns the one with the less strict requirements on the track length and $\nu_{FTR} < 100$ Hz is the [3;4]. On the other side, [3;4] is the pattern for which all the detectors are above the requirements.

To compare the trigger thresholds as a function of the detector's diameter on the same ground we want use the same trigger pattern. All the patterns starting from [3;4] up satisfy the FTR requirements.

5.2.2 The trigger efficiency

We have simulated the trigger response on a sample of 30000 proton EAS in clear sky atmosphere, with a flat energy distribution in logarithmic scale, i.e. $J(E) \propto E^{-1}$, in the energy range 10^{19} eV $< E < 5{\cdot}10^{20}$ eV and $\cos\theta$ angular distribution.

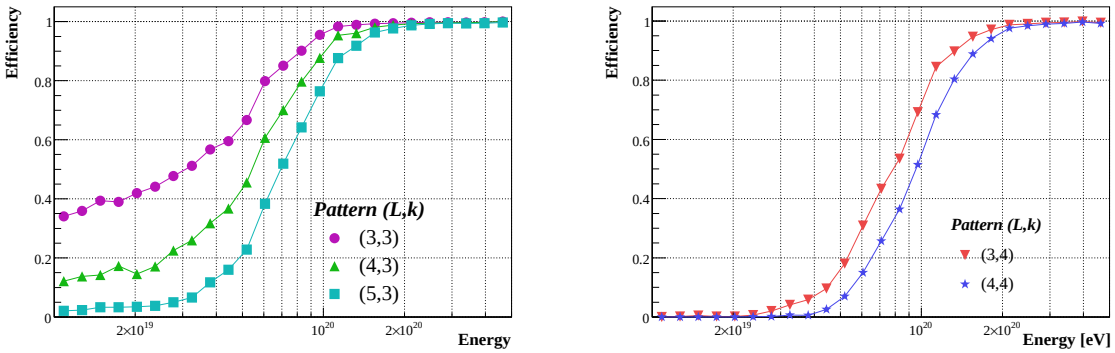

(a) (b)

Figure 5.10: The trigger efficiency for patterns with FTR above 100 Hz (a) and below 100 Hz (b).

From the previous considerations, the trigger efficiency in clear sky shall be 0 at 10^{19} eV and reach the plateau of full efficiency at high energies. In Fig. 5.10 are plotted two sets of patterns obtained with the 4 m detector. In the former (a) the FTR is not satisfied and there is a long tail of the efficiency at low energies. The tail depends weakly on the energy and flattens at low energies to a value depending on the pattern. The presence of this feature is not compatible with EAS induced triggers, which at those energies are too faint to be distinguished from the noise. In the in the latter (b) the efficiency has the correct behavior.

Another feature which is expected by the trigger efficiency curve is the dependence on the EAS zenith angle. As discussed in Chapter 3 and in the previous sections, the more inclined the EAS, the brighter the signal appears on the FS. The is shown in Fig. 5.11 where the efficiency of [3;4] and [4;4] for three subsamples of events at different θ. Compared to the full sample of events, the efficiency curve is shifted toward higher energies for $\theta < 30°$ and toward lower energies for $\theta > 60°$.

Concerning the behavior of the efficiency curve as a function of L and k, we simulated several patter triggers:

- $k = 3, 4, 5, 6$;

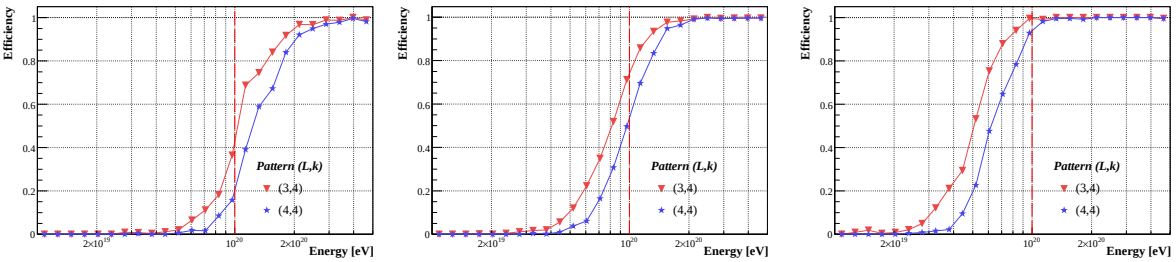

(a) $\theta < 30°$. (b) $30° < \theta < 60°$. (c) $\theta > 60°$.

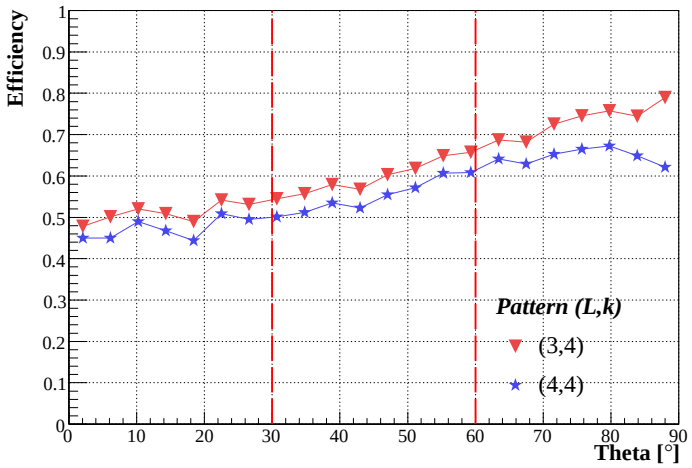

(d)

Figure 5.11: Trigger efficiency of the [3;4] and [4;4] patterns on three ranges in θ. The relative weight of the three samples are (a) ≈ 25%, (b) ≈ 50%, (c)≈ 25%. The red line at 10^{20} eV is drawn as a reference. In (d) the trigger efficiency is plotted vs. the EAS zenith angle for 10^{19} eV < E < $5{\cdot}10^{20}$ eV.

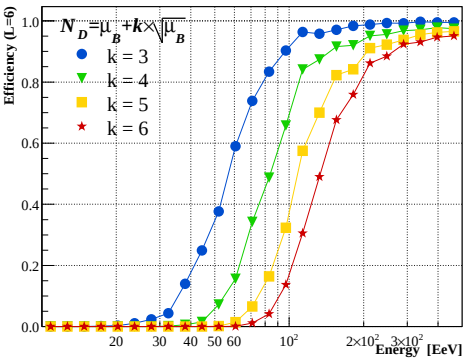

(a) Shift of the energy trigger threshold as a function of the digital threshold at fixed $L = 6$ ($k = 3, 4, 5, 6$).

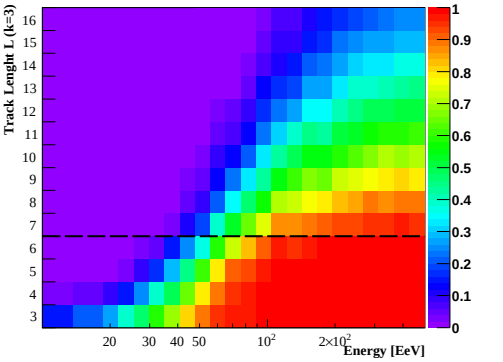

(b) Shift of the energy trigger threshold as a function of the track length at fixed $k = 3$ ($L = 3 \div 16$). The dashed line separates the patterns that reach $\epsilon = 1$ at full trigger efficiency ($L = 3, 4, 5, 6$).

Figure 5.12: Study of the trigger threshold with the 4 m diameter detector.

- $3 \leq L \leq 16$.

An example of the behavior of the trigger efficiency as a function of k keeping L constant is shown in Fig. 5.12a. The net result is again a shift of the curve toward higher energies without a change in shape. The high energies plateau remains at $\epsilon = 1$. The situation is different when the minimum track length L increases keeping k constant: at large L the plateau decreases below the full efficiency. Two effects are responsible for the lost events. The primary reason is the time length of the shower signal, or, to be more accurate, of the part of the shower which is bright enough to stand over the noise. Vertical showers are shortened by the impact with the ground and the signal may result too short. An example is shown in Fig. 5.12b. Patterns with $L > 6$ do not reach the full efficiency even at $5{\cdot}10^{20}$ eV. A secondary reason which affects longer showers is that tracks which have a length compatible with the EC size can be split in two segments. If none of the segment is as long as L ore more, the trigger is not issued. In Fig. 5.12b is plainly visible that if $L > 12$ the efficiency plateau is lower than 12%.

5.3 Energy threshold as a function of $\mathcal{E}_{\rm PD}$

In Chapter 3 we have introduced the Photodetection Efficacy $\mathcal{E}_{\rm PD}$ as the parameter that quantifies the photodetection capabilities of a Space-based

D [m]	$\mathcal{E}_{PD}$ [m^2]
12	3.315
8	1.473
4	0.368
2.5	0.144

Table 5.2: Photodetection efficacy vs. D.

UHECR. Here we study the correlation between the $\mathcal{E}_{PD}$ with the trigger threshold of the CTT.

Actually, the real energy threshold depends on both the trigger and the reconstruction efficiency, therefore the trigger threshold obtained with the CTT must be considered as the limit at which the energy threshold would approach if the reconstruction efficiency approaches to 1. We also assume that a simple algorithm like the CTT, relying on the most elementary properties of the signal, can be applied to different detectors without major changes.

We have used the *EUSO* phase A as the base configuration. To simulate a detector with a higher $\mathcal{E}_{PD}$ we scaled the size of the detector. We used the four *EUSO*-like detectors introduced in section 5.1.1.

The efficacy associated to every detector is computed using the (3.12). Since $\mathcal{E}^{tri}_{opt}$ varies with γ we used the on-axis efficacy as reference value. From the *EUSO* Phase A requirements [113] $\mathcal{E}^{tri}_{opt}(0) = 1.48$ m^2. For larger than *EUSO* detectors the optical triggering efficacy is scaled as the collection area. $G \sim 0.9$ and $\rho_{el} \sim 0.9$ are constant for all the configurations.

To compare the detectors on the same grounds we used the [3,4] trigger pattern, the configuration with the lowest energy threshold fulfilling the FTR requirements for all the detector's configuration.

For every detector we simulated 30000 proton EAS in clear sky atmosphere, with a flat energy distribution in logarithmic scale, i.e. $J(E) \propto E^{-1}$, in the energy range 10^{19} eV $< E < 5{\cdot}10^{20}$ eV and $\cos\theta$ angular distribution.

The corresponding trigger efficiency curves are plotted in Fig. 5.13.

We define the trigger threshold in energy E_{th} the energy above which the trigger efficiency is above 90%. The energy threshold as a function of $\mathcal{E}_{PD}$ is plotted in Fig. 5.14.

The number of both signal and background detected photons is proportional, by definition, to the $\mathcal{E}_{PD}$. Since the CTT exploits the intensity of the signal we expect E_{th} to scale as the signal to noise ratio $\frac{N_S}{\sqrt{N_N}}$. Therefore,

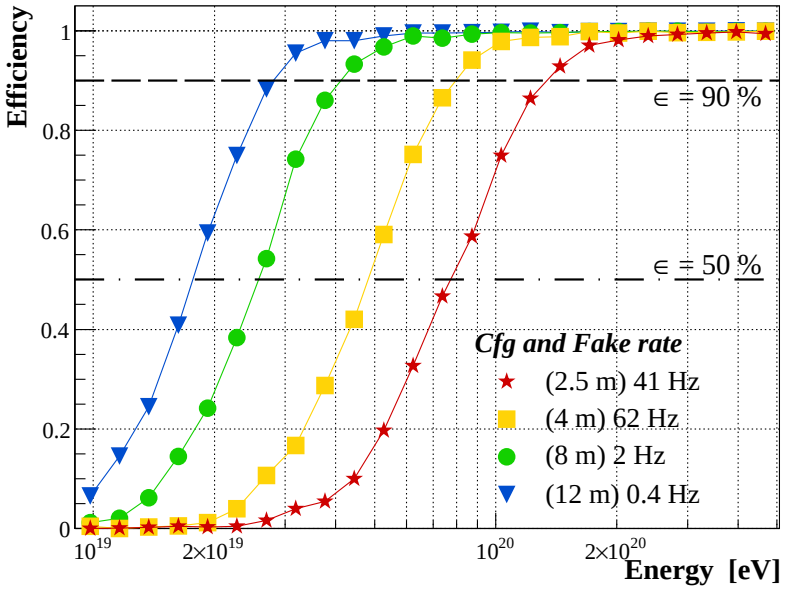

Figure 5.13: Energy threshold vs. D, the detector's diameter.

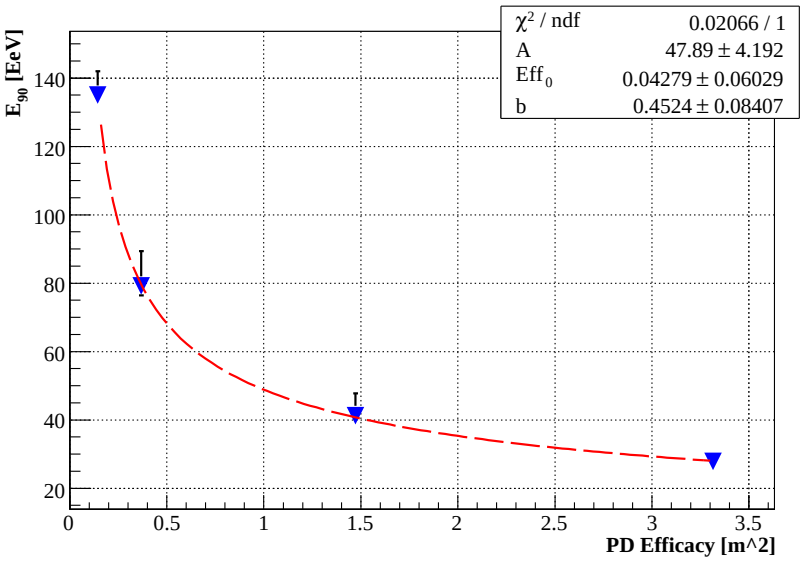

Figure 5.14: Energy trigger threshold E_{th} vs. $\mathcal{E}_{\text{PD}}$.

we fitted the data with the function

$$E_{\text{th}} = \frac{\alpha}{(\mathcal{E}_{\text{PD}} - \mathcal{E}_0)^{\beta}}. \tag{5.11}$$

The optimal values after the fit are: $\alpha = (47 \pm 4)$ EeV, $\mathcal{E}_0 = (4.2 \pm 6.0) \cdot 10^{-2}$ m^2 and $\beta = (0.45 \pm 0.08)$.

The result of the fit is in agreement with the expectation as β is compatible with 0.5 and $\mathcal{E}_0$ is compatible with 0.

5.4 Summary

The consequence of the relation between the trigger threshold and $\mathcal{E}_{\text{PD}}$ are relevant in the framework of a future Cosmic Vision mission. Using the performances of the *EUSO* Phase A design as a reference, a new mission aiming to reach an E_{th} lower by a factor of F will require a $\mathcal{E}_{\text{PD}}$ F^2 times *EUSO*'s. Supposing, in a very conservative approach, to use a detector exactly like *EUSO* as we did, increasing only the size, E_{th} would decrease proportionally the detector's entrance pupil diameter.

The Fig. 5.14 shows that, even with a 12 m diameter *EUSO*-like detector and an optimistic trigger, the trigger threshold is 3 times higher than the scientific requirements presented in Chapter 3. It is conceivable that the resources available to a future Cosmic Vision mission will be much less constrained than on the ISS. Nevertheless, even if a 4-5 meter detector will be feasible, without the support of new solution to improve the quality of the optics and of the photodetectors, the target threshold $E_{\text{th}} = 10^{19}$ eV will be out of reach.

Chapter 6

Characterization of a SiPM prototype

The improvement of the Photo-Detection Efficacy (see Sec. 3.2.5) will be one of the primary goals of any future mission for the observation of UHECR from space. The main research and development lines will be the design of large aperture, large FOV optics and the development of high quantum efficiency photo-sensors.

The Silicon Photomultiplier is a photon-counting solid-state detector concept devised a few years ago which aims to join together the silicon intrinsic high quantum efficiency, the high gain of the Geiger avalanche and a large dynamical range with low consumption and low voltage supply. Compared to the standard PMTs, a photodetector with these characteristics would have a deep impact on both the sensitivity of a space based UHECR telescope and its power, mass and volume budgets.

Several groups have been working during the past years on the implementation of the SiPM, applying different techniques and solution to reach the desired performances. The Max-Plank Institute für Physik of Munich, member of the *EUSO* collaboration, in cooperation with the Moscow Engineering Physics Institute and the MPI Semiconductor Laboratories in Munich has started a research and development program to produce SiPMs with high quantum efficiency in the near UV for applications in astrophysics and astroparticle physics.

Part of the work of this thesis has been done in Munich, hosted at the Max-Plank Institute, with the purpose of studying the characteristics of SiPM prototypes from Moscow Engineering Physics Institute (MEPhI) and their possible evolution from the point of view of the observation of

UHECR from space.

In this Chapter we will describe the working principle of the MEPhI SiPM design and present the characteristics we have measured at Max-Plank Institute (MPI) Munich. We will also describe a new method we have developed for the measurement of their quantum efficiency, or as it will be explained further on, their photo-detection efficiency.

6.1 PMTs, APDs and Silicon Photomultipliers

In every activity where the detection of extremely low light level is involved like nuclear, particle and astroparticle physics and medical imaging, the PMT have played a primary role. Their strengths are the high gain, high temporal resolution, single photon counting capability, high reliability and versatility thanks to the many models available on the market. Still some of their characteristic limit their performances and sometime their applications:

- the power supply of the order of few thousand volts, used to power the dynode chain up and obtain the multiplication process, implies the use of high voltage power supply,
- the need of shielding from direct light exposure due to the extreme sensitivity of the photocathode, which could ultimately result in its breaking,
- the limited photodetection efficiency, partly due to the quantum efficiency of the photoncathode and partly to the first dynode collection efficiency.
- a limited spatial resolution and high sensitivity to magnetic fields.

The higher quantum efficiency of solid-state devices makes high sensitivity semiconductor devices interesting competitors for PMT in the low light regime. Among the solid-state photo-detectors the Avalanche Photodiodes (APDs) combines the high quantum efficiency with internal gain. A high reverse bias voltage (up to 2 kV) creates a strong internal field that accelerates the electrons through the silicon and produces secondary electrons by impact ionization. The resulting electron avalanche can produce gain factors up to several hundred.

For the past few years mainly Russian groups pursued the development of a new type of APD, the Silicon Photomultiplier [114, 115, 116]. In this new approach the single photon counting feature of APDs operating

in Geiger mode is exploited. An APD is operating in Geiger mode if reversely biased a few Volts above the electrical breakdown voltage. A photo electron that reaches the high field region then initiates a avalanche breakdown. The breakdown is quenched by an external resistor which limits the current through the junction. A Geiger mode APD always gives an output signal independent of the number of primary charge carriers which initiated the Geiger breakdown. To overcame this limitation the SiPM combines the amplification of the Geiger mode and a large area and dynamic range implementing a matrix of several hundreds independent micro APD cells within an area of few mm^2. The sum signal of all cells is in first order proportional to the number of photons impinging on the whole sensor surface, provided the number of photons is small compared to the number of pixels. The main advantage of these devices compared to APDs is their very high intrinsic gain, of the order of $10^4 \div 10^6$, which makes a high performance preamplifier unnecessary.

The characteristics of the SiPM, together with an intrinsic insensitivity to magnetic fields make them very attractive for nuclear, particle and astroparticle applications and for space experiments.

Despite the number of years of development since the first presentation of the SiPM the technology has not reached the maturity to compete with the standard PMT. All the devices are still in the prototype stage and a number of common issues have to be solved:

- poor overall effective quantum efficiency (photo detection efficiency)
- limited pixel size $1 \times 1\ mm^2 \div 5 \times 5\ mm^2$,
- high dark noise rate at room temperature,
- intra micro-APDs cross-talk between.

The groups involved in the development are looking for alternative technical solutions to solve these issues which are proving themselves quite challenging. The incoming generation of new prototypes [117] seems to have partly cured some of these problems. In particular some claim an effective quantum efficiency of 40%.

6.2 The Silicon Photomultiplier

SiPMs are designed to work in Geiger mode exploiting the internal amplification of an avalanche process in the $p-n$ junction under a reverse bias voltage $|V_{\text{bias}}| > |V_{\text{breakdown}}|$. If an electron-hole pair is created in the

avalanche region, both carriers (i.e. electrons and holes) are accelerated under the influence of a strong electrical field. Upon acceleration the carriers continuously collide with the lattice structure. The typical value of the electric field in the multiplication region of a SiPM cell is about 10^5 V/cm. This soon saturates the carrier's velocity giving them enough kinetic energy to impact ionize the lattice. More carriers will in order perform the same operation as their parent carriers resulting in an avalanche breakdown. The multiplication process for both electrons and holes are shown in Fig. 6.1.

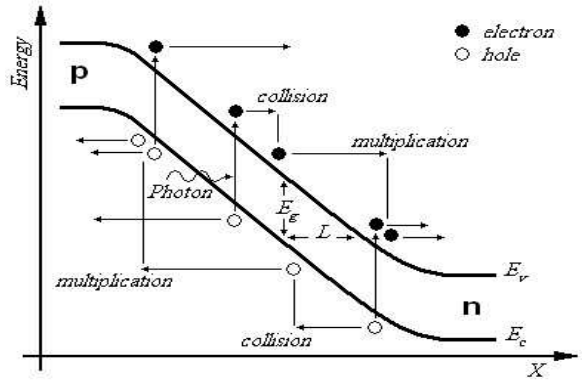

Figure 6.1: Charge multiplication by the avalanche process in high electric-field regions of a SiPM as illustrated in a band structure model.

6.2.1 Structure of the Silicon-Photomultiplier

The SiPM we tested is a 1×1 mm^2 matrix made of 42×42 μm^2 APDs (see Fig. 6.2). Each cell operates as an independent photon Geiger micro-counter, under bias voltage of 10-20% more than the breakdown voltage, so each carrier generated by photons or thermally gives rise to a Geiger-type discharge. This Geiger discharge is stopped when the voltage goes down below breakdown value due to external resistor R coupled to each cell.

Like Single Photon Avalanche Diodes (SPADs), in "Geiger Mode" the signal of the cell does not depend on the triggered carrier number which fires the cell. The discharge currents from the cells are added on the common load resistor and the output signal of the device is the sum of the signals from all the cells firing at the same time. High density of the cells ($100 \div 4000$ mm^{-2}) makes the response of the device linear over a wide range of light intensities.

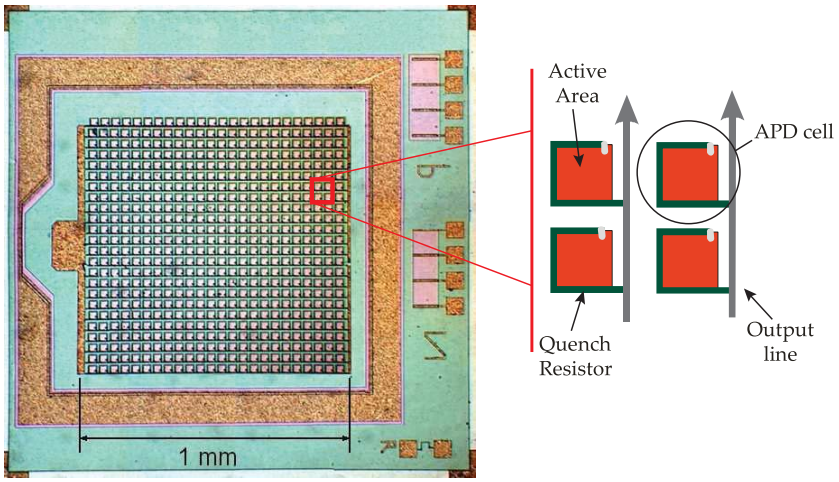

Figure 6.2: Silicon-Photomultiplier micro photograph. The 1 mm^2 SiPM consists of 576 cells with a size of 42×42 μm^2 each.

The SiPM semiconductor structure is shown in Fig. 6.3 (a and b): a few micron epitaxy layer on low resistive p substrate forms the drift region with low built-in electric field. A thin depletion region ($0.7 \div 0.8$ μm) between the p^+ and n^+ layers with very high electric field ($3 \div 5 \cdot 10^5$ V/cm) is created. By applying a bias voltage $|V_{\text{bias}}| > |V_{\text{breakdown}}|$ a Geiger mode discharge takes place if the cell is triggered. The electrical decoupling between the adjacent cells is provided by polysilicon resistive strips connected to the n^+ layer (anode). The uniformity of the electric field within a cell is provided by the n^- guard rings around each cell-anode. All cells are connected by common Al strips, in order to readout the SiPM signal.

6.2.2 Dynamic range and Photo Detection Efficiency

As the detector has a finite number of pixels, the dynamic range is limited. The saturation of the signal with increasing light intensity can be calculated, assuming that the dispersion of each number of photons arriving on the detector is poissonian (we must take it into account, because the tail of this Poisson distribution will be more affected by the saturation than its head). The number of pixels fired depends on the number of photons arriving on the detector as [119]:

$$N_{\text{fired}} = m \cdot \left(1 - e^{\frac{\varepsilon_{\text{PD}} N_{\text{ph}}}{m}}\right) \tag{6.1}$$

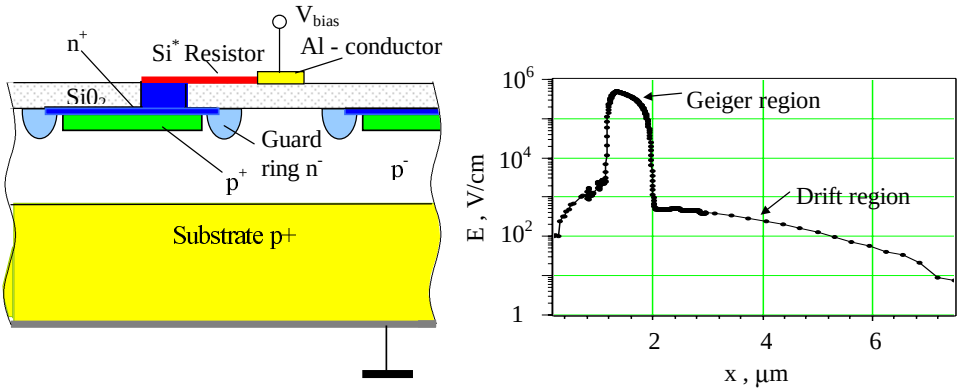

Figure 6.3: a) Topology of a SiPM b) Electric field distribution in epitaxy layer of one SiPM-cell (taken from [118]).

where ε_{PD} is the detection efficiency and m the total number of microcells of the SiPM.

The Photo Detection Efficiency (PDE) ε_{PD} is wavelength dependent and related to the quantum efficiency according to:

$$\varepsilon_{PD}(\lambda) = QE(\lambda) \cdot \eta_{Geiger} \cdot \eta_{Geo} \tag{6.2}$$

where $QE(\lambda)$ is the quantum efficiency (typically $30 \div 80\%$, wavelength dependent), η_{Geiger} is the probability for a carrier created in the active cell area to initiate a Geiger-mode discharge and

$$\eta_{Geo} = \frac{\sum_m A_{Cell}^{active}}{A_{SiPM}} \approx \frac{A_{Cell}^{active}}{A^{Cell}} \tag{6.3}$$

is the so-called geometrical efficiency. A^{active} is the active area. This approximation is acceptable when discussing the PDE of a single pixel, SiPM. A multi-pixel SiPM would also suffer from the dead areas due to the packing of the single pixels together. However it is conceivable that this issue can be solved with a proper dedicated design, once that the single pixel SiPM will be well established. One of the most problematic aspects of the SiPM is the correct evaluation of the PDE. The cross talk between microcells, which will be discussed later, makes the estimation of ε_{PD} complicate because, out of a k fired cells is not possible to know precisely how many of them have been triggered by incident photons and how many by the cross talk. The development of a technique to measure the PDE with a good precision is the main topic of the last part of this Chapter.

6.3 Measurement of the properties of a SiPM prototype

During the measurement campaign at MPI we used two different set of 1×1 mm^2 SiPM provided by MEPhI and PULSAR Enterprise. They were belonging to different batches and therefore had rather different behavior. The first batch was made of 576 cells per pixel while the second of 1024 cells per pixel. The measurements we describe have been carried out on the 576 cells model, for the other shown much poor performances. The 1024 cell SiPM has been used afterward to test the PDE method only because the 576 cell model was not available any more.

The preliminary measurements we have performed are aimed to understand the basic properties of the SiPM prototype. Since the development of the SiPMs is ongoing, the characteristics of the prototypes may have large variations from a batch of prototypes to the next one. The schematic electric circuit of a such device is shown in Fig. 6.4a. The variable capacitance C_{APD} in stands for an APD-microcell. A resistor R_c and a capacitance C_c are coupled in parallel to each cell. C_n represents the capacitance of the aluminum network that connects the cells together. The value of R_c and C_c depends on the production process and they have to be estimated from the SiPM gain and recovery time.

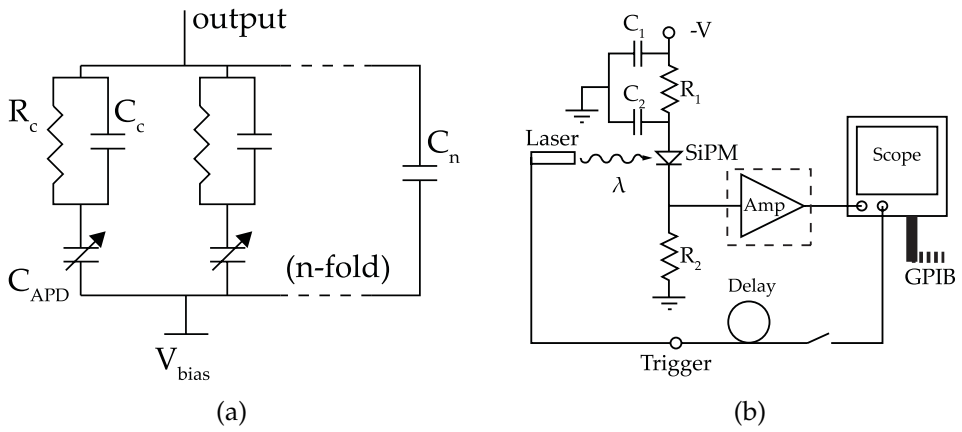

Figure 6.4: (a) Scheme of the equivalent embedded circuit. (b) Setup used in the measurement of the SiPM properties.

The scheme of the circuit to measure the basic properties of the SiPM is sketched in Fig. 6.4b The SiPM detector is connected according to Fig. 6.4a.

R_1 is of the order of the MΩ and limits the current flowing through the detector. R_2 1 kΩ is the output resistance of the circuit. The digital oscilloscope (LeCroy, Model9362, 1.5 GHz, 10 GS/s) has been used either in self-triggering mode or external triggering mode, depending on the quantity to measure. In self triggering mode the threshold was typically set to half the height of the single microcell peak. The oscilloscope was connected via GPIB to a PC. We have used the Labview framework and its GPIB libraries to create a simple program for setting the oscilloscope up automatically and for pulse distribution data acquisition.

6.3.1 The SiPM signal

The typical SiPM signal is shown in Fig. 6.5a. As expected the device is completely quite while increasing the voltage supply until the breakdown voltage is reached. For the prototype we measured, the breakdown voltage was 51 V. Once the Geiger regime is reached the signals stand clearly over the noise. The signal to noise ratio The plots refer to signals obtained with ~ −56 V bias. In Fig. 6.5b, switching on the persistency in the oscilloscope and triggering on the signal just above the noise, the signals corresponding to 1, 2, and 3 cells firing simultaneously have been superimposed. The signal are neatly separated; the violet area on the right of the three peaks points out the presence of afterpulses.

The rise time is of the order of ~ 500 ps, while the FWHM is ~ 2 ns.

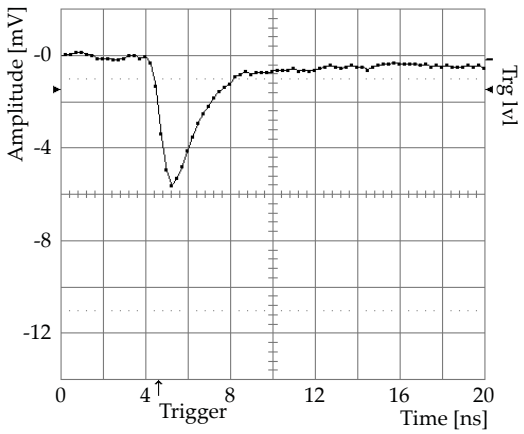

(a) Single micro-cell SiPM signal

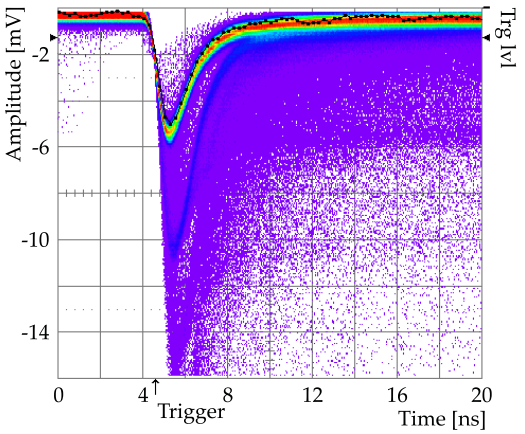

(b) Superposition of several SiPM signals. Peaks corresponding to 1,2 and 3 cells firing together are visible.

Figure 6.5: MEPhI 576 prototype signal, bias voltage −56 V.

6.3.2 The SiPM gain

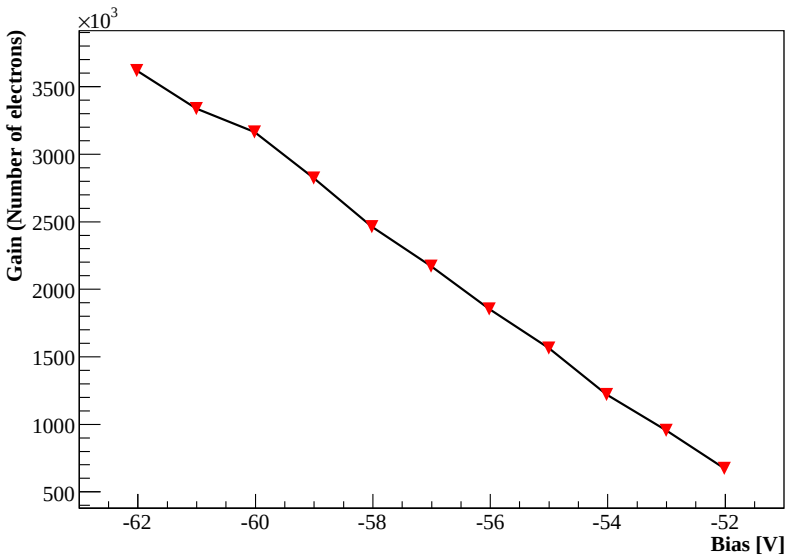

Figure 6.6: Measured SiPM Gain vs. the reverse bias voltage.

Fig. 6.6 shows the gain linearity vs. reverse bias voltage for the tested SiPM with 576 cells. The gain M of the SiPM is deduced by measuring the single cell pulse area according to:

$$M = \frac{Q_c}{e} = \frac{\int \mathrm{d}t\, V(t)}{e \cdot Z} \tag{6.4}$$

V is the pulse shape, e the elementary charge and Z the input impedance of the used oscilloscope. The charge accumulated in the cell capacitance C_c is simply given by: $Q_c = C_c(V_{\text{bias}} - V_{\text{breakdown}}) = C_c \Delta V$. Thus the single cell capacitance can be calculated as

$$C_c = \frac{e \cdot M}{\Delta V} \tag{6.5}$$

It is found to be 40 fF for this tested SiPM prototype. The typical single cell "gain" is $1 \div 2{\cdot}10^6$, i.e. in the same order as vacuum PMT gains.

6.3.3 Dark noise

An important aspect of the SiPMs is the dark rate. It determines the coincidence efficiency, the noise and the power consumption of the detector. Two

effects contribute to the dark pulses, i.e. pulses generated when the SiPM is not illuminated: the thermal electron-hole pairs production near or in the active region and the generation due to tunneling of carries through the junction. The former component depends on the operating temperature while the latter on the quality of the design and the purity of the silicon. Furthermore the dark count rate is proportional to the size of the active area of the microcell. In fact the the larger the microcell are the larger the probability a pair is generated in the active area. The dark noise depends also on the bias voltage, as the Geiger efficiency becomes higher. We have measured the dark noise rate using a Camac counter, a discriminator and a 10x amplifier and a gate generator. The SiPM output is amplified and compared to a threshold of ~ 2 mV and then fed to the counter. The gate generator defines the counting time interval (3.6 s).

The plot in Fig. 6.7 shows the SiPM's dark rate measured for as a function of the bias voltage. A dark rate of $1 \div 10$ MHz is very high, considering

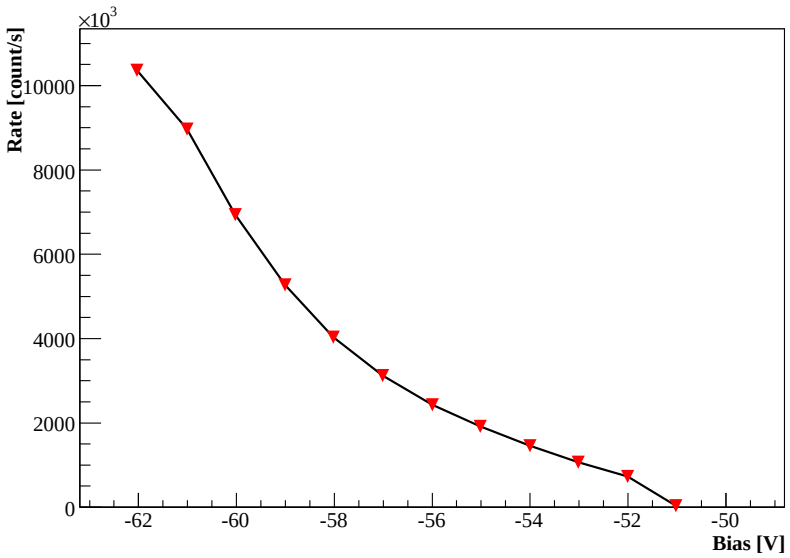

Figure 6.7: Dark Rate vs. the bias voltage at room temperature.

the limited area of the device (1 mm^2), and limits its use to applications where the either the background rate is of the same order of magnitude, or the detection is done using two or more SiPM in coincidence, like in PET scanners, for instance. The dark rate decreases with the temperature as the thermal pair generation probability decreases. Cooling down the SiPM appears, up to now, the only solution to keep the dark rate low in

prototypes with larger area. The recently issued $5 \times 5\,\mathrm{mm}^2$, 2500 micro-cell prototypes require to be cooled down to $-60°$.

6.3.4 Single photoelectron detection

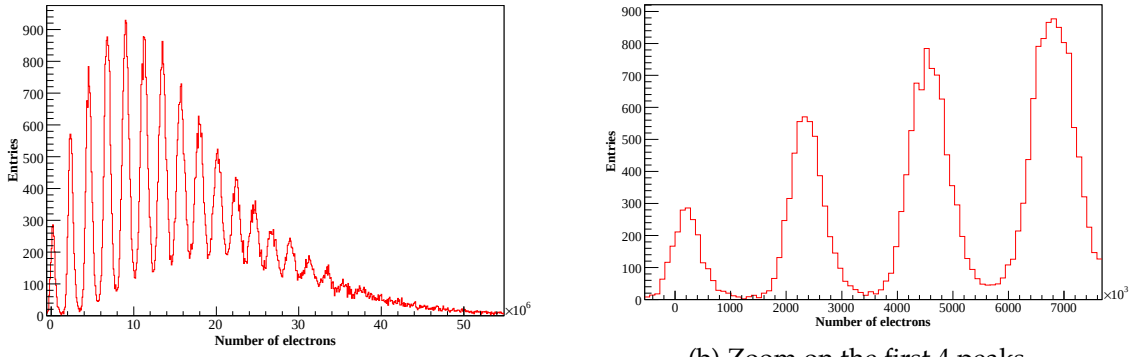

(a) ~ 7 photoelectrons pulse distribution.

(b) Zoom on the first 4 peaks.

Figure 6.8: Pulse distribution detected by 576 cell SiPM using Laser pulses and bias voltage -56 V corresponding to (a) ~ 7 detected photoelectrons and (b) the zoom on the first peaks.

The Geiger mode makes SiPMs like APDs or SPAD ideal for the single photon detection. Provided that the electron-hole pair is generated in the active area within the depletion region, the detection capability are excellent due to the naturally high signal to noise ratio. The response of the tested SiPM in coincidence with the laser pulse pulses are shown in Fig. 6.8.

In principle, for a low light flux one can count the average amount of photoelectrons per single lase light flash detected by the device. In fact with the available prototypes the possibility to use SiPMs for photon counting is limited chiefly by the dark noise, but also by the cross talk. For very high trigger rates however, the signal detection capability of the SiPM is limited by the recovery time of the whole cell-matrix. During the recovery time, no or only partial avalanche breakdowns takes place even if many photoelectrons enter the avalanche region of one cell.

6.3.5 Optical cross-talk

In general, reverse biased silicon-diodes emit light when they are operated in Geiger mode [120]. The carriers released during the avalanche have a

temperature high enough to emit blackbody radiation. This fact leads to a photon assisted crosstalk between the cells of the SiPM. Photons emitted by a cell while firing could trigger the surrounding cells. The quoted emission rate is ≈ 3 photons every 10^5 carriers in the avalanche. The effect

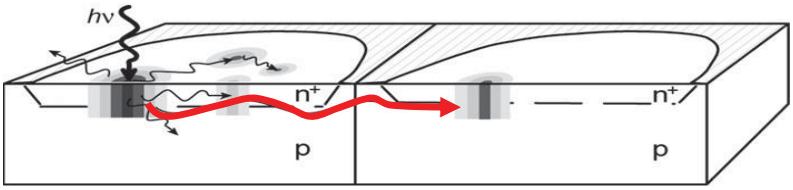

Figure 6.9: Sketch of the optical cross-talk mechanism [121].

of the cross-talk is clearly visible in the dark pulsed distribution. Since the electron-hole pairs are generate randomly, the odds of two cells firing at the same moment are very low and even less for 3 cells firing. Assuming a dark noise rate of 5 Mhz, signal width of 2 ns, the probability of 2 cell firing together is ≈ 0.01, going down to 10^{-4} if we require 3 cells. The visibility of both the 2 cells and 3 cells signals in Fig. 6.5b is then a clue of a cross talk mechanism.

We have measured the dependence of the cross-talk on the bias voltage from the dark pulses distribution spectrum(see Fig. 6.10a). The dark pulse distribution has been measured setting the oscilloscope to self-triggering mode. We have assumed the probability that two or more cells start the avalanche together to be negligible. Hence the cross-talk probability is given by

$$P_{\mathrm{CT}} = 1 - \frac{I_{1^{\mathrm{st}}}}{I} \tag{6.6}$$

where I and $I_{1^{\mathrm{st}}}$ are the number of entries in the pulse distribution and in the first peak respectively. The result are shown in Fig. 6.10b. The probability increases with the reverse bias voltage, as the number of carries rises (see Sec. 6.3.2) and the Geiger mechanism becomes more efficient. On average, more than 50% of the pulses of the device we examined where affected by cross-talk. The cross-talk becomes an issue when a precise measurement of the number of detected photons is necessary. Furthermore, when the number of photons is comparable to the dynamical range, the cross-talk reduces the dynamical range further.

To solve this issue, in the last 5×5 mm^2 prototypes have introduced a trench filled with optically thick material between the APDs to block thecross-talk photons generated in the neighbouring cells.

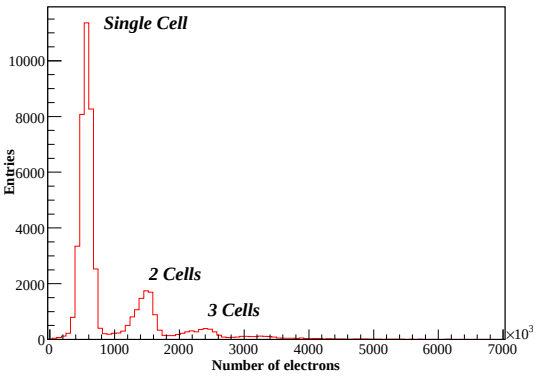

(a) Dark pulse distribution detected at −56 V bias.

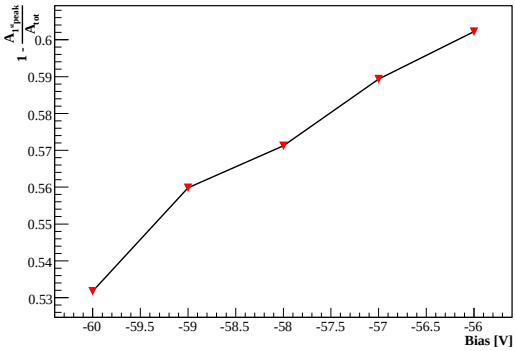

(b) Cross-talk measurement: fraction of dark noise signals with more than 1 cell firing.

Figure 6.10: (a) ~ 7 detected photoelectrons and (b) the zoom on the first peaks.

6.3.6 Recovery time

The dead time after the Geiger avalanche has been generated is due to the finite time taken to quench the avalanche and reset the diode voltage to its initial value. The recovery time depends on R_c and C_c, the quenching resistor and the intrinsic capacitance of the diode. R_c and C_c are dimensioned to have a recovery time

$$\tau = R_c \cdot C_c \gg t_{\text{discharge}} \approx 1\ \text{ns}, \tag{6.7}$$

so that the passive quenching is effective.

Due to the parallel readout of the pixels, is not possible to measure directly the recovery time of the cells of the SiPM. Measuring the recovery time of the whole matrix is misleading because the the result doesn't depend on R_c and C_c only but also on aluminum network capacitance. Instead we are interested in the recovery time of the single cell for that is the relevant quantity when measuring very low light fluxes.

To overcome such kind of difficulties and the prototype are equipped with 3 test structure etched on the main matrix side: 1 cell, 4 cells and 8 cells. For the recovery time measurement we used a SiPM from the same sample of the one we used in the other measurements where the output terminals where connected to the single cell test structure. In Fig. 6.11a is shown the amplitude profile of the dark noise pulses of the single cell test structure following the laser pulse.

The recovery time has been measured firing two laser pulses on the single cell with a delay included between 64 ns and 900 ns. The result is

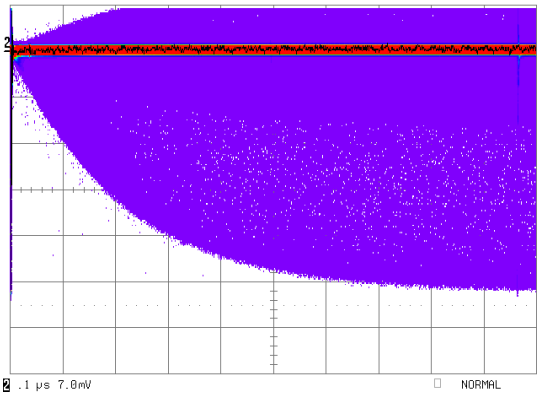

(a) Amplitude profile of the dark noise pluses which follow a laser pulse. After the laser pulse the cell is recharging and the all the avalanches induced before the recharge process is complete produce smalled pulses. The picture has been obtained triggering on the laser and activating the persistence on the oscilloscope.

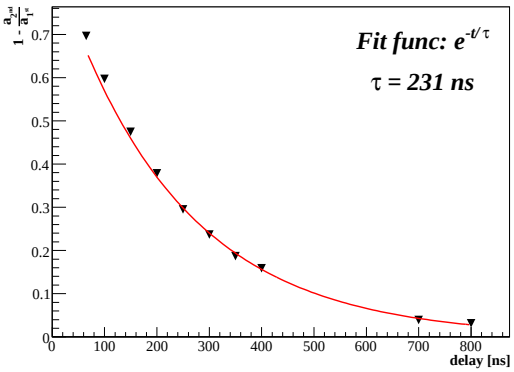

(b) Fit of the recovery time. $a_{1^{st}}$ and $a_{2^{nd}}$ are the amplitudes of the first and second laser pulse. To enhance the resemblance with (a), the recovery has been expressed as $1 - \frac{a_{1^{st}}}{a_{2^{nd}}}$.

Figure 6.11: Recovery time measurement.

shown in Fig. 6.11b Using the recovery time (6.7) is possible to calculate the impedance of the polysilicon resistor R_c. From (6.7) $R_c \simeq 5\,\mathrm{M}\Omega$.

6.4 Measurement of the Photo Detection Efficiency

The photo detection efficiency is probably the most subtle among the SiPM characteristics to measure. On the other hand, one of the greatest hope of the scientific community concerning SiPMs is to have a high QE photosensor, which makes the PDE the most interesting characteristic to measure. The difficulty of this measure comes from the nature of the SiPM as a photon counting device with limited dynamical range from the cross-talk and from the high dark noise rate. Henceforth the common methods using a DC light source should be avoided. We have developed a new method which is not influenced by the particular features of the SiPM and that should give a precise measurement of the real PDE.

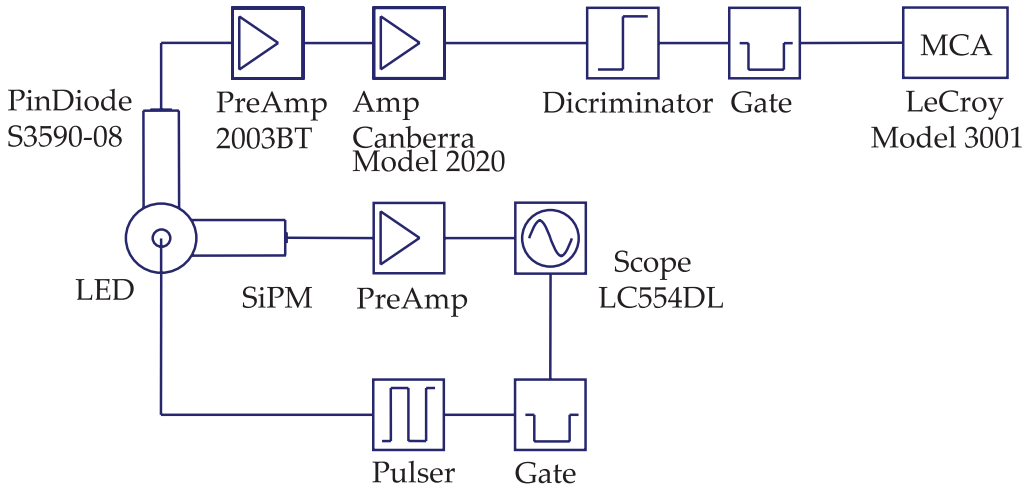

Figure 6.12: Block scheme of the experimental setup for the PDE measurement.

6.4.1 Measurement Procedure

The setup we used is shown in Fig. 6.13 and 6.12. With this construction we simultaneously measure the signal from a reference detector, a calibrated photodiode (*Hamamatsu APD S3590-08*), and the detector under investigation. As light source we are using pulsed monochromatic LEDs. The pulse duration of a single LED flash is about one ns. The LED is directly emitting into a hollow cylinder made out of spectralon, a diffuse reflecting material of high reflectivity [122]. We have simulated the characteristics of this sphere and obtained that on average a photon is reflected 100 times within the spectralon cylinder before it leaves the sphere or is absorbed. The decay time of the light intensity is of the order of 10 ns. The light can escape from the sphere in two directions through holes of different sizes. On each of these exit holes a cylinder is attached to the integrating sphere. Each cylinder is closed on its open end with a diaphragm which is tailored to be smaller then the active area of the photon detector installed behind the diaphragm.

The relative ratio of light intensities at both detector positions has been measured with a constantly emitting LED and a PiN diode which has been interchanged between both positions. The ratio of photocurrents of the PiN diode at the two positions gives the relative ratio of the light intensities including all inhomogeneities and geometrical effects. To check

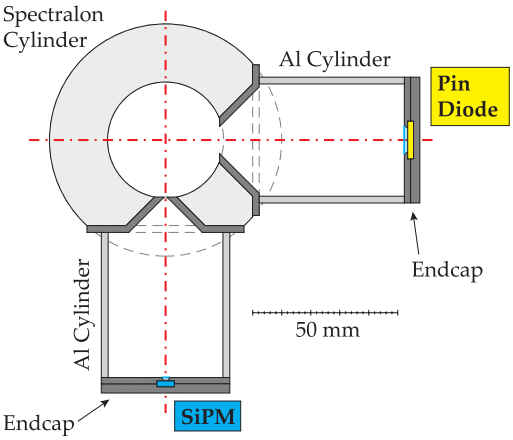

(a) The schematics of the setup of the PDE measurement. A pulsed light source is emitting light into the integrating sphere and the light is distributed with a fixed splitting ratio between the reference detector and the detector under investigation.

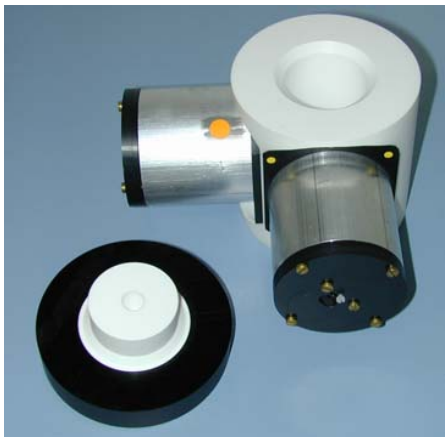

(b) Picture of the setup.

Figure 6.13: PDE measurement setup.

for systematic effects we used several LEDs and obtained the same result within 2%.

For the measurement of the PDE of the SiPM for each LED shot the signal of the PiN diode is preamplified with a charge sensitive amplifier (*Canberra BT2003*) and a successive Spectroscopy amplifier (*Canberra 2020* shaping time 3 μs). The processed event is then recorded by a multichannel analyzer (LeCroy 3001). By converting the measured signal into photoelectrons and taking the relative intensity ratio between the two detector positions into account one obtains the mean number of photons at the position of the SiPM. The calibration of the PiN diode signal chain in photoelectrons is performed with an ^{241}Am 59 keV-γ-source (Fig. 6.14). A fully absorbed 59 keV $-\gamma$ is in Silicon on average generating

$$N_e = \frac{59\ \text{keV}}{3.62(\text{pairs/eV})} = 1.5{\cdot}10^4\ \text{e}^- \tag{6.8}$$

By using a microscope we have positioned the *SiPM* behind the diaphragm. The size of the diaphragm is ~ 0.8 mm i.e. smaller than the active size of the SiPM. The signal of the SiPM is processed with a *LeCroy LC554DL* oscilloscope after the signal has been amplified with a 500 MHz broadband amplifier *MAN-1LN* from Mini-Circuits. Within a 140 ns window opening short before the LED fired the scope is looking for a minimum

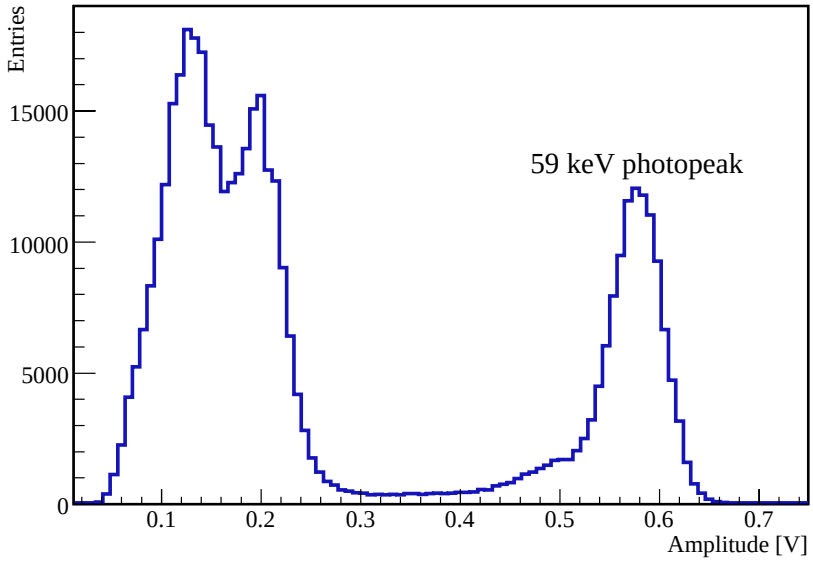

Figure 6.14: ^{241}Am 59 keV spectrum measured with the PiN diode.

amplitude and transfers this value to a PC by using a *GPIB* readout. The mean number of photoelectrons (μ) per event is extracted from the relative number of events in which no pixel has fired (N_0). These events can be very well separated from the remaining events. According to Poisson statistics the probability to record 0 photoelectrons is given by

$$P_0 = e^{-\mu} = \frac{N_0}{N_{\text{tot}}} \qquad =: \qquad \mu = -\ln \frac{N_0}{N_{\text{tot}}} \tag{6.9}$$

where N_{tot} is the number of LED shots. In the same way one obtains the contribution due to dark counts if the LED is switched off. In deriving μ in this way one avoids systematic effects introduced by optical crosstalk. Finally the photon detection efficiency is the ratio of the mean number of photoelectrons detected by the SiPM to the mean number of incident photons.

6.4.2 Results

We have verified our method by measuring the PDE of a HPD *R9792U-40* from Hamamatsu which is currently under study for using it in the MAGIC II experiment. Due to the capability of HPDs to resolve single

λ [nm]	**PDE** (meas)	**QE** (Hamamatzu)
395	24 ± 1	-
400	-	28.7
590	27 ± 1	31.5
610	23 ± 1	27.0

Table 6.1: Measurement of an HPD type *R9792U-40* by Hamatzu. Comparison by the cathode's QE declared by the manifacturer and the measured PDE.

photoelectrons our method can be applied without any change. As the gain of HPDs is $< 10^5$ we reduced the gate to from 140 ns to 60 ns to have sufficient signal to noise ratio. We measured the PDE at three different wavelength. The results are listed in Tab. 6.1. The PDE is compared to the photocathode's QE claimed by the manifacturer and the QE measured in MPI. The PDE is systematically 5% lower than the QE. A reasonable hypothesis that could account for this difference is that the QE doesn't include the probability for the photoelectrode accelerated by the magnetic field to be backscattered. For further details refer to [123]. Nevertheless this is still under investigation and has to be verified.

Finally we applied the measurement to the SiPM prototypes. At the time when we developed this technique the 576 microcells SiPM was not available any more. We had to use a different prototype with different characteristics from the one measured in the first part of the Chapter. Unfortunately the device under study didn't have the same performances as the 576 cells SiPM.

The results for one SiPM is shown in Fig. 6.15.

As mentioned before the 1024 SiPM has shown poor performances since the beginning, so the poor quantum efficiency, below 4% even at the peak, is not completely unexpected. On the contrary the maximum efficiency is in the red wavelength region and decreasing toward blue wavelengths as expected from the structure of these devices (p substrate). In fact one of the limits of the application of the current SiPM design to UV detectors is their limited efficiency at those wavelength. The motivation is the absorption length of the Si that in the UV is ~ 0.2 μm. In the current structure the active region is currently deeper and only a fraction of the photons induced carriers give rise to an avalanche.

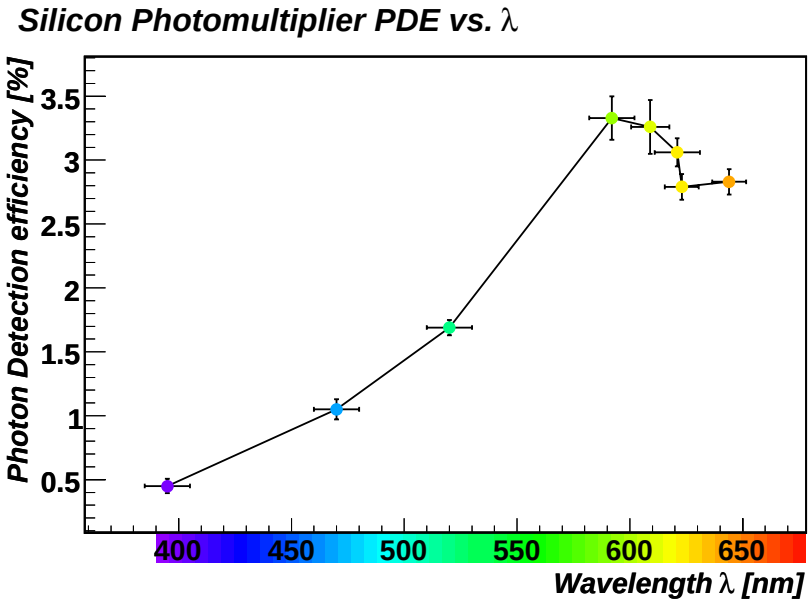

Figure 6.15: Photon detection efficiency of a SiPM vs. wavelength. The SiPM used here has 1024 cells on one square millimeter sensor area.

Conclusions

The work of this Ph. D. thesis developed in two contexts: the *EUSO* experiment and, after *EUSO* was put on hold, the preliminary studies for a mission proposal to the ESA Cosmic Vision 2015-2025 Call for proposals.

In the context of the *EUSO* experiment, the research activity has been focused on the development of ESAF. ESAF is the first software which implements the whole simulation chain: the interaction of the primary particle in the atmosphere, the light production and transmission to the detector and the simulation of the detector itself. ESAFhas been designed with a modular structure to provide the flexibility required by the *EUSO* Phase A study. Furthermore, the same flexibility extends the ESAF's scope beyond *EUSO*. The structure can accommodate new detectors with a small effort.

We used ESAF to develop and study the performances of a new trigger for *EUSO*, the Contiguity Tracking Trigger. The trigger is based on a contiguity algorithm to perform a fast selection between the incoherent noise and the EAS tracks. The simplicity is one of the strengths of the algorithm. It can be implemented in the front-end electronics to minimize the power consumption. With ESAF we tuned the parameters to keep the fake trigger rate to a level acceptable by the severe telemetry constraints. The trigger was tested on a large sample of showers and used to select the set of parameters which grant the best efficiency.

In the context of the mission planning for the ESA Cosmic Vision Call for proposals, the activity was structured as follows:

We investigated the relations between the scientific requirements and the mission requirements with an analytical and semi-analytical approach. The resulting set of equations is a solid base for the mission definition as sets the requirements the instrument must fulfill to detect EAS with the necessary angular and energy resolution. The most relevant outcome regards the photo-detection efficacy $\mathcal{E}_{\mathrm{PD}}$, the parameter that affects the performances at low energies the most. We derived that to observe 10^{19} eV EAS the photo-detection efficacy must not be smaller than $\gtrsim 2\ \mathrm{m}^2$. Assum-

ing the use of an ideal optics and standard MAPMT, it turns out that the entrance pupil diameter must not be smaller than $D_{\min} \gtrsim 4.5\,\mathrm{m}^2$. Applying a correction to take into account the losses of a real optics, $D_{\min}$ rises by a factor of 2. These considerations imply that the 10^{19} eV threshold goal will be achievable only with high quantum efficiency detectors.

To complement the analytical approach with the full Monte-Carlo, we used ESAF to derive the relation between the photo-detection efficacy and the performances of the detector. Since *EUSO* will be the reference point for the design of the next generation detector, we used the *EUSO* Phase A configuration as a working model for a future instrument. The photo-detection efficacy of the simulations has been extended scaling the size of *EUSO*. These extended detectors were compared on the basis of the CTT trigger threshold. We showed that the trigger threshold depends on $\sqrt{\mathcal{E}_{\mathrm{PD}}}$. Decomposing the photo-detection efficacy in its factors we obtained the following implications:

1) The trigger threshold is proportional to D^{-1}, where D is the entrance pupil diameter. In fact, the number of detected signal photons is proportional to the optics aperture, i.e. to R^2, but the same factors applies to the number of background photons collected in the same time interval. Then, the net gain is roughly proportional to the signal to noise ratio $N_{\mathrm{S}}/\sqrt{N_{\mathrm{B}}}$.
2) For the same reason, an improvement of the quantum efficiency by a factor A lowers the threshold by a factor $\sqrt{A}$.
3) A reduction of the optics aberrations would improve the signal to noise ratio and therefore the strength of the signal over the noise. A reduction of the optic's FOV simplifies the design of the optics and improves the quality of the point spread function. This option must be considered in the design of a new mission according to the requirements on the energy threshold.

The last part of the thesis is dedicated to the characterization of a SiPM prototype as a possible alternative for a future UHECR experiment. Nowadays the SiPM are single pixel solid-state devices with good photon counting capabilities. Their compactness, intrinsic radiation hardness and low power consumption will make them one of the best candidate for space applications on condition that in the next years some of the major problems will be solved. In detail

1) The PDE measured in prototypes available in 2005 was mostly below the PDE of Bialkali PMTs, especially in the $300 \div 400$ nm wavelength

range. In 2006 the compiletion of a new batch of prototypes which could rise the PDE to 40% in the yellow region [124] is foreseen. However, high PDE in the near UV seems problematic. Some groups have proposed to use wavelength shifter exploit the better PDE in green-yellow.

2) The dark noise rate per square mm is the second main issue of these devices. The tested models presented a dark hit rate of $\sim 1 \div 10$ MHz depending on the bias voltage. If scaled to the *EUSO* pixels size, 4×4 mm^2, the dark noise rate would rise proportionally to $\gtrsim 16$ MHz which has to be compared with the expected background rate of $\sim$ 1 MHz per pixel. On ground the solution is to cool the system down to reduce the thermal pair generation probability to temperatures of the order of $-60°$. For a space experiment, the need of a cooling system on board would mean an increase of mass and power consumption, balancing or canceling the low power and mass advantages of the SiPM employment. For a future experiment, if we assume the same FOV granularity $\sim 0.1°$ and the same $f/\# \simeq 1$, the problem of dark noise becomes even more severe will require even bigger pixels

3) The cross-talk relevance, as regards the EAS signal detection, depends on the implementation of the electronics. The efficiency of a counting digital electronics like *EUSO*'s would not be affected by the cross-talk as it counts the number of pulses, not caring about their amplitude. In any case dedicate technical solutions like the use of optical thick trenches [125] seem to have reduced the cross-talk to a negligible level.

4) The packing factor. Nowadays SiPMs are produced as a single-pixel device. An important step forward will be achieved when multi-pixel SiPM will become available although solution in which many single-pixel devices are assembled together are conceivable acceptable packing factor.

The SiPM development in the next years will be decisive to establish whether they will become a competitive candidate.

The results presented in this dissertation are a part of an ongoing effort aimed at the preparation of a mission for the observation of the UHECR from space. In particular the next step are the following: i) Evaluation of the trigger efficiency when clouds are present in the field of view which shorten the visible track length. ii) Completion of the main modules of the reconstruction chain to evaluate the combined trigger and reconstruction efficiency and energy threshold as a function of the photo-detection efficacy

iii) The monitoring of the new development of the SiPM technology in the next yeas. The 2015-2025 time frame poses strict limits to the time left for the improvement of the design, considering that the device has to undergo strict test procedure to be qualified for space.

Appendix A

Acronyms

CM Center of Mass

UHECR Ultra High Energy Cosmic Ray

EAS Extensive Air Shower

CMB Cosmic Microwave Background Radiation

CNB Cosmic Neutrino Background

IRB InfraRed Background Radiation

GZK Greisen-Zatsepin-Kuzmin

AGN Active Galactic Nuclei

TD Topological Defect

GUT Great Unification Theory

LPM Landau-Pomeranchuk-Migdal

CR Cosmic Rays

LD Lateral Distribuction

DSAM Diffusive Shock Acceleration Mechanism

CRF Cosmic Rest Frame: the reference frame where the cosmic radiation is isotropic

PP Pair Production

PPP Pair Production by Proton

QED Quantum ElectroDynamics

GRB Gamma Ray Burst

COBE Cosmic Background Explorer

WMAP Wilkinson Microwave Anisotropy Probe

ICS Inverse Compton Scattering

EUSO *Extreme Universe Space Observatory*

OWL *Orbiting Wide-angle Light-collectors Experiment*

AGASA *Akeno Giant Air Shower Array*

SUGAR *Sidney University Giant Air-shower Recorder*

PAO *Pierre Auger Observatory*

HiRes *High Resolution Fly's Eye*

ESA European Space Agency

ISS International Space Station

FOV Field Of View

EC Elementary Cell

PDM Photo-Detector Modules

PCB Printed Circuit Board

OM Optical Module

EP Entrance Pupil

PD Photo Detector

PSF Point Spread Function

FS Focal Surface

FTR Fake Trigger Rate

PMT Photomultiplier

MAPMT Multi Anode PhotoMulTiplier

SiPM Silicon Photomultiplier

APD Avalanche Photodiode

HPD Hybrid Photodiode

SPAD Single Photon Avalanche Diode

PDE Photo Detection Efficiency

ASIC Application Specific Integrated Circuit

ESAF EUSO Simulation and Analysis Framework

CTT Contiguity Tracking Trigger

GTU Gate Time Unit

MEPhI Moscow Engineering Physics Institute

MPI Max-Plank Institute

Appendix B

Table of symbols

Table B.1: Commonly used symbols

Var	*Description*	*Unit*
λ	photon wavelength	[nm]
$\hat{v}$	Shower direction, unitary	[-]
$\hat{\sigma}$	line of sight, unitary, referred to the position maximum	[-]
$R_{\oplus}$	Earth radius	[km]
H	Detector's altitude	[km]
$\gamma_{\max}$	FOV half angle	[°]
β_{M}	Earth's center angle correspondent to $\gamma_{\max}$	[°]
β_{hor}	Horizon angle	[°]
α_{tilt}	Detector's tilt angle	[°]
θ	Shower's zenith angle	[°]
γ	$\mathcal{S}_{ref}$ location in the FOV and photons' incident angle	[°]
η	Duty cycle	[-]
η_{o}	Observational duty cycle	[-]
τ_{dead}	Instrumental dead time	[-]
η_{c}	Cloud coverage efficiency	[-]
Y	Fluorescence Yield	[ph·particle^{-1}·m^{-1}]
h_0	Atmosphere characteristic length	[8.3 km]
λ	EAS attenuation length	[g/cm^2]
$X_{\max}$	Depth of the EAS maximum	[g/cm^2]
X_0	Depth of the EAS fisrt interaction	[g/cm^2]

Table B.1: Commonly used symbols

Var	*Description*	*Unit*
ζ	angle between the shower's direction and the line of sight.	[°]
D_{EP}	Entrance Pupil Diameter	[m]
D_{PD}	Photon Detector Diameter	[m]
$f/\#$	Focal Number	[-]
d_b	Focal surface bucket diameter	[mm]
M	Irradiace	[ph·m^{-2}·s^{-1}]
F	Photon flux	[ph·m^{-2}]
N_{pe}^{tri}	Number of triggering photo-electrons	[ph]
$\mathcal{E}_{\mathrm{PD}}$	Photodetection Efficacy	[m^2]
$\mathcal{E}_{\mathrm{opt}}^{\mathrm{tri}}$	Optical Triggering Efficacy	[m^2]
$\varepsilon_{\mathrm{PD}}$	Photo sensor photo-detection efficiency	[-]
G	PD filling factor	[-]
$\mathcal{A}^{\mathrm{geo}}$	Geometrical aperture (acceptance)	[km^2·sr]
$\mathcal{A}^{\mathrm{eff}}$	Effective aperture (acceptance)	[km^2·sr]
Σ	Exposure	[km^2·sr·yr]
ω_{EAS}	Angular velocity of the shower on the focal surface	[rad·s^{-1}]
ξ_{EAS}	EAS angular extension on the detector's focal surface	[°]
T_{EAS}	EAS duration on the detector's focal surface	[μs]
$\Delta\alpha$	Pixel granularity	[°]
B	Background radiance	[ph·m^{-2}·s^{-1}·sr^{-1}]
μ_{B}	Mean background rate in the detector	[ph·s^{-1}]
n_{B}	Mean number of background counts per time unit	[s^{-1}]

Bibliography

[1] J. Linsley. Evidence for a Primary Cosmic-Ray Particle with Energy 10^{20} eV. *Phys. Rev. Lett.*, 10:146–148, 1963.

[2] M. A. Lawrence, R. J. O. Reid, and A. A. Watson. The cosmic ray energy spectrum above 4x10**17-ev as measured by the haverah park array. *J. Phys.*, G17:733–757, 1991.

[3] N. N. Efimov, N. N. Efremov, A. V. Glushkov, I. T. Makarov, and M. I. Pravdin. Peculiarities of muon component in giant eas. Prepared for ICCR International Symposium on the Astrophysical Aspects of the Most Energetic Cosmic Rays, Kofu, Japan, Nov. 26-29, 1990.

[4] D. J. Bird et al. The cosmic ray energy spectrum observed by the fly's eye. *Astrophys. J.*, 424:491–502, 1994.

[5] D. J. Bird et al. Detection of a cosmic ray with measured energy well beyond the expected spectral cutoff due to cosmic microwave radiation. *Astrophys. J.*, 441:144–150, 1995.

[6] M. Takeda et al. Extension of the cosmic-ray energy spectrum beyond the predicted greisen-zatsepin-kuzmin cutoff. *Phys. Rev. Lett.*, 81:1163–1166, 1998.

[7] N. Hayashida et al. Observation of a very energetic cosmic ray well beyond the predicted 2.7-k cutoff in the primary energy spectrum. *Phys. Rev. Lett.*, 73:3491–3494, 1994.

[8] N. Hayashida et al. Updated agasa event list above 4*10**19-ev. *Astron. J.*, 120:2190, 2000.

[9] J. Linsley. Call for project and ideas in high energy astrophysics, 1979.

[10] J. Linsley. Neutrino Astronomy Using Socras - a Satellite Observatory for Cosmic-Ray Air Showers. In *SOUTHWEST REG. CONF. ASTRON.& ASTROPH., V.7, P.169, 1981*, pages 169–+, 1981.

[11] Orbiting Wide-angle Light-collectors. `http://owl.gsfc.nasa.gov/`.

[12] V. I. Abrashkin et al. Preparation of the TUS space experiment for UHECR study. *Int. J. Mod. Phys.*, A20:6865–6868, 2005.

[13] A. Petrolini. EUSO: A space-borne experiment for UHECR observations. 2004. Prepared for International Workshop on Frontier Science: Physics and Astrophysics in Space, Frascati and Rome, Italy, 14-19 Jun 2004.

[14] ESA. Cosmic Vision. Space Science for Europe 2015-2025, 2005.

[15] J. W. Cronin, S. P. Swordy, and T. K. Gaisser. Cosmic rays at the energy frontier. *Sci. Am.*, 276:32–37, 1997.

[16] Gerard Jungman, Marc Kamionkowski, and Kim Griest. Supersymmetric dark matter. *Phys. Rept.*, 267:195–373, 1996.

[17] L. Bergstrom. Particle dark matter and its indirect detection. *New Astron. Rev.*, 42:245–257, 1998.

[18] David Maurin et al. Galactic cosmic ray nuclei as a tool for astroparticle physics. 2002.

[19] D. R. Bergman. Fitting the hires spectra. 2005.

[20] The Auger Collaboration. The Pierre Auger Observatory Design Report, 1997. `http://www.auger.org`.

[21] Review of Particle Physics. *Physics Letters B*, 592:1+, 2004. `http://pdg.lbl.gov`.

[22] K. Greisen. Progress in cosmic-ray physics 3. 3, 1956.

[23] W. Heitler. *The Quantum Theory of Radiation*. Dover Publications, 1984.

[24] C. L. Pryke. A comparative study of the depth of maximum of simulated air shower longitudinal profiles. *Astropart. Phys.*, 14:319–328, 2001.

[25] M. et Al Ave. New constraints from haverah park data on photon and iron fluxes of uhe cosmic rays. *Phys. Rev. Lett.*, 85, 2000.

[26] Markus Risse. Upper limit on the primary photon fraction from the pierre auger observatory. 2005.

[27] Ralph Engel. Very high energy cosmic rays and their interactions. *Nucl. Phys. Proc. Suppl.*, 151:437–461, 2006.

[28] J. Linsley and A. A. Watson. Validity of scaling to 10**20-ev and high-energy cosmic ray composition. *Phys. Rev. Lett.*, 46:459–463, 1981.

[29] A. A. Watson. The mass composition of cosmic rays above 10**17-ev. *Nucl. Phys. Proc. Suppl.*, 136:290–300, 2004.

[30] Luis Anchordoqui et al. High energy physics in the atmosphere: Phenomenology of cosmic ray air showers. *Ann. Phys.*, 314:145–207, 2004.

[31] O. Adriani et al. Technical design report of the lhcf experiment: Measurement of photons and neutral pions in the very forward region of lhc. CERN-LHCC-2006-004.

[32] K. Eggert. The totem experiment. Prepared for LHC Days 2003, Les Diablerets, Switzerland, 2- 4 Jun 2003.

[33] J. Linsey. Fluctuation effects on directional data. *Phys. Rev. Lett.*, 34, 1975.

[34] Luis A. Anchordoqui et al. Full-sky search for ultrahigh-energy cosmic ray anisotropies. *Phys. Rev.*, D68:083004, 2003.

[35] R. Abbasi et al. Search for global dipole enhancements in the hires-i monocular data above 10**18.5-ev. *Astropart. Phys.*, 21:111, 2004.

[36] N. Hayashida et al. The anisotropy of cosmic ray arrival direction around 10**18-ev. 1999.

[37] N. Hayashida et al. Possible clustering of the most energetic cosmic rays within a limited space angle observed by the akeno giant air shower array. *Phys. Rev. Lett.*, 77:1000–1003, 1996.

[38] Y. Uchihori et al. Cluster analysis of extremely high energy cosmic rays in the northern sky. *Astropart. Phys.*, 13:151–160, 2000.

[39] P. G. Tinyakov and I. I. Tkachev. Correlation function of ultra-high energy cosmic rays favors point sources. *JETP Lett.*, 74:1–5, 2001.

[40] R. U. Abbasi et al. Study of small-scale anisotropy of ultrahigh energy cosmic rays observed in stereo by hires. *Astrophys. J.*, 610:L73, 2004.

[41] R. U. Abbasi et al. A search for arrival direction clustering in the hires-i monocular data above 10**19.5-ev. *Astropart. Phys.*, 22:139–149, 2004.

[42] Benoit Revenu. Search for localized excess fluxes in auger sky maps and prescription results. 2005.

[43] Chad B. Finley and Stefan Westerhoff. On the evidence for clustering in the arrival directions of agasa's ultrahigh energy cosmic rays. *Astropart. Phys.*, 21:359–367, 2004.

[44] A. M. Hillas. Proc. of 11th ICRC. volume 3, page 355, 1970.

[45] A. M. Hillas, D. J. Marsden, J. D. Hollows, and H.W. Hunter. Proc. of 12th ICRC. volume 3, page 1001, 1971.

[46] J. J. Beatty. The pierre auger project: An observatory for the highest energy cosmic rays. *Int. J. Mod. Phys.*, A16S1C:1022–1024, 2001.

[47] M. Teshima. Agasa results and telescope array project. *AIP Conf. Proc.*, 566:184–194, 2000.

[48] Arno A. Penzias and Robert Woodrow Wilson. A measurement of excess antenna temperature at 4080-mc/s. *Astrophys. J.*, 142:419–421, 1965.

[49] Kenneth Greisen. End to the cosmic ray spectrum? *Phys. Rev. Lett.*, 16:748–750, 1966.

[50] G. T. Zatsepin and V. A. Kuzmin. Upper limit of the spectrum of cosmic rays. *JETP Lett.*, 4:78–80, 1966.

[51] A. Mucke, Ralph Engel, J. P. Rachen, R. J. Protheroe, and Todor Stanev. Monte carlo simulations of photohadronic processes in astrophysics. *Comput. Phys. Commun.*, 124:290–314, 2000.

[52] J. L. Puget, F. W. Stecker, and J. H. Bredekamp. Photonuclear interactions of ultrahigh-energy cosmic rays and their astrophysical consequences. *Astrophys. J.*, 205:638–654, 1976.

[53] V. S. Berezinsky and A. Z. Gazizov. Production of high-energy cosmic neutrinos in p gamma and n gamma scattering: 1. neutrino yields for power law spectra of protons and neutrons. *Phys. Rev.*, D47:4206–4216, 1993.

[54] F. W. Stecker. Effect of photomeson production by the universal radiation field on high-energy cosmic rays. *Phys. Rev. Lett.*, 21:1016–1018, 1968.

[55] Michael Blanton, Pasquale Blasi, and Angela V. Olinto. The gzk feature in our neighborhood of the universe. *Astropart. Phys.*, 15:275–286, 2001.

[56] V. S. Berezinsky and S. I. Grigor'eva. A bump in the ultrahigh-energy cosmic ray spectrum. *Astron. Astrophys.*, 199:1–12, 1988.

[57] T. W. Jones. Cosmic particle acceleration: Basic issues. 2000.

[58] Enrico Fermi. On the origin of the cosmic radiation. *Phys. Rev.*, 75:1169–1174, 1949.

[59] Luke O'C. Drury. Acceleration of cosmic rays. *Contemp. Phys.*, 35:231–242, 1994.

[60] Angela V. Olinto. From the galaxy to the edge of the universe: Plausible sources of uhecrs. *AIP Conf. Proc.*, 566:99–112, 2000.

[61] Pasquale Blasi, Richard I. Epstein, and Angela V. Olinto. Ultra-high energy cosmic rays from young neutron star winds. *Astrophys. J.*, 533:L123, 2000.

[62] Elisabete de Gouveia Dal Pino and Alex Lazarian. Ultra-high-energy cosmic ray acceleration by magnetic reconnection in newborn accretion induced collapse pulsars. *Astrophys. J.*, 536:L31–L34, 2000.

[63] K.S. Thorne, R.H. Price, and D.A. Macdonald. *Black Holes: The Membrane Paradigm*. Yale University Press, New Haven and London, 1986.

[64] (ed.) Ginzburg, V. L., V. A. Dogiel, V. S. Berezinsky, S. V. Bulanov, and V. S. Ptuskin. Astrophysics of cosmic rays. Amsterdam, Netherlands: North-Holland (1990) 534 p.

[65] Jorg P. Rachen, Todor Stanev, and Peter L. Biermann. Extragalactic ultrahigh-energy cosmic rays. 2. comparison with experimental data. *Astron. Astrophys.*, 273:377, 1993.

[66] Martin Lemoine, Guenter Sigl, and Peter Biermann. Supercluster magnetic fields and anisotropy of cosmic rays above 10**(19) ev. 1999.

[67] Eun-Joo Ahn, Gustavo A. Medina-Tanco, Peter L. Biermann, and Todor Stanev. "The origin of the highest energy cosmic rays: Do all roads lead back to Virgo?". 1999.

[68] Mario Vietri. On the acceleration of ultrahigh-energy cosmic rays in gamma-ray bursts. *Astrophys. J.*, 453:883–889, 1995.

[69] Eli Waxman. Cosmological gamma-ray bursts and the highest energy cosmic rays. *Phys. Rev. Lett.*, 75:386–389, 1995.

[70] D. A. Frail, S. R. Kulkarni, S. R. Nicastro, M. Feroci, and G. B. Taylor. The radio afterglow from the gamma-ray burst of 8 may 1997. *Nature*, 389:261, 1997.

[71] E. et al. Costa. Discovery of an x-ray afterglow associated with the big gamma-ray burst of 28 february 1997. *Nature*, 387:783–785, 1997.

[72] T. J. Galama et al. Discovery of the peculiar supernova 1998bw in the error box of grb980425. *Nature*, 395:670, 1998.

[73] Mario Vietri, Daniel De Marco, and Dafne Guetta. On the generation of uhecrs in grbs: A reappraisal. *Astrophys. J.*, 592:378–389, 2003.

[74] Pijushpani Bhattacharjee and Gunter Sigl. Origin and propagation of extremely high energy cosmic rays. *Phys. Rept.*, 327:109–247, 2000.

[75] Christopher T. Hill, David N. Schramm, and Terry P. Walker. Ultrahigh-energy cosmic rays from superconducting cosmic strings. *Phys. Rev.*, D36:1007, 1987.

[76] Ya. B. Zeldovich and Alexei A. Starobinsky. Particle production and vacuum polarization in an anisotropic gravitational field. *Sov. Phys. JETP*, 34:1159–1166, 1972.

[77] Daniel J. H. Chung, Edward W. Kolb, Antonio Riotto, and Igor I. Tkachev. Probing planckian physics: Resonant production of particles during inflation and features in the primordial power spectrum. *Phys. Rev.*, D62:043508, 2000.

[78] Vadim Kuzmin and Igor Tkachev. Ultra-high energy cosmic rays, superheavy long-living particles, and matter creation after inflation. *JETP Lett.*, 68:271–275, 1998.

[79] V. Berezinsky, M. Kachelriess, and A. Vilenkin. Ultra-high energy cosmic rays without gzk cutoff. *Phys. Rev. Lett.*, 79:4302–4305, 1997.

[80] James W. Cronin. The highest-energy cosmic rays. *Nucl. Phys. Proc. Suppl.*, 138:465–491, 2005.

[81] US Standard Atmosphere. `http://modelweb.gsfc.nasa.gov/atmos/us_standard.html`.

[82] T. K. Gaisser and A. M. Hillas. Proc. 15th ICRC. volume 8, page 353, 1977.

[83] C. Pryke. *Astropart. Phys.*, 14:319–328, 2001. astro-ph/0003442.

[84] T. Stanev. *High Energy Cosmic Rays*. Springer, 2004.

[85] F. Kakimoto et al. *Nucl. Instrum. Meth.*, A372:527–533, 1996.

[86] P. Mazzinghi et al. Physics and Astrophysics in Space, Frascati Physics Series vol. xxxvii, 437-444. 2004.

[87] L. M. Barbier et al. *Astropart. Phys.*, 22:439–449, 2005.

[88] O. Catalano et al. *NIM "A"*, 480(2-3):547–554, 2002.

[89] D. J. Knecht et al. *Advances in Space Research*, 19(4):627–630, 1997.

[90] G. K. Garipov et al. *JEPT Letters*, 82(4):185–187, 2005.

[91] Heck D. and Pierog T. *Extensive Air Shower Simulations with CORSIKA: A User's Guide*. CORSIKA an Air Shower Simulation Program `http://www-ik.fzk.de/corsika/`.

[92] S. J. Sciutto. Aires: A system for air shower simulations (version 2.2.0). 1999.

[93] S. Bottai. 27th International Cosmic Ray Conferences (ICRC 2001), Hamburg, Germany, 7 - 15 Aug 2001.

[94] D. Naumov. Slast: Shower initiated light attenuated to the space telescope. EUSO Report SDA-REP-015, 2003.

[95] J. Engel, T. K. Gaisser, T. Stanev, and Paolo Lipari. Nucleus-nucleus collisions and interpretation of cosmic ray cascades. *Phys. Rev.*, D46:5013–5025, 1992.

[96] R. S. Fletcher, T. K. Gaisser, Paolo Lipari, and Todor Stanev. Sibyll: An event generator for simulation of high-energy cosmic ray cascades. *Phys. Rev.*, D50:5710–5731, 1994.

[97] J. et al. Engel. Proc. of 26th ICRC, Salt Lake city, (USA).

[98] A.M. Hillas. *J. Phys. G Nucl. Phys. 8*, 1982.

[99] Baltrusaitis et al. *J. Phys. G Nucl. Phys. 13*, 1987.

[100] M. Nagano, K. Kobayakawa, Naoto Sakaki, and K. Ando. New measurement on photon yields from air and the application to the energy estimation of primary cosmic rays. *Astropart. Phys.*, 22:235–248, 2004.

[101] Bunner A.N. PhD thesis, 1964. Ph.D Thesis.

[102] Lebrun D. ISN-Grenoble Report 02-37, 2002.

[103] Kneizys F.X. et al. The modtran 2/3 report and lowtran 7 model. 1996.

[104] A.E. Hedin. A Revised Thermospheric Model Based on Mass Spectrometer and Incoherent Scatter Data: MSIS-83. *J. Geophys. Res.*, 88:10170, 1983.

[105] A.E. Hedin. MSIS-86 Thermospheric Model. *J. Geophys. Res.*, 92:4649, 1987.

[106] A.E. Hedin. Extension of the MSIS Thermosphere Model into the Middle and Lower Atmosphere. *J. Geophys. Res.*, 96:1159, 1991.

[107] International satellite cloud climatology project. `http://isccp.giss.nasa.gov/`.

[108] S. Giarrusso et al. Measurements of the uv nocturnal atmospheric background in the 300-nm to 400-nm wavelength band with the experiment baby during a transmediterranean balloon flight. Prepared for 28th International Cosmic Ray Conferences (ICRC 2003), Tsukuba, Japan, 31 Jul - 7 Aug 2003.

[109] Leinert et al. The 1997 reference of diffuse night sky brightness. *Astron. Astrophys. Suppl. Ser.*, 127:1–99, 1998.

[110] P. Cinzano, F. Falchi, and C. D. Elvidge. The first world atlas of the artificial night sky brightness. *Mon. Not. Roy. Astron. Soc.*, 328:689, 2001.

[111] C. P. Barrington-Leigh. PhD thesis, 2000. Ph.D Thesis.

[112] P. Colin, D.V. Naumov, and P. Nedelec. EUSO Reconstruction Algorithms, 2003. EUSO-SDA-REP-016-1.

[113] The EUSO Collaboration. EUSO: Report on the Phase A Study, 2003. preprint EUSO-PI-REP-002.

[114] P. Buzhan et al. Silicon photomultiplier and its possible applications. *Nucl. Instrum. Meth.*, A504:48–52, 2003.

[115] V. Golovin and V. Savelev. Novel type of avalanche photodetector with geiger mode operation. *Nucl. Instrum. Meth.*, A518:560–564, 2004.

[116] D. Bisello et al. Silicon avalanche detectors with negative feedback as detectors for high-energy physics. *Nucl. Instrum. Meth.*, A367:212–214, 1995.

[117] K. Arisaka. Conference summary and reference therein. 4th International Conference on New Developments in Photodetection (BEAUNE 2005): From Infra Red to Gamma Rays, Beaune, France, 19-24 Jun 2005.

[118] P. Buzhan et al. An advanced study of silicon photomultiplier. *ICFA Instrum. Bull.*, 23:28–41, 2001.

[119] J. Barral. Study of silicon photomultipliers.

[120] R. Newman. Visible light from a Si p-n junction. *Phys. Rev. Lett.*, 100:100–103, 1955.

[121] S. Cova, M. Ghigni, A. Lotto, and F. Zappa. Evolution and Prospect of Single Photon Avalanche Diodes and Quenching Circuits. 2003. Workshop on Single Photon Detectors Gathesburg.

[122] B. J. Pichler, S. I. Ziegler, E. Lorenz, R. Mirzoian, and L. Weiss. Production of a diffuse very high reflectivity material for light collection in nuclear detectors. *Nucl. Instrum. Meth.*, A442:333–336, 2000.

[123] C. Joram. Hpd and mapmt: Segmented photon detectors for hep and beyond. Prepared for INFN Eloisatron Project: 42nd Workshop on Innovative Detectors for Supercolliders, Erice, Sicily, Italy, 28 Sep - 4 Oct 2003.

[124] Y. Musienko. The gain, photon detection efficiency and excess noise factor of multipixel geiger-mode avalanche photodiodes. Prepared for 4th International Conference on New Developments in Photodetection (BEAUNE 2005): From Infra Red to Gamma Rays, Beaune, France, 19-24 Jun 2005.

[125] B. et al. Dolgoshein. Large area silicon photomultipliers: performance and applications. Prepared for 4th International Conference on New Developments in Photodetection (BEAUNE 2005): From Infra Red to Gamma Rays, Beaune, France, 19-24 Jun 2005.